INFRARED OPTICAL IMAGING TECHNIQUES FOR GAS VISUALIZATION AND MEASUREMENT

A Dissertation

by

ANISA SAFITRI

Submitted to the Office of Graduate Studies of
Texas A&M University
in partial fulfillment of requirements for the degree of

DOCTOR OF PHILOSOPHY

May 2011

Major Subject: Chemical Engineering

INFRARED OPTICAL IMAGING TECHNIQUES FOR GAS VISUALIZATION AND MEASUREMENT

A Dissertation

by

ANISA SAFITRI

Submitted to the Office of Graduate Studies of
Texas A&M University
in partial fulfillment of requirements for the degree of

DOCTOR OF PHILOSOPHY

Approved by:

Chair of Committee,	M. Sam Mannan
Committee Members,	Mahmoud M. El-Halwagi
	Charles J. Glover
	William H. Marlow
Head of Department,	Michael Pishko

May 2011

Major Subject: Chemical Engineering

ABSTRACT

Infrared Optical Imaging Techniques for Gas Visualization and Measurement.

(May 2011)

Anisa Safitri, B.S., Institut Telnologi Bandung, Indonesia; M.S., Tecnische Universiteit Eindhoven, the Netherlands

Chair of Advisory Committee: Dr. M. Sam Mannan

Advancement in infrared imaging technology has allowed the thermal imaging to detect and visualize several gases, mostly hydrocarbon gases. In addition, infrared cameras could potentially be used as a non-contact temperature measurement for gas and vapor. However, current application of infrared imaging techniques for gas measurements are still limited due to several uncertainties in their performance parameters. The aim of this research work was to determine the key factors in the application of infrared imaging technology for gas visualization and a non-contact temperature measurement. Furthermore, the concentration profile and emission rate of the gas are predicted by combining the application of the infrared imaging method with gas dispersion modeling.

In this research, infrared cameras have been used to visualize liquefied natural gas (LNG) plumes from LNG spills on water. The analyses of the thermograms showed that the apparent temperatures were different from the thermocouple measurement which occurred due to the assumption of that the object emissivity was always equal to unity.

The emissivity for pure methane gas and a mixture of methane and atmospheric gases were then evaluated in order to obtain the actual temperature distribution of the gas cloud. The results showed that by including the emissivity value of the gas, the temperature profile of the dispersed gas obtained from a thermal imaging measurement was in good agreement with the measurement using the thermocouples. Furthermore, the temperature distribution of the gas was compared to the concentration of a dispersed LNG vapor cloud to obtain a correlation between the temperature and the concentration of the cloud.

Other application of infrared imaging technique was also conducted for leak detection of natural gas from a pipeline. The capability of an infrared camera to detect a fugitive gas leak was combined with the simulation of vapor discharge and dispersion in order to obtain a correlation between the emission rates and the sizes of the gas plume to the minimum detectable concentration. The relationship of the methane gas cloud size to the gas emission rate was highly dependent to the prevailing atmospheric condition. The results showed that the correlation were best to predict the emission rate less than 0.2 kg/s. At higher emission rate, the increase in gas release rate did not change the size of the cloud significantly.

DEDICATION

To

My husband

Jaffee Arizon Suardin

and my son

Mika Aidan Suardin

ACKNOWLEDGEMENTS

There are many people who have been involved in making this dissertation happen. For that, I would like to offer my heartfelt thanks to my advisor, Dr. M.S. Mannan, who has giving me encouragement, support and supervision since the very first day I joined the Chemical Engineering Department as a Graduate Assistant until this concluding level. As my advisor, Dr. Mannan has not only given me an understanding of the research subject but more than that, he has inspired me through his mission, rich experience and knowledge to become a person with integrity, ethics, knowledge and character. He has given me a lot of opportunities to develop myself both personally and professionally.

I would like to recognize the Mary Kay O'Connor Process Safety Center for funding support of my research. It is also my pleasures to thank all of my committee members, Dr. Mahmoud El-Halwagi, Dr. Charles J. Glover and Dr. William H. Marlow, for the ideas and materials which are very beneficial for my research.

I am also thankful for all the members of Mary Kay O'Connor Process Safety Center. I would like to give my appreciation to the staff: Valerie Green, Donna Startz, Mary Cass and Danielle Burns. Without their cooperation and help I would not have achieved this level of success. Also, I'd like give my regards to the post-docs at the MKOPSC for constantly giving me direction, guidance and assistance especially to Dr. Yanjun Wang, Dr. Yuyan Guo and Dr. Xioadan Gao. I'm offering blessings also to all of

those who supported me in any respect and contributed in any forms towards the successful completion of my dissertation.

I would like to thank all the special people who have been tirelessly giving me love and moral support, especially my husband. It would have been impossible for me to accomplish this project without his encouragement and guidance. I also would like to thank my parents, Soetrisno Soetojo and Ela Turmala Tarmidi, and parents-in-law, Ir. Suardin and Linggardjati Suardin, for being very supportive and always keeping me in their prayers. I'd also like to give my appreciation to my brother, Aditya Prabowo, and my sisters and brothers in law for their love and support. I'd like to send my blessings to my aunt, Nunung Tardine, for spending her time and energy to support me and for lovingly and patiently taking care of my son during the completion of my research work.

Lastly, I am very grateful to my son, Mika Aidan Suardin, who has been very patient, brave, and understanding throughout this whole period. I thank him for always giving me the most wonderful smiles, even when I had to come home late and wake him up from his sleep. And for that, I am dedicating this dissertation to him.

TABLE OF CONTENTS

Page

Page

Page

LIST OF FIGURES

Page

Page

Page

Page

Page

LIST OF TABLES

Page

1. INTRODUCTION

1.1 Overview of Natural Gas System

Natural gas is a mixture containing combustible hydrocarbon gases with methane as the primary component. Natural gas is a major component in the world's energy supply and is constantly used for generating electricity, heating and cooking. Therefore, the availability of this energy resource is vital to human life. Natural gas in the Unites States is abundant; however, since natural gas is one form of a non-renewable energy resource, the availability of the natural gas supply depends on the demand of the use of this fossil fuel.

Natural gas is the second largest energy consumed in the United States. High amount of energy can be obtained by burning natural gas. Another advantage of the use of natural gas is that it gives less emission and less harmful byproducts compared the burning of other fossil fuels. For that reason, natural gas is considered as one of the cleanest and safest energy resources.

This dissertation follows the style and format of the *Journal of Loss Prevention in the Process Industries.*

1.1.1 Natural Gas Consumption in the United States

Natural gas is one of the major energy resources in the Unites States. The use of natural gas as a source of energy is very crucial for all sectors of the US economy, including residential, commercial, industrial, utility and transportation. According to the Annual Energy Report 2008 by Energy Information Administration, natural gas accounts for 25% of primary energy consumption in the US by source, of the total of 98 Quadrillion Btu as shown in Figure 1 (EIA, 2009a).

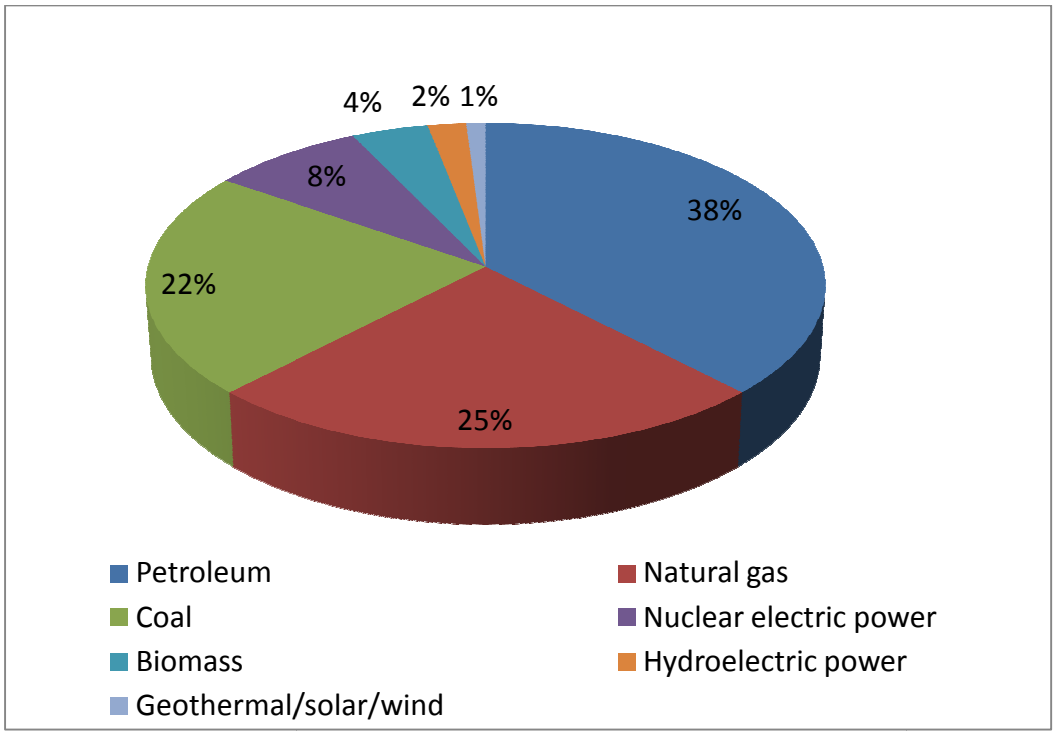

Figure 1. U.S. Energy Consumption by Source in 2008 (Data source: EIA, 2009a)

Residential end-users accounted for 21 % of total natural gas consumption in the U.S.; however, due to the increase in equipment efficiency, improved housing construction and warmer-than-normal winter weather have contributed to the reduction in residential natural gas consumption. EIA reported that the U.S. residential natural gas consumption showed decreasing trends from 1998 to 2009. In 2008, the total U.S. consumption of natural gas accounted for 23.2 Trillion cubic feet (Tcf) from all sectors including residential, commercial, industrial and power generation (EIA, 2009a).

1.1.2 Natural Gas Production, Transportation, Distribution and Storage System

Based on EIA data, there are more than 450,000 natural gas producing wells in the U.S., operated by more than 6300 producers (EIA, 2009b). The natural gas distribution system consists of approximately 305,000 miles of interstate and intrastate transmission pipelines, more than 1,400 compressor stations, 11,000 delivery points, 5,000 receipt points and 1,400 interconnection points throughout the United States. This distribution network is capable of transferring over 148 Billion cubic feet (Bcf) of gas per day. There are 400 underground natural gas storage facilities in the US, with a storage capacity of 4,059 Bcf and the capability to deliver 85 Bcf of gas per day, in addition to 8 LNG (Liquefied Natural Gas) import facilities and 100 LNG peaking facilities (EIA, 2009b).

In 2009, the average marketed production of natural gas was about 60 Bcf per day and the total production in a year was 21.9 Tcf. According to the study conducted by

Colorado School of Mines Potential Gas Committee, there are approximately 2,074 technically recoverable natural gas resources in the U.S.

Also in 2009, there were several additions to the national pipeline grid close to 3,000 miles of pipe and about 43 natural gas pipeline projects. Rockies Express East (REX-East) project was the largest natural gas pipeline project completed in 2009. In addition, LNG imports increased from 352 Bcf in 2008 to 452 Bcf in 2009 (EIA, 2009b).

1.1.3 Emissions from Natural Gas Systems

Natural gas is considered one of the cleanest energy sources because the combustion of natural gas results in low SO_2 and NO_x emissions and almost no particulate or ash. However, methane, which is the main constituent of natural gas, is one of the most potent greenhouse gases. The energy sectors, including coal mining, natural gas systems, petroleum systems and stationary and mobile combustion, contributed to the largest U.S. methane emission. In 2008, the methane emissions from these energy sectors accounted for 295.7 $MMCO_2$ equivalents (EPA, 2008a).

In the natural gas systems, methane is constantly released during production, processing, and transmission, as well as distribution. EPA reported the emission from natural gas system accounts for 104.7 Tg CO_2 Eq. (4,985 Gg) of CH_4 in U.S. Inventory of Greenhouse Gas Emissions and Sinks 1990 – 2007 (EPA, 2008a). More than half of the methane emissions come from fugitive leaks, which occur during normal operation, routine maintenance or system upsets. Methane emissions from natural gas systems are

estimated using a methodology developed by The Gas Research Institute (GRI) and EPA as described in Figure 2. In source categorization emissions from natural gas systems are categorized by the industry segments, operating modes, and emission types (Kirchgessner, 1997).

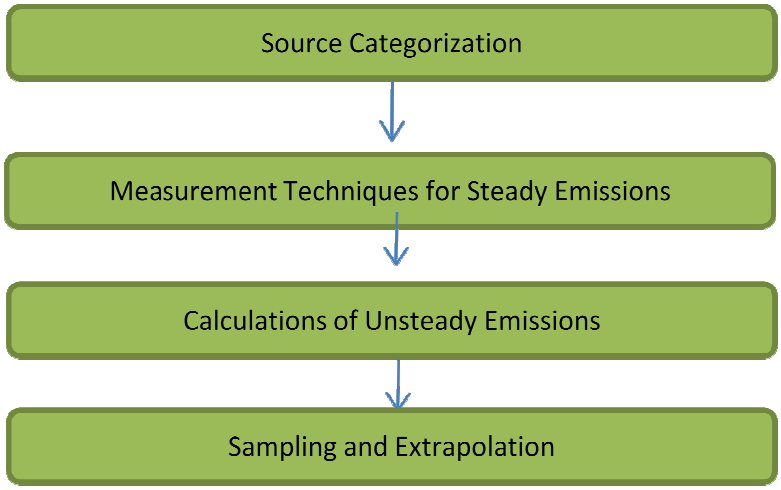

Figure 2. EPA/GRI 1996 Method to Estimate Methane Emission

There are three steps in estimating the steady emissions of natural gas, namely the component measurement method, the tracer gas method and the leak statistic method. The leak statistic method is used to quantify methane emissions by analyzing the historical leak records to determine the number of leaks and the average leak rate to calculate the total emissions. The leak measurement was performed using a handheld device which detects methane gas point by point and measures the gas concentration (Kirchgessner, 1997).

Unsteady methane emissions are estimated from detailed company records of unsteady methane releases, detailed characterizations of the source, and identification of the important parameter affecting emissions. Finally, sampling and extrapolation were performed to minimize bias in the data as well as to evaluating the relationship between the emission rate and parameter that may affect the emissions (Kirchgessner, 1997).

The release of hydrocarbon gases into the atmosphere also creates excessive problems, such as risk of explosions and fires, energy loss, and environmental hazards through its contribution to the greenhouse effect. A leak in the natural gas pipeline has the potential for releasing gas consisting up to 80% methane into the atmosphere. Therefore, rapid detection and localization of the methane leak are in a great demand. In addition, the selective sensitivity of natural gas, i.e. methane, is also required, as well as the detection of the methane concentration, to maintain the gases below the threshold of the risk of an explosion (Sandberg, *et al.*, 1989).

1.2 EPA Leak Detection and Repair (LDAR)

EPA has determined that the largest source of emissions of a volatile organic compound (VOC) from petroleum refineries and chemical manufacturing facilities resulted from leaking equipment, such as valves, pumps, compressors, flanges and connectors. According to the agency report, approximately 70,367 tons of VOCs per year leak from the equipment into the atmosphere (EPA, 1995b).

Therefore, EPA developed a work practice, namely the leak detection and repair (LDAR) program, which was designed for facilities to identify leaking equipment so that the emissions can be controlled and reduced through repairs. The implementation of LDAR practice has been required by 25 federal standards (EPA, 1995b).

LDAR program requires monitoring of the equipment at regular intervals in order to specify whether or not the component is leaking. EPA predicted that emissions of VOCs can be reduced by 63% for petroleum refineries and 56% for chemical industries when the LDAR program is implemented. In addition, there are several other advantages that resulted from the implementation of this program, including reducing production loss, increasing the facility workers and operators' safety, decreasing the exposure of hazardous material to the surrounding community, and avoiding enforcement action (EPA, 1995b).

1.2.1 EPA Method 21

25 federal standards required the implementation of a formal LDAR program using Method 21 and the hand held total vapor analyzers (TVA), also called "sniffers." EPA method 21 is applied to determine VOC leaks from process equipment. The sources include valves, flanges, pumps and compressors, pressure relief devices, process drains, open ended valves, pump and compressor seal system degassing vents, accumulator vessel vents, agitation seals and access door seals. The objective of this method is to enhance the quality of the air pollutant from the sampling methods (EPA, 1995a).

A portable instrument is used to detect VOC leaks from individual sources. This method is intended to locate and classify leaks only and not used as a tool for the direct measurement of mass emission rates from individual sources.

Several volatile organic compounds which may be determined by this method might be irritating or corrosive (e.g. heptane), toxic (e.g. benzene, methyl alcohol), and nearly all are fire hazards. The VOC monitoring instrument should meet several specifications required (EPA, 1995a):

1. The instrument is responsive to the compounds which are being processed. Included in this criterion are catalytic oxidation, flame-ionization, infrared absorption and photo-ionization.
2. The instrument is capable of measuring the leak definition concentration specified in the regulation. The leak definition concentration is the local VOC concentration at the surface of a leak source that indicates the presence of VOC emission.
3. The scale of the instrument meter shall be readable to approximately 2.5% of the specified leak definition concentration.
4. The instrument should be equipped with an electric pump to ensure that the sample is provided to the detector at a constant flow rate.
5. Probes and probe extensions, not exceeding 6.4 mm in outside diameter and with a single admission opening for the sample, have to be provided for sampling.
6. The instrument must be intrinsically safe for operation in explosive atmospheres as defined by the National Electrical Code by NFPA.

1.2.2 Smart LDAR Using Infrared Imaging Techniques

Finding leaks using method 21 is labor intensive, time consuming and surveys must be conducted point by point in close proximity with pipes, valves and other volatile organic compounds (VOC) carrying components. In addition, vapor analyzers do not actually measure the emissions rate of the leak, rather they use an empirical equation to convert the concentration (parts per million by volume) into mass flow rate (Robinson *et al.*, 2007).

Recently, a new gas detection method using infrared optical imaging techniques became popular in the oil and gas industry. This technique allows for the visualization of several hydrocarbon gases. This method is much more effective compared to the conventional method for its ability to (EPA, 2008b), (Benson *et al.*, 2006a; Madding, 2006):

- Visualize leaks in real time,
- Pinpoint leak locations,
- Scan large areas rapidly,
- Scan components that are hard to reach by contact measurement tools,
- Detect leaks without interrupting processes,
- Monitor potentially dangerous leaks from a distance,
- Record and documents leaks, and
- Detect the gas remotely.

The utilization of infrared imaging systems potentially simplifies the EPA LDAR program and therefore it is currently recognized in industry as a Smart-LDAR approach. Optical imaging techniques must meet several requirements to qualify as a smart approach equivalent to the traditional LDAR approach including (Epperson *et al.*, 2007):

- It should be able to significantly reduce monitoring cost.
- It performs more frequent monitoring of process equipment.
- It should be able to locate leaks from high leaking components without having to monitor every individual piping component.
- It provides more effective control.
- It results in better emission reduction.
- It gives better environmental protection.
- Based on API report, 90% of all emission comes from 1% of leaks. Smart LDAR is able to detect and locate the high leakers and therefore it is more cost-effective.

Table 1 provides the comparison between smart LDAR using optical imaging instruments compared to traditional LDAR using single point measurement.

Table 1. Comparison of Traditional and Smart LDAR

Measurement characteristics	Traditional LDAR	Smart LDAR
Sampling capability	Single point measurement	Area scanning of a facility
Sampling of components	Only small number of components in 1-hr duration of sampling.	Able to scan up to 3000 components per hour, 20 times faster than traditional method.
Mass emission rate measurement	Inaccurate because it measures the ambient concentration adjacent to the leaking components. Poor correlation of the actual emission rate.	Leak detection threshold is identified from several laboratory and field tests which was measured in g/hr.
Location of instrument during measurement	Must be in the vicinity of the leaking components	Capable to monitor the leaks remotely.
Ability to pinpoint leaks	No	Yes. It can visualize gas leaks thus able to exactly locate the location of the leak.
Multiple components monitoring	No	Yes. Able to simultaneously identify and control multiple components.
Monitoring frequency	90 days for every piping components	60 days for valve, 45 days for pumps and 30 days for flanges.

1.3 Problem Statement

Infrared imaging techniques are currently considered the state-of-the art gas detection method because of their qualifications shown in Table 1. Unfortunately, infrared cameras can only provide qualitative measurements of the gas; the thermograms demonstrate the presence of the gas but do not provide quantitative measurement of the gas concentration or gas emission rates. In fact, this information is crucial in order to gain information on leak frequency and emission estimation to ensure the success of the LDAR program for gas emission control and reduction.

One of the gaps in the application of infrared cameras for gas visualization and measurement is the lack of knowledge of physics and fundamentals on how the infrared cameras measures the radiation emitted by the target gas. Infrared cameras are also known as thermal cameras because they measure the thermal heat radiation that transfers from the environment to an object. However, there are no published works which explored this capability during the application of infrared cameras for gas detection. One major barrier is that the performance parameters of the infrared imaging for gas detection and visualization have not been identified.

Some previous works have identified the sensitivity of the infrared camera to detect gas, i.e. the minimum detectable concentrations under different environments have been specified. However, the application of this method has not been extended to estimating the gas emission rates based on the size of the gas plume at the minimum detectable concentrations. A semi-quantitative approach to determine the mass emissions

rate of a hydrocarbon gas release has been done previously. Field data and Monte Carlo statistical simulation techniques were applied to obtain the emission factor for valve, pump, connector, flange and instrument leaks. However, this method evaluated the emission factor of a component by comparing the leak rate to the lowest threshold, or sensitivity level, to which the camera detector would respond. The emission factor was calculated by summing the total emissions divided by the total count of the components. Furthermore, this semi-quantitative measure was general for all hydrocarbons which an infrared camera could detect. This method was not able to identify the correlation between the sizes of detected gas plumes and the emissions rate for a specific gas. Different gases have different characteristic when released to the atmosphere. Some gases are denser than air and have a tendency to stay on the ground before eventually warming and lifting up, whereas, some gases are lighter than air and rise when released into the atmosphere. Accurate quantitative measures for specific gases are important, and this paper proposes a solution for estimating the gas mass flow rate of methane emissions based on a dispersion modeling approach.

1.4 Objectives

Based on the concepts and research gaps described in the first section, the objectives of this research are:

- To assess the utilization of infrared imaging for LNG vapor cloud detection and visualization by:

- Obtaining and analyzing the thermograms of LNG vapor cloud from the LNG spill tests.
- Determining factors affecting the LNG cloud visualization and measurement.
- Specifying the discrepancy in thermal distribution of the LNG plume from the infrared camera and the direct contact temperature measurement device (thermocouple).
- Determining the most significant uncertainties in gas temperature measurement.
- Utilizing the correction factors in order to obtain accurate temperature profiles of the gas clouds.
- Developing a correlation between temperature and concentration of dispersed LNG vapor.

and

❖ To develop a methodology for estimating the methane gas emission rate from natural gas systems, specifically by:

- Conducting vapor dispersion modeling to simulate the dispersion of methane gas from leaks in natural gas systems.
- Establishing the correlation of the size of the plume to the minimum detectable gas concentration and the amount of gas emitted to the atmosphere.
- Identifying the uncertainty of the methodology.

1.5 Organization of Dissertation

This dissertation presents a study on the application of infrared imaging techniques for gas detection, visualization and measurement. The overall research works are mainly divided into two parts: (i) potential application of infrared cameras as a non-contact temperature measurement of LNG vapor clouds and (ii) development of a novel approach using gas dispersion modeling to quantify methane emission rates from rather qualitative measurements of methane leaks using an infrared imaging method.

Section 1 introduces the background on what motivates this research work. The motivation to conduct the study on the natural gas systems is discussed in this section. The second part of this section describes the EPA LDAR program and its current implementation following the gap analysis on the current application of infrared imaging methods.

Section 2 provides a comprehensive literature review on the current research status of the application of infrared imaging techniques for gas detection and visualization. The infrared camera fundamentals and the camera detectors' algorithm to measure the thermal radiation emitted by a target object is described in Section 2. A semi-quantification approach to estimate methane emission rates using infrared imaging is also explained in this section. The last part of this section provides an overview of vapor dispersion modeling, which is important in developing a methodology to quantify methane emission rates from the thermograms of a methane vapor cloud.

The research methodology and the overall framework are presented in Section 3. The approach is divided into two parts: (i) LNG systems and (ii) natural gas pipeline systems. For the LNG systems, the approach to obtain accurate temperature profiles of the LNG vapor is described. For the natural gas pipeline systems, the methodology to achieve the correlation between gas plume sizes detected in the thermogram to the emission rates is developed.

Section 4 contains the detailed results of the study on the LNG system. Analysis of the thermograms of LNG vapor clouds is provided in this section. The evaluation of the parameters affecting the camera performance for gas temperature measurements is presented in Section IV. The calculations of the gas emissivity of pure methane gas and a mixture of methane and atmospheric gases are described in this section as well. The last part of this section describes the development of temperature and concentration correlations for LNG vapor clouds.

Section 5 presents the developed methodology which can be used to predict the emission rates of methane from the leaks in natural gas pipeline systems. The application of infrared imaging techniques combined with gas dispersion modeling is used to correlate emission rates to plume size up to the minimum detectable concentration. Uncertainty analysis is carried out and presented in the last part of this section. Finally, Section 6, the last part of this dissertation, presents the overall conclusions of the research work and the recommendations for potential future research works.

2. BACKGROUND

2.1 Overview

Infrared optical imaging has been tested in the oil and gas industries, including refineries, and has demonstrated promising results for fugitive emissions detection and survey. This technology allows the user to see leaking gas from equipment as a real-time video image.

Infrared cameras detect the absorptive and emissive characteristics of several gases. Gas molecules absorb a photon and transitions from one state to another due to the dipole moment, which enables the molecule to oscillate in the same frequency as the incident photon, and transfer electromagnetic energy. Each molecule has a specific absorption range within the infrared spectrum. In a particular type of infrared camera, the focal plane arrays of the camera detector can be tuned to a very narrow spectral region where the gas has a strong absorption rate, and therefore, the gas can be visualized (Smith, 1999).

Infrared imaging systems detect the radiation emitted by the target and background. Detection can occur only if the target signature can be distinguished from the background. The basic input parameter for detection is the contrast in transmitted radiation between the target and background, which generates a detector output voltage. The infrared camera can see certain gases, mostly hydrocarbons, because the camera's detector is equipped with a filter which is sensitive to only a certain wavelength. The C-

H bond has an absorption characteristic at 3.46 μm; therefore, the infrared camera for hydrocarbon gas visualization generally has an absorption window within this range i.e. a mid-wave IR range. Since the camera detectors are sensitive to only certain wavelengths, detectors which are active at different wavelengths will have different spectral responses. The radiation intensity of the target object and background depends on their temperatures. It is possible to visualize the gas against the background only if the background and the target gas cloud are not in thermal equilibrium. If the gas temperature is uniform with the background temperature, the gas cannot be discriminated against the background. In this application, the infrared camera can visualize gas, which has lower temperature than the surrounding due to the expansion process when the gas is released. Different camera systems generally have different amplifiers. The combination between the detector and amplifier will result in different gains and levels, and thus different noise patterns (Holst, 2000).

2.2 Preliminary Research

2.2.1 Infrared Camera Fundamentals and Application

The principle of the thermal IR imaging camera is based on the fact that objects above absolute zero emit infrared thermal radiation due the temperature difference. Hence the aim in using infrared camera technique is to calculate the noise equivalent temperature difference (NETD), defined as the temperature change for any incident radiation that gives an output signal equal to the root mean square (rms) noise level

(Holst, 1998). This requires one to relate the temperature difference and the emissivity of the background gas to the measured gas. A test under real conditions could prospectively resolve some difficulties associated with obtaining a significant difference between the plume temperature and radiometric temperature of the background, as well as removal of the spectral feature of the background, and correctly account for internal emissions of the spectrometer elements when viewing cold backgrounds to acquire quantitative information about the plume. Typically, the background temperature is lower than or almost similar to the plume temperature and thus the self radiance of the plume has to be taken into account while doing the measurement (Holst, 1998).

Thermal imaging systems sense the radiation emanating from a surface and the camera detectors measure the radiation flux impinging upon them. The amount of energy emitted by the surface depends on the surface characteristics and temperature. The total amount of radiation released from a surface is described by the Stefan-Boltzmann law. In the Stefan-Boltzmann law, it is assumed that the target and its background are ideal blackbodies. However, real materials, especially gases, are not ideal blackbodies. The amount of radiation that appears to emanate from a surface is characterized by their emissivities (Holst, 1998).

Infrared cameras measured the radiation that appeared to emanate from an object. The system calibration converted the output voltage to temperature. The calibration provided a two-dimensional representation of the surface temperature. An object emitted energy from its internal molecular vibration. The energy emitted from an object depends on its surface temperature and surface characteristics. The camera detected the amount

of flux impinging upon a detector. By knowing the detector's spectral responsivity, the electrical signal could be determined and amplified to create a visible image. The temperature of an object depends on its physical properties, such as heat capacity and specific heat, in which the quantity varies with the material phase (Caniou, 1999; Jacob, 2006).

Heat measurement using the thermal imaging system was conducted either qualitatively or quantitatively. Qualitative measurements compared the thermal condition of identical or similar objects under the same or similar operating conditions and observed the anomaly identified by the variation in intensity without assigning temperature. This technique was simple, and adjustment of the thermal imaging to compensate for atmospheric conditions or surface emissivity was not required. Quantitative measurements provided the temperature of the object. The condition of the object was determined by its temperature, the increase or decrease in temperature is compared to the background condition that has been predetermined (Holst, 2000).

The infrared ability to measure temperature is based on the Stefan-Boltzmann law that describes the total maximum radiation that can be released from a surface. In a thermal imaging system it is assumed that the target and its background are ideal blackbodies. However, real materials are not ideal blackbodies; their surface quality is described by their emissivities. The Stefan-Boltzmann law describes the total rate of emissions per unit surface area from agitated atoms that release their energy through radiation, given as follow:

$$M = \sigma T^4 \qquad \textit{(Equation 1)}$$

where T is the absolute temperature (K), and σ is the Stefan-Boltzmann constant, $5.6x10^{-8}$ ($m^{-2}K^{-4}$). The detector response is given by output voltage as following:

$$V_{detector} = kR_D M \qquad \textit{(Equation 2)}$$

$$V_{detector} = kR_D \sigma T^4 \qquad \textit{(Equation 3)}$$

where k is a constant that depends upon the specific design and R_D is the detector response (Holst,2000; Jacob, 2006).

The algorithm used by the camera's detector to measure temperature always assumes that the emissivity of the object is equal to unity. However, gases are considered gray bodies and the emissivity of gases are less than their unity. Therefore, the appearance temperature shown in the thermogram is not the real temperature of the gas because the correct value of emissivity is not used. In this research, the correct value of the emissivity is theoretically developed using the band absorption model to obtain the correct temperature measurement using infrared imaging systems.

2.2.2 Infrared Imaging Techniques for Methane Gas Visualization

2.2.2.1 Laboratory and Field Test of Methane Gas Detection using IR Imaging

The use of infrared camera for leak detection began in 1990 at a small company in Texas that wanted to improve its natural gas pipeline leak surveys. During this time, a 3 to 5 micrometer waveband camera was employed. However, the result was not a satisfactory due to the severely out of focus images the camera produced. This idea was continuously improved, and in 2002, the Merlin camera was built with a warm filter

operating at a center wavelength of 3.38 micrometers. It had limited success because it did not work during cloudy days and when thermal contrast was low. In 2003, the modification of the Merlin camera was constructed with a non-removable, built-in cold filter. The camera could detect more leaks as well as find leaks more quickly than the previous version. These results led to important milestones in VOC detection (Furry *et al.*, 2005).

Experiments on the utilization of infrared imaging for fugitive methane gas detection and visualization had been demonstrated by Gross *et al.* (1998). In their work, the methane gas from buried, leaky pipelines was monitored using Sterling, high resolution, PtSi Schottky barrier focal plane array infrared camera with 256 x 256 pixels and cooled to 77 K. The optical camera was operating at 3.32 μm wavelength, and a narrow band (0.16 μm) interference filter was placed in the camera detector in order to reduce the spectral range and enhance the sensitivity. The temperature resolution of the infrared camera was 0.1 – 0.01 K at 300 K background temperature. Methane emanating from a buried pipeline was simulated. A halogen lamp was used to irradiate the object region and a diffuse reflector was placed behind the target to reflect the infrared radiation to get a better contrast between the methane gas and the environment. The absorption of infrared radiation by the methane gas caused a reduction in radiation intensity, and the gas was detected as a flickering dark cloud in front of uniform background. The test by Gross *et al*. (1998) was conducted under a controlled environment, therefore wind-force and moisture level was considered negligible. A cloud with a diameter of 30 cm was observed and a methane concentration as low as

0.03 % could be detected. During the test, the gas flow rate was gradually decreased, and a gas mass flow rate as low as 0.1 L/min could still be recognized (Gross *et al.*, 1998).

A similar camera system had been applied to detect and monitor methane leaks from pipelines under realistic condition by Schulz *et al.* (2008). Infrared optical imaging was used to monitor leaks from a natural gas pipeline buried 1.2 m underground. The camera was able to recognize a leak as low as 2 L/min, under moderate weather conditions, and with a 2 m/s wind speed. The cloud diameter was measured at 50 cm during the observation (Schulz *et al.*, 2008).

A test of the sensitivity of an infrared camera to detect methane gas was also performed by Benson *et al.* (2006b). They employed a cell with infrared optical imaging to evaluate the IR absorption characteristics of methane gas. The test was conducted in a laboratory where wind force was negligible. The study showed that a methane gas concentration as low as 275 ppm could be distinguished by the infrared detector (Benson *et al.*, 2006b).

In the oil and gas industry, optical infrared imaging techniques have been applied to the survey of VOC releases from equipment and pipelines. Total E&P Indonesia had utilized an infrared camera system to monitor and repair major and minor releases of benzene, toluene, ethyl benzene and xylene. The camera had a spectral range of 1 – 5 μm, a 30x30 InSb detector with 320x240 pixel array, and operated at near the liquid nitrogen temperature. The integration time of this infrared camera was 5 to 16.5 ms, and the noise equivalent temperature difference (NETD) was 18 mK. The surveys were carried out for the purpose of protecting the operators from toxic chemical releases and

minimizing the environmental impact of hydrocarbon leaks in the facility. Leaks from valves, flanges, connectors, stuff boxes and other equipment were exhaustively detected within the 1500 km^2 operation. Using this method, they identified 500 unknown leaks from 2100 fugitive emissions sources. Depending on wind conditions, leaks between 3 to 6 g/h can be detected using this system (Plisson-Saune *et al.*, 2008).

Table 2. Summary of Previous Tests of Infrared Imaging Application for Methane Gas Detection and Visualization

	Type of test	Weather condition	Minimum detectable flow rate	Minimum detectable concentration	Size of cloud
Gross *et al.* (1998)	Laboratory	-	0.1 L/min	300 ppm	30 cm
Schulz *et al*. (2008)	Real field	Mild, 2 m/s	2 L/min	-	50 cm
Benson *et al*. (2006b)	Laboratory	-	-	275 ppm	-

Based on the available data of the application of infrared imaging techniques for gas detection, the capability of infrared cameras to detect the minimum flow and concentration of methane gas is summarized in Table 2. The table shows that that locations and prevailing weather conditions are among the most determining factors of an infrared camera's performance. The test, which was carried out indoors, in a controlled environment, resulted in higher sensitivity, whereas the sensitivity drops by a factor of two in the tests conducted under real weather conditions.

2.2.2.2 Field Test of LNG Vapor Visualization

Leake *et al.* (2005) provided initial results from employing UV/IR video imaging for gas absorption. The IR camera used in their tests was the HAWK camera system built by Leak Surveys Inc. It consisted of a modified Indigo Merlin MID camera with a spectra range of 1 – 5.4 μm. The detector is made of 30 x 30 μm indium antimonide (InSd) with a 320 x 256 pixel array. The *Sterling* cooler system was used, and provided the system with NEDT of no more than 18 mK, hence the sensitivity was relatively high. The camera consists of the optical module for image information, the detection module for conversion of the optical image into an electrical signal, and the electric module for conditioning and data processing. The role of the optical module is to concentrate the radiation energy from the target object to form an image in the focal plane. It consists of lenses and mirrors made of materials which have high refractive indexes such as germanium, silicon, zinc sulfide, etc (Leake *et al.*, 2005).

The detection module determines the overall performance of the camera system. There are different types of detector systems, single cell and focal plane array. The camera used in the experiment had the focal plane array detector system. Scanning devices consist solely of mirror or refractive elements, or a combination of both. The materials used for making the detectors are indium antimonide (InSb), platinum silicate (PtSi) or cadmium-mercury telluride (HgCdTe).

In order to reduce the noise from the environment, the detectors used in the infrared camera system are cooled to 77 K by the circulating nitrogen. The disadvantage of this cooling system is that the liquid has to be continuously circulated.

The role of the electronic module is to amplify the signal delivered by the detector and convert it to the format compatible to peripheral devices. This module's task is also to perform signal conditioning and image processing. This module consists of preamplifier, conditioning circuitry, image manipulation and signal format processor.

The spectral range of the HAWK camera was limited to detect several hydrocarbon infrared absorptions. It operated in the mid-wavelength infrared radiation (3 to 5 μm). The narrow band of the filter could not detect absorption less than the gas phase hexane.

Liquefied natural gas (LNG) is present in cryogenic conditions or sub-zero temperatures. Since the temperature is the measure of how fast a molecule is oscillating, a cooler object will show slower oscillations. Therefore, the HAWK camera used in the experiment captured the energy emitted by the background relative to the cold cloud and converted it to a real-time image display. The cold gas appeared as a darker area relative to the lighter background. This gas imaging system is calibrated to convert the radiation energy into temperature measurement units.

The result of their experiment showed that the invisible hydrocarbon (methane) vapor actually surrounded the white condensate cloud that formed once LNG spill onto the ground. The visible condensate was much heavier than the methane cloud and essentially attached to the ground, but its motion was strongly influenced by the wind.

Another interesting outcome of this experiment was how the LNG spill burned when it was caught by an ignition source. When the LNG reached its flammable range, the outside part burned faster so that the flame encircled the remaining vapor before burning all the way to the source (Leake *et al.*, 2005).

2.2.3 Emissivity Evaluation of Grey Gases

Emissivity is an important physical property in heat transfer, particularly when thermal radiation is significant. In the application of an infrared imaging system, the value of gas emissivity is important in determining the actual amount of radiation that is emitted from the object to the camera detector. Emissivity is defined as the ratio of the actual energy emitted from a surface to the energy emitted by a blackbody at the same temperature. The total emissivity of a gas can be estimated if experimental data of monochromatic emissivity is available. The monochromatic emissivity is defined as:

$$\varepsilon_{\lambda i} = \frac{E_{\lambda}}{E_{b\lambda}} \qquad \textit{(Equation 4)}$$

where E_{λ} is the actual monochromatic emissive power (energy per unit area at a particular wavelength) for an object surface and $E_{b\lambda}$ is the emissive power of blackbody at that temperature given by Planck's equation (Barron, 1999; Caniou, 1999).

Planck's radiation law describes the energy $E_{b\lambda}$ emitted per unit volume by a cavity of a blackbody in the wavelength interval λ to $\lambda+\Delta\lambda$ at a temperature T. The Planck function is given as the following equation:

$$E(T) = \frac{8\pi hc}{\lambda^5} \frac{1}{exp(hc/kT_g\lambda)-1} \qquad \textit{(Equation 5)}$$

where

h is the Planck's constant = $6.6260693 \times 10^{-34}$ Joule·second,

c is the speed of light = 2.99792458×10^{8} m.s^{-1} and

k is the Boltzmann constant= $1.380\,6504 \times 10^{-23}$ Joule.K^{-1}

(Siegel & Howell, 2002).

The total energy emitted per unit area is given as:

$$E = \int_0^\infty \varepsilon_\lambda \left(T_g, X, \lambda\right) E_{b\lambda}\left(T_g, \lambda\right) d\lambda \qquad \textit{(Equation 6)}$$

and eventually total emissivity may be calculated from its definition as follow:

$$\varepsilon_T = \frac{E}{E_b} = \frac{\int_0^\infty \varepsilon_\lambda(T_g,X,\lambda) E_{b\lambda}(T_g,\lambda) d\lambda}{\int_0^\infty E_{b\lambda}(T_g,\lambda) d\lambda} = \frac{\int_0^\infty \varepsilon_\lambda(T_g,X,\lambda) E_{b\lambda}(T_g,\lambda) d\lambda}{\sigma {T_g}^4} \qquad \textit{(Equation 7)}$$

(Lee & Happel, 1964).

In the past there were three general approaches developed to determine the emissivity and absorptivity of gas, namely theoretical calculation, the total energy method and the absorption band model. In theoretical calculation, gas emissivity is determined from the gas molecular transition energy. The molecular transition can be in the form of changes in electronic, vibrational, or rotational energy. A radiating gas emits energy in a range of defined frequencies and each individual transition contributes within this range. The total radiation is the sum of the radiation intensities corresponding to these individual transitions. Theoretical calculations require knowledge of quantum statistic, frequencies corresponding to individual transitions, the spectral line as a

function of temperature and pressure and the intensities of radiation related to the transition probabilities (Ostrander, 1951). The theoretical calculations of gas emissivities had been performed in the past for carbon monoxide (Penner *et al.*, 1952), nitric oxide (Benitez & Penner, 1950), hydrogen chloride (Penner & Gray, 1961) and carbon dioxide (Malkmus, 1963).

Using the total energy method, gas emissivity is calculated from the total energy radiated from a gas and the absorptivity is determined from the attenuation of blackbody radiation from the intervening gas. Hottel & Sarofim (1970) developed this method to estimate the total emissivity and absorptivity of water vapor within a non-radiating gas. In this method, the radiating gas is assumed to have a hemispherical volume at a uniform temperature and the correlation of the gas emissivity with the temperature, partial pressure, total pressure of the entire gas, and the radius of the hemisphere is determined (Hottel & Sarofim, 1970). A similar method also has been applied by Smith, Shen and Friedman for water vapor and carbon dioxide system (Smith *et al*., 1982).

The absorption band model, also known as the band energy method, was developed by Goody (1952) and separates the energy spectrum into individual bands where the gas is active. The band energy method takes into account the effect of temperatures within the active spectra of the gas. It generates the band emissivity and absorptivity in each individual band and their sums will result in total emissivity and absorptivity of the gas. This method has been applied in the past for carbon dioxide and water vapor (Howard *et al.*, 1963), methane at high temperatures (Brosmer & Tien, 1984) and carbon dioxide (Howard *et al.*, 1956; Pierluissi & Maragoudakis, 1986).

2.2.3.1 Emissivity Evaluation of Methane Gas

The emissivity of the methane gas at temperatures between 300 – 3000 K have been presented in the past (Lee & Happel, 1964). The emissivity of methane was evaluated using the band absorption method developed by Elsasser. The total emissivity is obtained by summing the band emissivity from all the bands which give signification contribution to radiation emitted by the surface:

$$\varepsilon_T(T_g, X) = \sum_i \varepsilon_{\lambda i}(T_g, X) \qquad \textit{(Equation 8)}$$

The band emissivity can be described as a function of the average blackbody radiance and the absorption band and the temperature of the gas of interest as given in the following equation:

$$\varepsilon_\lambda(T_g, X) = \frac{\bar{E}_\lambda(T_g, \bar{\lambda}_i) A_i(T_g, X)}{\sigma {T_g}^4} \qquad \textit{(Equation 9)}$$

where A_i is the band absorption of the *i*th band (Modest, 2003).

The mathematical expression of band absorption, A_i, was developed by Elsasser with the assumptions that spectral lines have equal intensity, line centers are equally spaced, spectral half-width is constant for all lines, and the line shape may be described by collision-broadening contour. The application of the Elsasser model requires the knowledge of the effective band width and its dependency of the band width on the temperature (Lee & Happel, 1964).

In its spectral line, methane has a nonzero spectral emissivity within several narrow regions and the blackbody radiation does not vary significantly in each region,

thus the average blackbody radiant energy evaluated in the center of the narrow band can be used for the entire band width.

$$J_{max} = \sqrt{\frac{10.235KT_g}{B_0 hc}} \qquad \textit{(Equation 10)}$$

Methane has active infrared absorption regions in three wavelengths, 2.37, 3.31 and 7.65 microns. The 2.37 micron band is considered as the weak, or non-overlapping, band whereas the 3.31 and 7.65 microns are considered the strong, or overlapping, band. Penner *et al.* (1952) developed a modification of the Elsasser method to calculate the effective bandwidth, which was applied to the 3.31 and 7.65 micron bands of methane. The effective band width is defined as the frequency interval in which the spectral lines have an intensity of at least 0.1% of the strongest line in the corresponding branch of the vibration-rotation band. The intensity of the lines in the vibration-rotation band at a constant temperature is characterized by the rotational quantum number J (Lee & Happel, 1964).

For the harmonic-oscillator rigid-rotator model, the selection rule for a radiation transition, which is governed by $\Delta J = \pm 1$, can be applied. From the Planck's relation, the spectral line location can be derived as:

$$\upsilon = 2BJ' \qquad \textit{(Equation 11)}$$

where *J'* is any quantum number and *B* is the rotational constant given as:

$$B = \frac{h}{8\pi^2 Ic} \qquad \textit{(Equation 12)}$$

In the selection rule, any molecules advancing from level *v* to *v'* can go either to the next higher rotational level $\Delta J = +1$ or lower rotational level $\Delta J = -1$ with the same probability. Molecular vibrations can generate an oscillating electric dipole moment that is sufficient for both rotational and vibrational transitions, which occur simultaneously. However, since the vibrational transition energy is much larger than the rotational transition energy, the spectrum of the combined transitions results in an array of rotational lines that group around the vibrational wavenumber (Lee & Happel, 1964)

Table 3. Infrared Bands of Methane (Lee & Happel, 1964)

Band region	Vibrational state	Wavenumber, ω (cm^{-1})	Integrated band intensity, α (cm^{-2}-atm^{-1})
	$v_2 + v_3$	4546	1.26
	$v_3 + v_4$	4313.2	3.7
	$v_1 + v_4$	4216.3	4.4
2.37 μ	$v_2 + 2v_4$	4123	0.16
	v_3 fundamental	3019.3	300
	$v_2 + v_4$	2823	
3.31 μ	$2v_4$	2600	
7.65 μ	v_4 fundamental	1306.6	150

The group with the lower energy level $(\Delta J = -1)$ and corresponding with lower wavenumber portion of the band is called P-branch and the group with higher energy level $(\Delta J = +1)$ is called R-branch. The branch that occurs in the vibrational energy itself, $\Delta J = 0$ is, called Q-branch. The Q-branch does not have any effect on the effective band width. Several simultaneous transitions for CH_4 molecules are given in Table 3.

From Table 3, it can be indicated that for the 3.31 μ region, the R-branch of the v_3 determines the upper limit and the P-branch of v_2 + v_4 sets the lower limit. For the 7.65 μ region, the R-branch of the v_4 determines the upper limit and the P-branch of v_4 sets the lower limit. Since the 2.37 μ region has low intensity, the temperature does not have significant effect to the effective band width. The effective band width for both 3.31 and 7.56 μ band regions are given as following equations:

$$\Delta_{\omega 3.31\mu} = \omega_{\nu_3(R)}(J_{max}) - \omega_{\nu_2+\nu_4(P)}(J_{max}) \qquad \textit{(Equation 13)}$$

$$\Delta_{\omega 7.65\mu} = \omega_{\nu_4(R)}(J_{max}) - \omega_{\nu_4(P)}(J_{max}) \qquad \textit{(Equation 14)}$$

The expression of the band absorption and band emissivity for the strong or overlapping band of methane is given as:

$$A_i = \Delta\omega_i(T_g) erf\left\{C_{i0}\left(\frac{T_g}{T_{g0}}\right)^{\xi_i}\sqrt{X}\right\} \qquad \textit{(Equation 15)}$$

$$\epsilon_i(T_g, X) = \frac{\bar{E}_\omega(T_g, \bar{\omega}_i)}{\sigma {T_g}^4}\Delta\omega_i(T_g) erf\left\{C_{i0}\left(\frac{T_g}{T_{g0}}\right)^{\xi_i}\sqrt{X}\right\} \qquad \textit{(Equation 16)}$$

and for the weak or non-overlapping band is given as:

$$A_i = D_{i0}\left(\frac{T_g}{T_{g0}}\right)^{\xi_i+\zeta_i}\sqrt{X} \qquad \textit{(Equation 17)}$$

$$\epsilon_i(T_g, X) = \frac{\bar{E}_\omega(T_g, \bar{\omega}_i)}{\sigma {T_g}^4} D_{i0}\left(\frac{T_g}{T_{g0}}\right)^{\xi_i+\zeta_i}\sqrt{X} \qquad \textit{(Equation 18)}$$

The emissivity of methane at higher temperature was successfully evaluated using this method (Lee & Happel, 1964).

2.2.3.2 Emissivity Evaluation of a Mixture of Grey Gases

Several atmospheric gases absorb and emit radiation within the mid-wave infrared range. When the infrared imaging is used to visualize methane gas, some other gases, such as water vapor and carbon dioxide, will influence the radiation transmitted to the camera detector.

The absorbance of methane at the infrared range is shown in Figure 3. In the mid-wave infrared range, methane has strong absorptions at wavelength 3000 cm^{-1} and 1700 cm^{-1}.

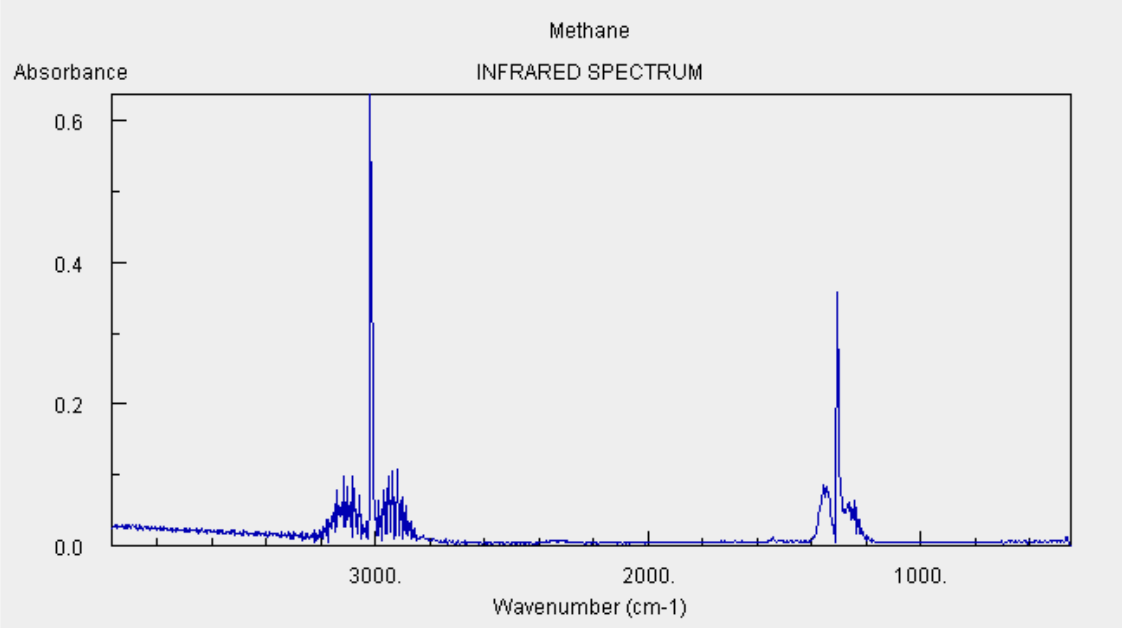

Figure 3. Methane Absorbance in the Infrared Range (Source: webbook.nist.gov)

Absorption of infrared radiation at the mid wave range by water molecule is shown in Figure 4. Water has active absorptions at the wavelength 1500 cm^{-1} and 3500 cm^{-1}.

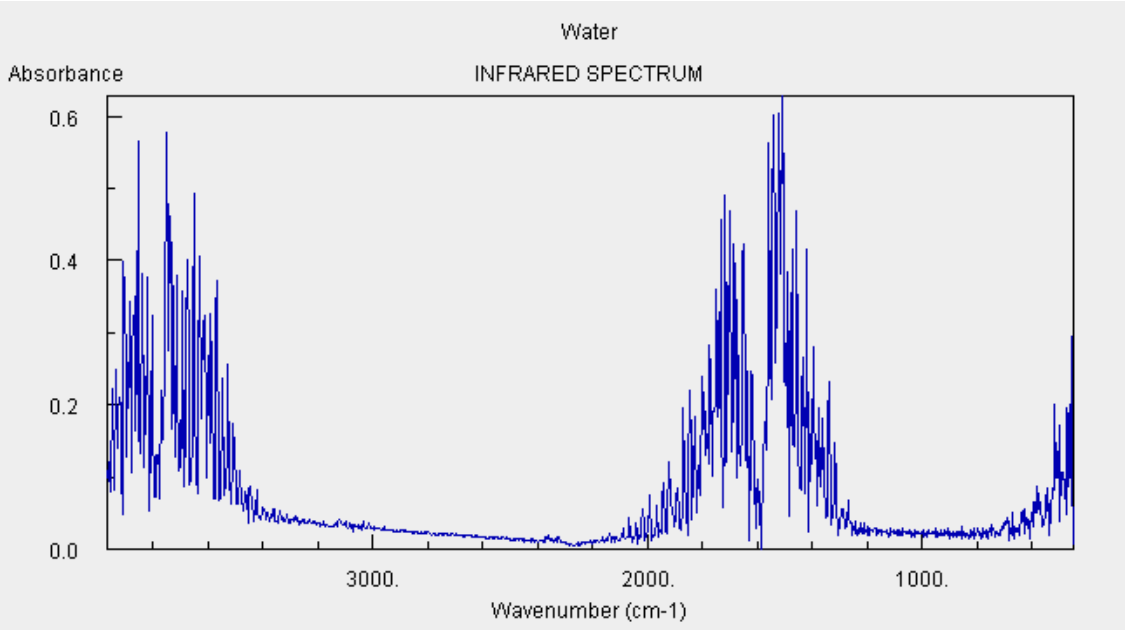

Figure 4. Water Absorbance in the Infrared Range (Source: webbook.nist.gov)

Absorption of infrared radiation at the mid wave range by carbon dioxide is shown in Figure 5. Carbon dioxide has a strong absorption at the wavelength 2200 cm^{-1}.

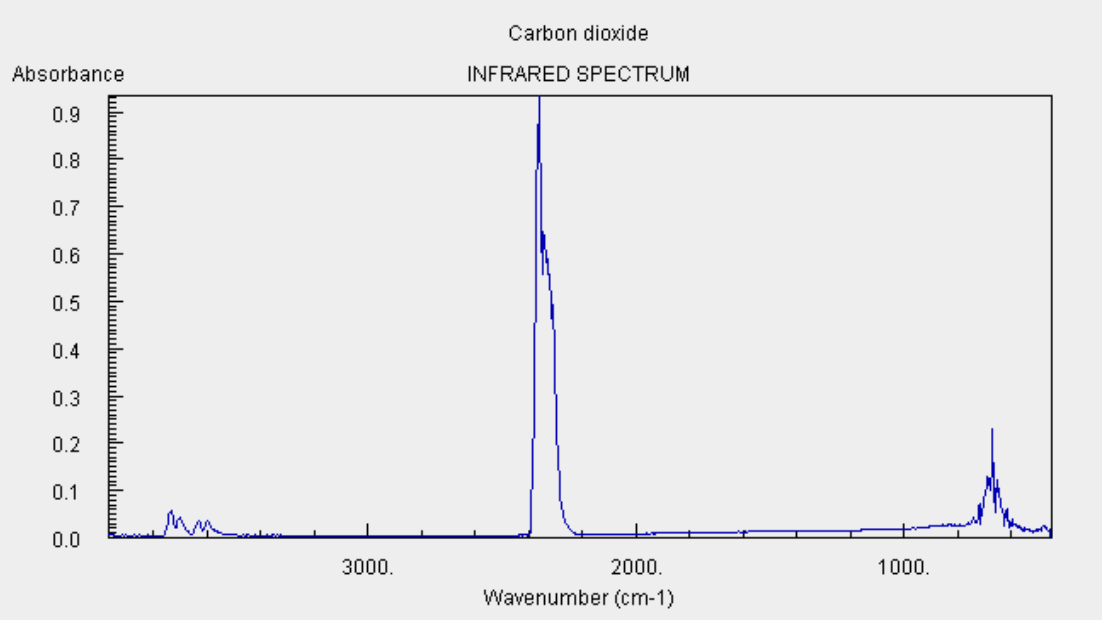

Figure 5. Carbon Dioxide Absorbance in the Infrared Range (Source: webbook.nist.gov)

Much of the available literature performed studies on the emissivity of mixtures of atmospheric gases. For instance, the emissivity of carbon dioxide in the 4.3-μ band for temperatures ranging from 300 – 3000 K was evaluated (Malkmus, 1963). In his work, a simplified model to compute the emissivity using the harmonic oscillator approach was developed. The model could be used to predict the radiation emitted in the 4.3-μ band of carbon dioxide for a given pressure and optical path length. The results of this model had been compared to the experimental data and other theoretical calculations and had shown a good agreement. Figure 6 shows the relation of the emissivity to the optical length for carbon dioxide studied by Malkmus (1963).

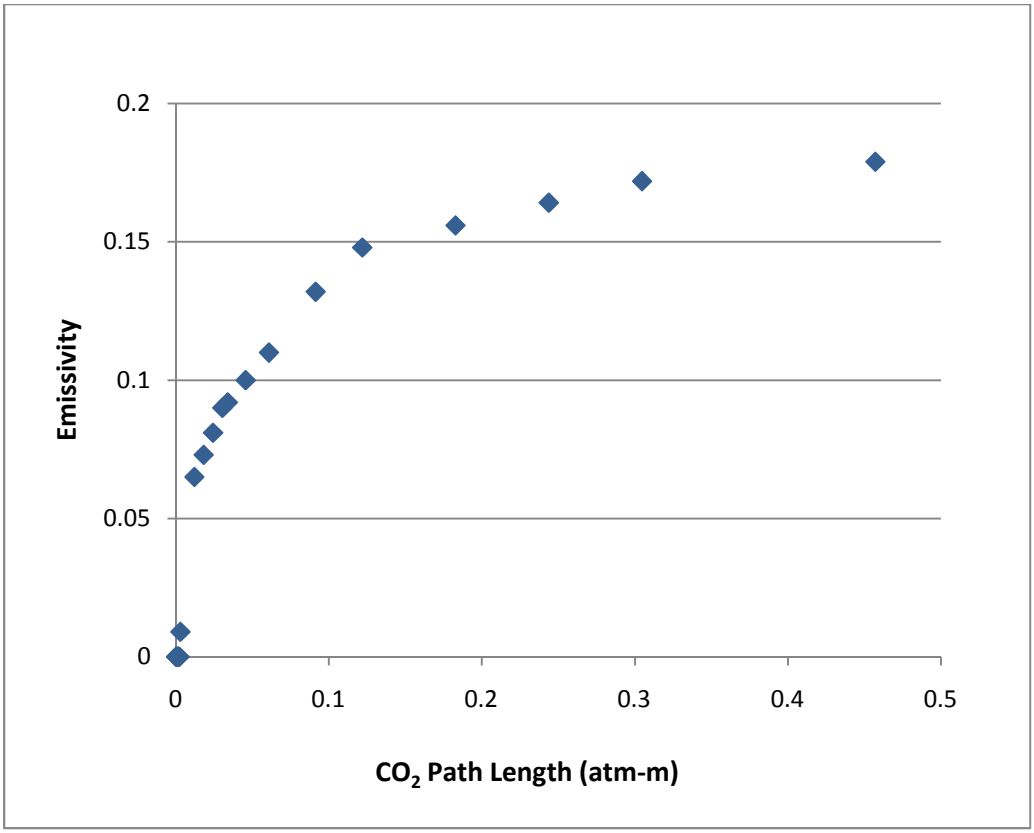

Figure 6. Emissivity of Carbon Dioxide as a Function of Optical Length at 298 K (Adapted from Malkmus, 1963)

Emissivity of homogeneous gases was generally presented in a diagram or chart which provided the correlation of the emissivity to the temperature and path lengths. However, due to the complexity of the gas spectra, the accuracy of the emissivity values over spectral regions was rather poor, and the diagrams or charts generally cannot be used as a standard because the extrapolation of the data might result in significant errors. Therefore, Leckner (1972) performed a comparison between the total emissivity charts and the total emissivity calculated from spectral data (Leckner, 1972).

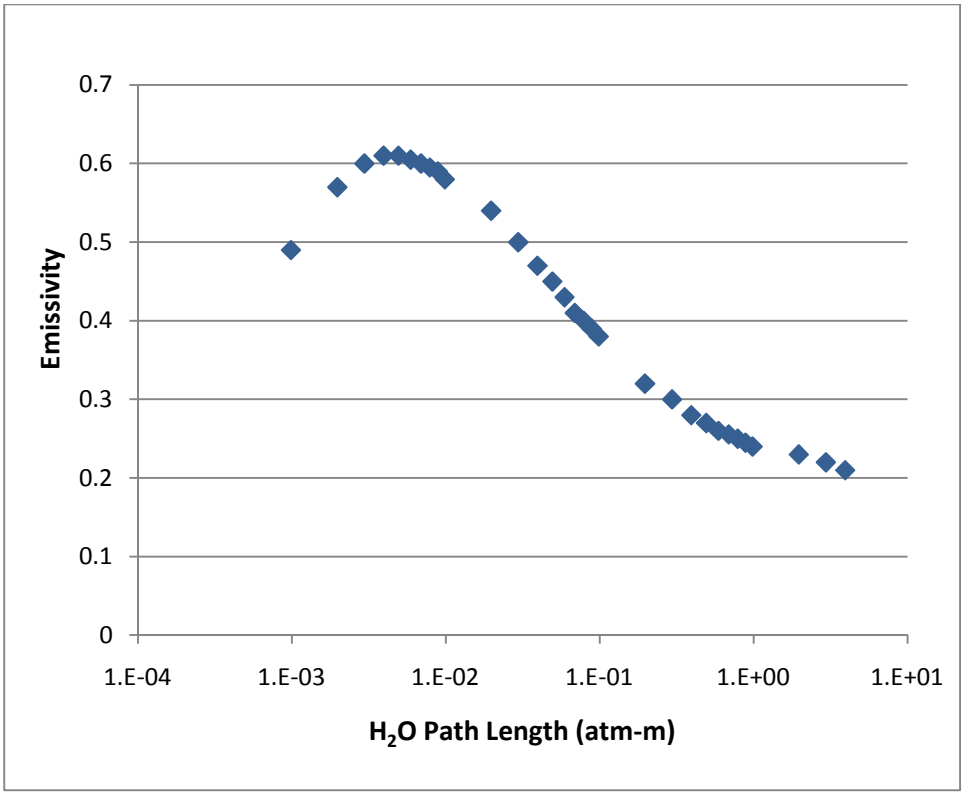

Figure 7. Emissivity of Water Vapor as a Function of Optical Length at 298 K (Adapted from Leckner, 1972)

For water vapor, total emissivity from the calculation showed a reasonably good agreement with the experimental data with a discrepancy of less than 10%. The emissivity of water vapor at different wavelengths is given in Figure 7. However, the total emissivity of carbon dioxide showed a higher discrepancy, especially in the weak band region which Leckner described as a result of the absorption in the air-layer that could have been present during the measurement using the radiometer (Leckner, 1972).

Another study on the emissivity of water vapor, carbon dioxide and ozone was conducted (Staley & Jurica, 1970). The flux emissivities of these three components were

evaluated by adapting the Elsasser's band absorption model in order to calculate the wavelength-dependent absorption coefficients and flux transmissivities. In the temperature range from -40 to 20 °C, the total water vapor flux emissivity is not significantly influenced by the temperature but increases rapidly with optical depth. The flux emissivity of carbon dioxide is a weak function of the temperature. However, the emissivity increased significantly with the increase in optical depth (Liou, 2002).

Infrared camera detectors received heat fluxes that emanated from a target object, other objects in the atmosphere, atmospheric gases and/or components in the camera and then translated it into a temperature measurement. Absorption by atmospheric constituent plays an important role in attenuating the radiation absorbed and emitted by the target object. It is evident from the laboratory experiment that at an ambient temperature of 15 °C and 50% humidity, the absorption by carbon dioxide and water vapor is observable at optical distance range 1 – 10 m (Minkina & Dudzik, 2009). The atmospheric transmittance will vary greatly depends on the environmental and meteorological conditions, such as relative humidity in the atmosphere, ambient temperature, prevailing wind rose and the distance between the camera detector and target object.

An infrared camera is able to detect gas leaks from pipelines, components or equipment. The camera detector translates the radiative power from the target object into a voltage reading. The amount of radiation emitted by the target gas depends on its emissivity, which strongly depends on the gas temperature and optical depth. Radiation

emitted from a black body object is described by the Stefan-Boltzmann law as given in Equation 1.

Equation 1 is used to describe the radiative power of a black body. However, since most objects particularly gases cannot be considered as a black body, the emissivity value of the target will determine the amount of radiation transmitted to the detector. Hence, grey body emissive power is given in the following equation:

$$P = \varepsilon\sigma T^4 \qquad \textit{(Equation 19)}$$

where ε is the emissivity of the target object.

The gas mixture emissivity can be evaluated by the weighted sum of the gray gases model (WSGGM) (Hottel & Sarofim, 1970). The WSGGM estimates the total emissivity and absorptivity by summing the gray gas emissivity weighted with a temperature dependent factor. The emissivity of the gray gas is expressed in terms of the temperature-independent absorption coefficient, gas partial pressure and path length as given in the following expression:

$$\epsilon = \sum_{i=0}^{I} a_{\epsilon,i}(T)\,[1 - e^{-k_i PL}] \qquad \textit{(Equation 20)}$$

where the notation $a_{\varepsilon,i}$ refers to the emissivity weighting factors for *i-th* gray gas as a function of temperature, *T*. The term in the bracket gives the emissivity value for the *i-th* gray gas with k_i denotes the absorption coefficient and *PL* is the product of the sum of partial pressures of the absorbing gases in the gas mixture, *P* and optical length, *L*. The physical understanding of the weighting factors, $a_{\varepsilon,i}$ is a fractional amount of blackbody energy in the spectral region where the gray gas absorbs. The sum of the weighting

factor must be equal to one. At *i=0*, the absorption coefficient, k_i, is equal to zero. The weighting factor at *i=0* is given as:

$$a_{\epsilon,0} = 1 - \sum_{i=1}^{I} a_{\epsilon,i} \qquad \textit{(Equation 21)}$$

Only *i* number of weighting factors need to be calculated. The temperature-dependent weighting factor is a polynomial of order *J-1* expressed as the following:

$$a_{\epsilon,i} = \sum_{j=1}^{J} b_{\epsilon,i,j} T^{j-1} \qquad \textit{(Equation 22)}$$

where $b_{\varepsilon,I,j}$ represent the emissivity gas temperature polynomial coefficients (Smith *et al*., 1982; Park & Kim, 2003).

Beer, Foster and Siddall (1971) developed a gray gas model which took into account the contribution of other gases, such as carbon monoxide and unburned hydrocarbons, in addition to CO_2 and H_2O (Beer *et al.*, 1971). The unburned hydrocarbons such as methane are a significant contributor of radiation emitters and therefore will significantly affect the total emissivity of the gas mixture.

According to Beer, Foster and Siddall (1971) the *kiP* term in the WSGGM model is modified in the presence of other species by including the partial pressure of the hydrocarbon gas. For instance, the *kiP* in the presence of methane gas in the atmosphere can be expressed as:

$$k_i P = k_i\left(P_{CO_2} + P_{H_2O}\right) + k_{CH_4} P_{CH_4} \qquad \textit{(Equation 23)}$$

The value of the polynomial coefficients and absorption coefficients are given in Table 4. The coefficients are given for three components gas mixture and four components gas mixture.

Table 4. Coefficients for Gray Gas Mixture Emissivity Calculation (Beer *et al.*, 1971)

I	i	$b_{\varepsilon,i,1}$	$b_{\varepsilon,i,2}$	k_i	$k_{HC,i}$
3	1	0.437	7.13	0.0	3.85
	2	0.390	-0.52	1.88	0.0
	3	1.173	-6.61	68.83	0.0
4	1	0.364	4.74	0.0	3.85
	2	0.266	7.19	0.69	0.0
	3	0.252	-7.41	7.4	0.0
	4	0.118	-4.52	80.0	0.0

2.2.4 Semi-quantification of Gas Emission Rate from the Application of IR Camera for Gas Detection

A semi-quantitative approach to determine the mass emissions rate of a hydrocarbon gas release has been developed. The work focused on obtaining new emission factors for hydrocarbon gas releases when an optical imaging technique was used for leak detection. This new emission factor was derived to replace the emission factors from EPA Protocol 1995. Field data and Monte Carlo statistical simulation techniques were applied to obtain the emission factor for valve, pump, connector, flange and instrument leaks ranging from 3 – 60 g/h. Components were categorized into "leaker" and "non-leaker," based on the gas mass flow rate relative to the lowest flow rate, which can be detected by infrared camera. The emission factors were calculated for 3, 6, 30 and 60 g/h detection threshold (Lev-On *et al.*,2007).

The semi-quantitative method is used to determine emission factors for different components was a suitable approach to estimate the total mass emission rate of fugitive gas released from leaking components. However, this method evaluated the emission factor of a component by comparing the leak rate to the lowest threshold, or sensitivity level, where the camera detector responded. The emission factor was calculated by summing the total emissions divided by the total count of the components. Furthermore, this semi-quantitative measure was general for all hydrocarbons that an infrared camera could detect. This method was not able to identify the correlation between the sizes of detected gas plumes and the emissions rate for a specific gas. Different gases have different characteristic when released to the atmosphere. Some gases are denser than air and have a tendency to stay on the ground before eventually warming and lifting up, whereas, other gases are lighter than air and rise when released into the atmosphere. Accurate quantitative measures for specific gases is important, and therefore, this paper proposes a solution for estimating the gas mass flow rate of methane emissions based on a dispersion modeling approach.

2.2.5 Methane Gas Discharge from a Leak in a Pipeline

For a relatively short pipe, the gas flowing through a pipeline is generally calculated with the assumption of adiabatic flow behavior, where no heat transfer occurs between the system and its surroundings. Assumption of isentropic behavior of

compressible fluid flow through a frictionless nozzle is usually valid (Perry, 2008). Figure 8 illustrates the process of gas being released and dispersed from a leaky pipeline.

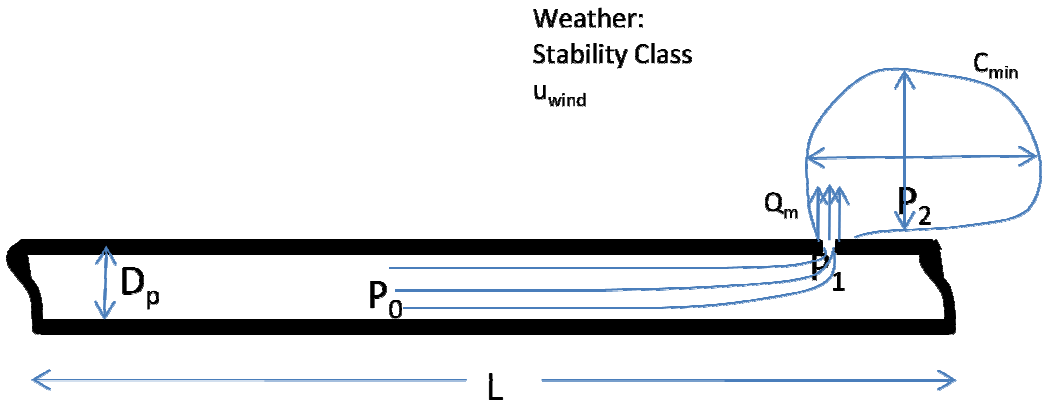

Figure 8. Flow Process of Gas Leak in a Pipeline

The gas release rate is calculated using equations for the flow of compressible gas through frictionless nozzles, which are readily available in the literature, by assuming stagnant upstream conditions, i.e. constant upstream pressure and temperature. It is important to specify the critical conditions prior to calculating the gas flow rate coming from the leak. The critical condition of the gas flow is achieved if the exit velocity of the gas is equal to the speed of sound. For ideal gas, the speed of sound is given as:

$$c = \sqrt{\frac{kRT}{MW}} \qquad \textit{(Equation 24)}$$

where:

k is the ratio of the specific heats, $C_p/C_{v,}$

R is the gas constant (3.314 kJ $kgmol^{-1}$ K^{-1}),

T is absolute temperature (K), and

MW is the molecular weight (kg $kgmol^{-1}$)

(Perry, 2008).

The term Mach number is introduced as a dimensionless parameter that compares the velocity of gas to the velocity of sound. When the flow is critical, or chocked, the Mach number is equal to one.

$$Ma = \frac{u}{c} \qquad \textit{(Equation 25)}$$

The criticality of the flow is determined by following equation:

$$\frac{P_{choked}}{P_0} = \left(\frac{2}{k+1}\right)^{k/k-1} \qquad \textit{(Equation 26)}$$

where P_0 is the pressure of the gas inside the pipeline.

If the downstream pressure, P_2, is higher than the choked pressure, P_{choked}, the flow is non-critical and the exit pressure, P_1, will be the same as the surrounding pressure, P_2. The mass flux rate is calculated from the equation for subsonic flow, as given in the following:

$$G = P_0\sqrt{\frac{k\,MW}{RT_0}}\frac{Ma_1}{\left(1+\frac{k-1}{2}Ma_1\right)^{(k+1)/(k-1)}} \qquad \textit{(Equation 27)}$$

(Crowl & Louvar, 2002).

For subsonic flow, the Mach number can be obtained from the pressure correlation given in the following equation:

$$\frac{P_0}{P_1} = \left(1 + \frac{k-1}{2} Ma_1^2\right)^{k/k-1} \quad \textit{(Equation 28)}$$

The property relations for the isentropic process are given as:

$$\frac{\rho}{\rho_0} = \left(\frac{P}{P_0}\right)^{1/k} \quad \textit{(Equation 29)}$$

and:

$$\frac{T}{T_0} = \left(\frac{P}{P_0}\right)^{(k-1)/k} \quad \textit{(Equation 30)}$$

(Smith *et al.*, 1996).

If the downstream pressure, P_2, is lower than the choked pressure obtained from Equation 26, the gas flow becomes sonic, or choked. If this occurs, the exit pressure, P_1, is equal to P_{choked}. The exit velocity is equal to the speed of sound, and the maximum flow rate is attained when choked flow occurs. The maximum mass flux of gas discharged from the leak source is given as:

$$G = P_0 \sqrt{\frac{k\ MW}{RT}\left(\frac{2}{k+1}\right)^{(k+1)/(k-1)}} \quad \textit{(Equation 31)}$$

(Crowl & Louvar, 2002).

2.2.6 Vapor Dispersion Model

The dispersion model can be used to illustrate the transport phenomena of gas or vapor released from its source into the atmosphere. The vapor will be at its highest concentration at its release point and will continuously decrease as it is carried

downwind. The atmospheric dispersion is calculated by solving the conservation equations of mass, energy and momentum. Depending on the gas density, the light (buoyant) or dense gas dispersion model may be applied (Hanna & Drivas, 1987). The equation of continuity (conservation of mass) is given as:

$$\frac{\partial \rho}{\partial t} + (\nabla \cdot \rho v) = 0 \qquad \textit{(Equation 32)}$$

For three dimensional Cartesian coordinate the equation becomes:

$$\frac{\partial p}{\partial t} + \frac{\partial}{\partial t}(\rho v_x) + \frac{\partial}{\partial t}\left(\rho v_y\right) + \frac{\partial}{\partial t}(\rho v_z) = 0 \qquad \textit{(Equation 33)}$$

The expression of the equation of energy is given as follow:

$$\frac{\partial}{\partial t}\left(\frac{1}{2}\rho v^2 + \rho \widehat{U}\right) = -\nabla \cdot \left[\left(\frac{1}{2}\rho v^2 + \rho \widehat{U}\right) v\right] - (\nabla \cdot q) - (\nabla \cdot pv) - [\nabla \cdot (\tau \cdot v)] + \rho(v \cdot g) \qquad \textit{(Equation 34)}$$

and the equation of motion (conservation of momentum) is described as:

$$\frac{\partial}{\partial t}(\rho v) = -(\nabla \cdot \rho vv) - \nabla p - (\nabla \cdot \tau) + \rho g \qquad \textit{(Equation 35)}$$

(Bird *et al.*, 2006).

For non-isothermal flow, the fluid density and viscosity depend on temperature and pressure. This variation in the density is important and cannot be neglected because it determines the buoyant force which results in convection of the fluid.

The buoyant force is obtained from the arrangement of the equation of state and the equation of motion to create the simplified *Boussinesq* equation. This form of equation of motion is very useful for analyzing heat transfer phenomena.

$$\rho \frac{Dv}{Dt} = (-\nabla p + \bar{\rho} g) - (\nabla \cdot \tau) - \bar{\rho} g \bar{\beta} (T - \bar{T}) \qquad \textit{(Equation 36)}$$

in which

$$\beta = -\left(\frac{1}{\rho}\right)\left(\frac{\partial \rho}{\partial T}\right)_p \qquad \textit{(Equation 37)}$$

and

$$\bar{T} = \frac{1}{2}(T_1 + T_2) \qquad \textit{(Equation 38)}$$

There are important parameters which need to be identified prior to modeling vapor dispersion. Initially, the type of release incident must be developed to describe how the material is being released as well as the rate of the release, and the downwind concentration of the vapor can be determined thereafter. The factors that can affect the atmospheric dispersion are (Macdonald, 2003; Crowl & Louvar, 2002):

1) Wind speed

   The plume becomes longer and narrower and the substance is diluted faster as the wind velocity increases due to larger quantities of air.

2) Atmospheric stability

   The amount that gas mixes with air as it moves vertically is highly dependent on the stability of the atmosphere. During the day, temperature decreases with height very rapidly, therefore the vertical movements of air are also very fast. At night the temperature decreases less and as a result there is less vertical motion. There are three classes of atmospheric stability: unstable, neutral and stable. An unstable atmospheric condition occurs when the air temperature near the ground

is higher than the air temperature at elevated positions. This gives rise to unstable atmospheric conditions because the air below has a lower density than the air above it and it results in atmospheric mechanical turbulence. For neutral atmospheric stability, the air temperature difference does not influence the atmospheric mechanical turbulence. Neutral stability is obtained when the temperature near the ground is lower than the air temperature at higher elevations, and the air density below is higher than above. In this criterion, the buoyancy suppresses the mechanical turbulence.

3) Ground conditions

   Ground conditions have an effect on the mechanical mixing at and the wind profile.

4) Height of release above the ground

   The height of a release directly influences the concentration on the ground because the higher the release source the lower the ground-level concentration will be, as the vapor has to disperse a greater vertical distance.

5) Momentum and buoyancy of the initial material released

   The buoyancy and the momentum of the material alter the effective height of the release. For gas less dense than air, the release gas will have positive buoyancy and will move upwards and gas denser than air will sink toward the ground. The density of gas highly depends on the molecular weight and temperature.

2.2.6.1 Gaussian Dispersion Model

Gases that are less dense than air and have lower concentrations will form neutrally buoyant vapor dispersions as they are released and mixed with fresh air; their concentrations downwind can be predicted using this model. There are two types of neutrally buoyant vapor dispersion models that are frequently used: plume and puff models. The plume model represents the steady state concentration of material released from a continuous source and the puff model depicts the sequential concentration of material from a single release of a fixed amount of material.

$$C_i(x,y,z) = \frac{Q_{m,i}}{2\pi\sigma_y\sigma_z u} exp\left[-\frac{1}{2}\left(\frac{y}{\sigma_y}\right)^2\right]\left\{exp\left[-\frac{1}{2}\left(\frac{z-H}{\sigma_z}\right)^2\right] + exp\left[-\frac{1}{2}\left(\frac{z+H}{\sigma_z}\right)^2\right]\right\}$$

(Equation 39)

where:

Qm,i is source emission rate (m s^{-1}),

H is effective height of release (m),

σ_y is diffusion coefficient in y direction (m), and

σ_z is diffusion coefficient in y direction (m)

(Beychok, 1994; Yegnan, 2002).

The diffusion coefficients used are obtained from the stability classification by Pasquill and Gifford and determined by the amount of incident solar radiation and the wind speed. Table 5 gives the Pasquill-Gifford criteria to determine the stability class.

Table 5. Pasquill-Gifford Stability Classes (Gifford, 1976)

Surface wind speed	Daytime Solar Radiation			Nighttime conditions	
	Strong	Moderate	Slight	Thin overcast or > 4/8 low cloud	≤ 3/8 cloudiness
< 2	A	A-B	B	F	F
2 – 3	A-B	B	C	E	F
3 – 4	B	B-C	C	D	E
4 – 6	C	C-D	D	D	D
>6	C	D	D	D	D

Table 6 provides the equations to calculate the diffusion coefficients. The mixing between methane gas and air highly depends on the magnitude of wind speed and the surface roughness (Britter & Griffiths, 1982; Crowl & Louvar, 2002).

Table 6. Pasquill-Gifford Dispersion Coefficients for Plume Dispersion

Pasquill-Gifford Stability Class	σ_y(m)	σ_z(m)
Rural conditions		
A	$0.22x(1+0.0001x)^{-1/2}$	$0.2x$
B	$0.16x(1+0.0001x)^{-1/2}$	$0.12x$
C	$0.11x(1+0.0001x)^{-1/2}$	$0.08x(1+0.0002x)^{-1/2}$
D	$0.08x(1+0.0001x)^{-1/2}$	$0.06x(1+0.00015x)^{-1/2}$
E	$0.06x(1+0.0001x)^{-1/2}$	$0.03x(1+0.0003x)^{-1}$
F	$0.04x(1+0.0001x)^{-1/2}$	$0.016x(1+0.0003x)^{-1}$
Urban conditions		
A-B	$0.32x(1+0.0004x)^{-1/2}$	$0.24x(1+0.0001x)^{-1/2}$
D	$0.22x(1+0.0004x)^{-1/2}$	$0.2x$
D	$0.16x(1+0.0004x)^{-1/2}$	$0.14x(1+0.0003x)^{-1/2}$
E-F	$0.11x(1+0.0004x)^{-1/2}$	$0.08x(1+0.00015x)^{-1/2}$

2.2.6.2 Dense Gas Dispersion

The horizontal spreading of a dense gas is enhanced by gravity while vertical mixing is reduced by density stratification. Heat convection from the warm ground to the cold gas increases the cloud temperature. Heat convection is an additional source of turbulence and enhances the mixing of gas (Briscoe & Shaw, 1980; Nielsen, 2002).

As the gas cloud is mixed with air, the gas temperature will rise to its dew point where the liquefied gas evaporates. The idealized case of adiabatic mixing is when the cloud receives heat from no other source than the diluting air generally assumed upon dispersion of the gas. When a homogeneous equilibrium is assumed, the gas

concentration is equal to its partial pressure divided by the overall pressure according to the Dalton's law.

The mole budget provides the overall ratio of condensation given as:

$$\alpha_{tot} = \alpha . c + \alpha_w . q . (1 - c) \qquad \textit{(Equation 40)}$$

where

α is the degree of condensation for contaminant,

c is the concentration of contaminant (mole-mole^{-1}),

α_w is the degree of condensation for water vapor, and

q is the water concentration of diluting air (mole-mole^{-1}).

The phase composition depends on the mixture temperatures. The enthalpy budget can be used to calculate the phase composition as given in the following equation:

$$(T - T_a)\left[cMc_p + (1 - c)\left((1 - q).M_\alpha c_p^\alpha\right) + q.M_w c_p^w\right] + \Delta H_{con} = \Delta H$$

(Equation 41)

where

ΔH is the mixture enthalpy (J kg^{-1}),

Ta is the air temperature (K),

M, M_α and M_w is the molar weight for the gas mixture, air and water respectively (mole kg^{-1}),

c_p, $c_p{}^\alpha$ and $c_p{}^w$ is the heat capacities for the gas mixture, air and water respectively (J kg^{-1} K^{-1}), and

ΔH_{con} is the enthalpy change by condensation (J kg^{-1}) which is given by:

$$\Delta H_{con} = c\alpha ML + (1-c)q\alpha_w M_w L_w + \alpha_{tot}\Delta H_{mix} \quad \textit{(Equation 42)}$$

where

L and L_w is the latent heat of condensation for contaminant and water respectively,

ΔH_{mix} is the heat of reaction in non-ideal liquid mixtures (J kg^{-1})

(Nielsen, 2002).

The vertical mixing of the stratified gas is usually associated with the work against gravity which could dampen the turbulence kinetic. The local mixing rate depends on the concentration of the vertical gradient, which depends of the diffusion of the gas. Three dimensional numerical models, namely the k-ε model, are generally used to determine the turbulence diffusivity of dense gas.

Ermak *et al.* (1982) studied and compared three categories of the dense gas dispersion model for LNG spills:

1). Germalez-Drake (GD)Modified Gaussian plume model
2). SLAB or Box model, a layer-averaged conversion equation model with one spatial variable.
3). Computational Fluid Dynamic (CFD), a fully three dimensional conservation equation model that predicts the change in vapor concentration as a function of time and space (Ermak *et al.*, 1982).

These three level approaches to the vapor dispersion model are used to simulate the atmospheric dispersion of a cold, denser-than-air gas release. The GD model is based on a single species equation and neglects the momentum and energy effects in determining the vapor cloud dimensions. The SLAB model includes the conservation of

mass, momentum and energy in addition to the species equation, but it is time-averaged and neglects some parameters, such as the crosswind plane. In this case all properties of the vapor cloud only vary in the downwind direction. FEM3 is the most complete model among the three; it includes the conservation laws by treating the model explicitly in three dimensions.

Germalez-Drake Model

The GD model is the modification of the steady-state Gaussian plume, point source atmospheric release diffusion equation (Ermak *et al.*, 1982).

$$\frac{\partial C}{\partial t} + U\frac{\partial C}{\partial x} = K_y\frac{\partial^2 y}{\partial y^2} + K_z\frac{\partial^2 C}{\partial z^2} \qquad \textit{(Equation 43)}$$

This equation calculates the concentration of gas emitted to the atmosphere as a function of time and distance in the *x*, *y* and *z* directions. *U* is the wind velocity, assumed to be constant and one-directional (*x*-direction). K_y and K_z are the horizontal and vertical turbulent diffusivities, the turbulent diffusivity in x-direction is assumed to be negligible compared to wind advection.

The GD equation is solved by determining that the turbulent diffusivities, as well as the downwind distance *x*, are changing over time when the vapor is released. The concentration profile is obtained from the integration over a finite length of *L* normal to the wind direction and located at distance x_v, giving:

$$C(x,y,z) = \frac{\dot{V}v}{(2\pi)^{1/2}UL\sigma_z}exp\left(\frac{-z^2}{2{\sigma_z}^2}\right)\left(erf\left[\frac{\frac{L}{2}-y}{2^{1/2}\sigma_y}\right] + erf\left[\frac{\frac{L}{2}+y}{2^{1/2}\sigma_y}\right]\right) \qquad \textit{(Equation 44)}$$

where

V_v is the volumetric rate of vapor at ambient conditions,

σ_y, σ_z are the dispersion coefficients and are functions of both downwind distance from the source x and the virtual source distance x_v, and are related to the turbulent diffusivities by the expression:

$$\sigma^2(x + x_v) = \frac{2}{U}\int_0^{x+x_v} K(x')\,dx' \qquad \textit{(Equation 45)}$$

(Ermak *et al.*, 1982).

Germalez-Drake model uses the Pasquill-Gifford dispersion coefficients for the continuous ground level sources to determine σ_y and σ_z. The source length L and the virtual source distance x_v are determined by the gravity spread calculation for the cylindrically shaped volume of the vapor when compared to the real volume of vapor that evaporated in the time the wind moved along the liquid pool. The properties of the cylindrical cloud are assumed to be homogeneous, while the height, radius, temperature and density are changing with time due to the gravity spread of clouds more dense than air, air entrainment into the clouds, and surface heating of the clouds (Ermak *et al.*, 1982).

The cylindrical radius of the cloud increases due to the gravity spread; the rate of the increasing radius is given by:

$$\dot{R} = \left(2g\,\frac{(\rho-\rho_a)}{\rho_a}H\right)^{1/2} \qquad \textit{(Equation 46)}$$

where

g is the acceleration due to gravity,

ρ is the cloud density, and

ρ_a is the ambient air density.

In this model, air entrainment is assumed to occur only at the top of the cylindrical cloud. The rate of mass and energy transport for the cylindrical clouds are:

$$M = \pi \dot{\rho}_a R^2 \omega_e \qquad \textit{(Equation 47)}$$

$$\dot{E} = \pi \rho_a R^2 \omega_e C_{pa} T_a + \epsilon_v + \epsilon_w \qquad \textit{(Equation 48)}$$

where

ω_e is the entrainment rate,

c_p and T are the cloud specific heat and temperature,

c_{pa} and T_a are the ambient air specific heat and temperature,

ϵ_v is the heat condensation and

ϵ_w is the surface heat flux.

This equation is then combined with the time-independent ideal gas law to give the solutions as functions of time. Gas law approximations for the density and the specific heat are described as:

$$\rho = \frac{M_n M_a P}{RT(M_n + (M_a - M_n)\omega)} = \frac{MP}{RT} \qquad \textit{(Equation 49)}$$

$$C_p = C_a(1 - \omega) + C_{pn}\omega \qquad \textit{(Equation 50)}$$

The finite source length L is determined when the radial velocity of the cylindrical cloud R is equal to the wind velocity, and the virtual source distance x_v is found from the values of σ_y and σ_z at the concentration equal to the source center (0,0,0). When these values are known, the concentration of the vapor cloud as functions of time and space can be fully delineated.

SLAB Model

SLAB is the computer modeling that simulates the atmospheric dispersion of denser-than-air releases. In this model, the conservation equations are spatially averaged so as to treat the cloud as a steady state plume, a transient puff, or the combination of two depending of the duration of the release. For the long duration of the release, the cloud is treated as a steady state plume. In case of a finite duration release, initially the cloud dispersion is described using the steady state plume model and remains a plume when the source is still active, but once the source is off, the cloud is treated as a puff and the dispersion is calculated using the transient puff model.

The SLAB model treats the vapor as a well-defined cloud of height h and half-width B. Inside the cloud along the crosswind plane the properties are assumed to be uniform, they vary only with time and the distance of downwind direction. This allows the cloud to be defined as a slab or a layer-averaged property. For the cloud density, the expression becomes:

$$\bar{\rho}(x) = \frac{1}{Bh}\int_0^B dy \int_0^h dz\, \rho(xyz) \qquad \textit{(Equation 51)}$$

(Ermak *et al.*, 1982).

Cloud dispersion is assumed to occur due to the entrainment of air at the top and sides of the cloud and due to the gravity spread approximation. The heat and momentum transfer also occur at a cloud-ground interface. These assumptions give rise to the layer-averaged conservation equation for mass, momentum and energy.

$$\frac{\partial(\rho Bh)}{\partial t} + \frac{\partial(U\rho Bh)}{\partial x} = \rho_a v_e h + \rho_a \omega_e B + \rho_s W_s B_s \qquad \textit{(Equation 52)}$$

$$\frac{\partial \omega}{\partial t} + U\frac{\partial \omega}{\partial x} = \frac{\rho_a \nu_e \omega}{\rho B} - \frac{\rho_a \omega_e B}{\rho h} + \frac{\rho_s W_s B_s (1-\omega)}{\rho B h} \quad \textit{(Equation 53)}$$

$$\frac{\partial U}{\partial t} + U\frac{\partial U}{\partial x} = -\frac{g}{2\rho B h}\frac{\partial[(\rho-\rho_a)Bh^2]}{\partial x} - \frac{\rho_a}{\rho}\left(\frac{\nu_e}{B} + \frac{\omega_e}{h}\right)(U_a - U) - \frac{\rho_s W_s B_s}{\rho B h} - \frac{\tau_x}{\rho h} \quad \textit{(Equation 54)}$$

$$\frac{\partial V_g}{\partial t} + U\frac{\partial V_g}{\partial x} = -\frac{gh}{\rho B}(\rho - \rho_a) - \frac{\rho_a}{\rho}\left(\frac{\nu_e}{B} + \frac{\omega_e}{h}\right)V_g - \frac{\rho_s W_s B_s V_g}{\rho B h} - \frac{2\tau_y}{\rho h} \quad \textit{(Equation 55)}$$

$$\frac{\partial T}{\partial t} + U\frac{\partial T}{\partial x} = \frac{\rho_a C_{pa}}{\rho C_p}\left(\frac{\nu_e}{B} + \frac{\omega_e}{h}\right)(T_a - T) - \frac{\rho_s C_{ps} W_s B_s (T_s - T)}{\rho C_p B h} - \frac{j}{\rho h C_p} \quad \textit{(Equation 56)}$$

$$\frac{\partial B}{\partial t} + U\frac{\partial B}{\partial x} = V_g + \nu_e \quad \textit{(Equation 57)}$$

where

h is the cloud height,

B is the half-width,

ρ is the layer-averaged density,

ω is the mass fraction,

U is the wind velocity,

T is the cloud temperature,

g is the acceleration due to gravity, W_s is the source velocity,

B_s is the source half-width, C_p is the specific heat,

M is the molecular weight,

ω_e and ν_e are the vertical and horizontal entrainment rates respectively,

τ and j are the momentum and heat fluxes, and

V_g is the crosswind cloud velocity at the side edges.

The subscript "s" refers to the compound to be measure, "a" refers to the ambient air properties and "n" is designated to the vapor properties of the compound to

be measure. The above equations, along with the ideal gas law approximation, are the governing equations of the SLAB model. The six coupled non-linear partial differential equations (PDE) are solved using the finite element collocation method based on piecewise polynomials for spatial discretization techniques and implicit methods for the time integration (Ermak *et al.*, 1982).

CFD Model

The Computation Fluid Dynamic (CFD) is generally used to study the complex scenarios of LNG vapor dispersion. CFD modeling is able to handle the three-dimension dispersion model under complex geometry and obstacles. Several published works that have demonstrated the CFD results give a reasonably good agreement with the experimental results. The CFD code simultaneously solves the governing equations for the transport process using the Reynolds-Averaged Navier Stoke (RANS) (Cormier *et al.*, 2009). The governing equations include the continuity equation, momentum and energy balance.

There are several models to describe the turbulence of the dispersed gas. The most commonly used in the CFD model is the two-equation turbulence model k-ε due to the running time benefit. The two equations of the turbulence kinetic energy, k and turbulence dissipation energy, ε are given as:

$$\frac{\partial(\rho k)}{\partial t} + \nabla \cdot (\rho U k) = \nabla \cdot \left[\left(\mu + \frac{\mu_t}{\sigma_k}\right) \nabla k\right] + P_k - \rho\varepsilon \qquad \textit{(Equation 58)}$$

$$\frac{\partial(\rho \varepsilon)}{\partial t} + \nabla \cdot (\rho U \varepsilon) = \nabla \cdot \left[\left(\mu + \frac{\mu_t}{\sigma_\varepsilon}\right) \nabla \varepsilon\right] + \frac{\varepsilon}{k}(C_{\varepsilon 1} P_k - C_{\varepsilon 2} \rho\varepsilon) \qquad \textit{(Equation 59)}$$

where

$$P_k = \mu_t \nabla U \cdot (\nabla U + \nabla U^T) - \frac{2}{3}\nabla \cdot U(3\mu_t \nabla \cdot U + \rho k) + P_{kb} \qquad \textit{(Equation 60)}$$

and

$$P_{kb} = \frac{\mu_t}{\rho \sigma_\rho} g \cdot \nabla \rho \qquad \textit{(Equation 61)}$$

$C_{\varepsilon 1}$ and $C_{\varepsilon 2}$ are the turbulence model constants,

σ_k is the turbulence model constant for k equation,

σ_ε is the turbulence model constant for ε equation, and

σ_ρ is the Boussinesq buoyancy.

The obtained *k-ε* value is then used in to obtain the turbulence viscosity using the following relationship:

$$\mu_t = C_\mu \rho \frac{k^2}{\varepsilon} \qquad \textit{(Equation 62)}$$

where

C_μ is the turbulence constant,

k is the turbulence kinetic energy, and

ε is the turbulence dissipation rate.

The dispersion of LNG vapor depends on several parameters. Cormier *et al.* (2009) performed a parametric study on the simulation of LNG spills and dispersions. Some of the most influential parameters in LNG dispersions are release rate, pool shape, mass evaporation rate, pool area, turbulence intensity, heat exchange with the surrounding, wind velocity and direction, ambient temperature, surface roughness and effects of barriers or obstacles (Cormier *et al*., 2009).

2.3 Summary of Section 2

In this section, a thorough literature study is presented. The first part of this section introduces the development and application of infrared imaging techniques for gas visualization. Several previous works on the application of infrared cameras for methane gas leak detection as well as LNG vapor cloud visualization are presented.

Following the application of infrared imaging techniques, the method that estimated emissivity as the major determining factor in the use of infrared technology for temperature measurement is illustrated.. Elsasser's band absorption method used to evaluate pure gas emissivity is presented. The data collected by Lee and Happel (1964) on methane absorption at various temperatures and optical lengths is described. Smith's (1982) method for determining the emissivity of a mixture of gray gas is also presented. This method takes into account the effect of the atmospheric content on the total gas emissivity.

A previous study is presented on the quantification efforts used to estimate methane gas emissions from natural gas systems. The statistical study is demonstrated using the Monte Carlo simulation to predict and project methane gas emissions.

Finally, the last part of this section describes atmospheric vapor dispersion modeling, an approach that potentially could be combined with the imaging technique to obtain more quantitative measures of gas emissions from both natural gas and LNG systems. The general Gaussian model is used for measuring the dispersion of buoyant

gas, and the dense gas dispersion model is used for the heavy LNG vapor. Both are presented at the end of this section.

3. METHODOLOGY

3.1 Overview

In this section, there are two different frameworks which were developed for each case based on the objectives of this research work: i) application of the infrared imaging technique for LNG vapor gas visualization and gas temperature measurement, and ii) development of methodology to predict emissions from natural gas leaks in pipeline systems by utilizing the infrared imaging technique combined with the vapor dispersion approach.

There are three general approaches used in this research in order to tackle the gaps and meet the research goal: i) theoretical analysis on radiation heat transfer and gas emissivity ii) experimental work on methane gas leak simulations and LNG spills, and iii) gas dispersion model of methane and LNG. The following sections present the research methodology in more detailed descriptions.

3.2 Application of Infrared Imaging as Non-Contact Temperature Measurement of LNG Vapor Cloud

A methodology that utilizes the infrared imaging technique to measure LNG vapor cloud temperature has been developed in this research. The main reason infrared cameras are not currently used to measure vapors and gas without contact is due to the

unavailable prior information with regard to the emissivity value of the gas. At present, the algorithm in the infrared camera always assumes that the emissivity of the gas is equal to unity, which results in inaccuracy and unreliable thermal reading of the gas. Furthermore, there are no published works that have been able to quantitatively identify the impact of the atmospheric parameters on the temperature measurement shown in the thermal images or thermograms.

This research is utilizing the infrared camera to detect and monitor an LNG vapor cloud and measure the spatial temperature of the cloud. Two types of infrared cameras were used for the visualization of methane gas and LNG vapor clouds, the Amber Radiance 1 thermal camera and the FLIR System Gas FindIR^{TM}. Both infrared cameras worked in a mid wave infrared range within a 3-5 μm window. The Amber Radiance 1 thermal camera was able to provide temperature profiles of the scenes taken during the experiments. The operating temperature of the Amber camera is between 168 K to 338 K with a thermal sensitivity of 10 mK at 300 K. The FLIR System Gas FindIR^{TM} was a dual camera detector system, one detected targets in very narrow infrared wavelengths and one detector acted as a reference. For this reason, this infrared camera could detect most of the hydrocarbons within the narrow wavelength.

The environmental conditions and other parameters which may affect the performance of the infrared camera are recorded and an analytical method to evaluate methane gas emissivity as well as gas mixture emissivity is performed. The emissivity values obtained from the theoretical evaluation are then employed in the Stefan-Boltzmann law of heat radiation in order to obtain the actual spatial temperature

distribution of the vapor cloud. The overall methodology for this LNG system is given in Figure 9.

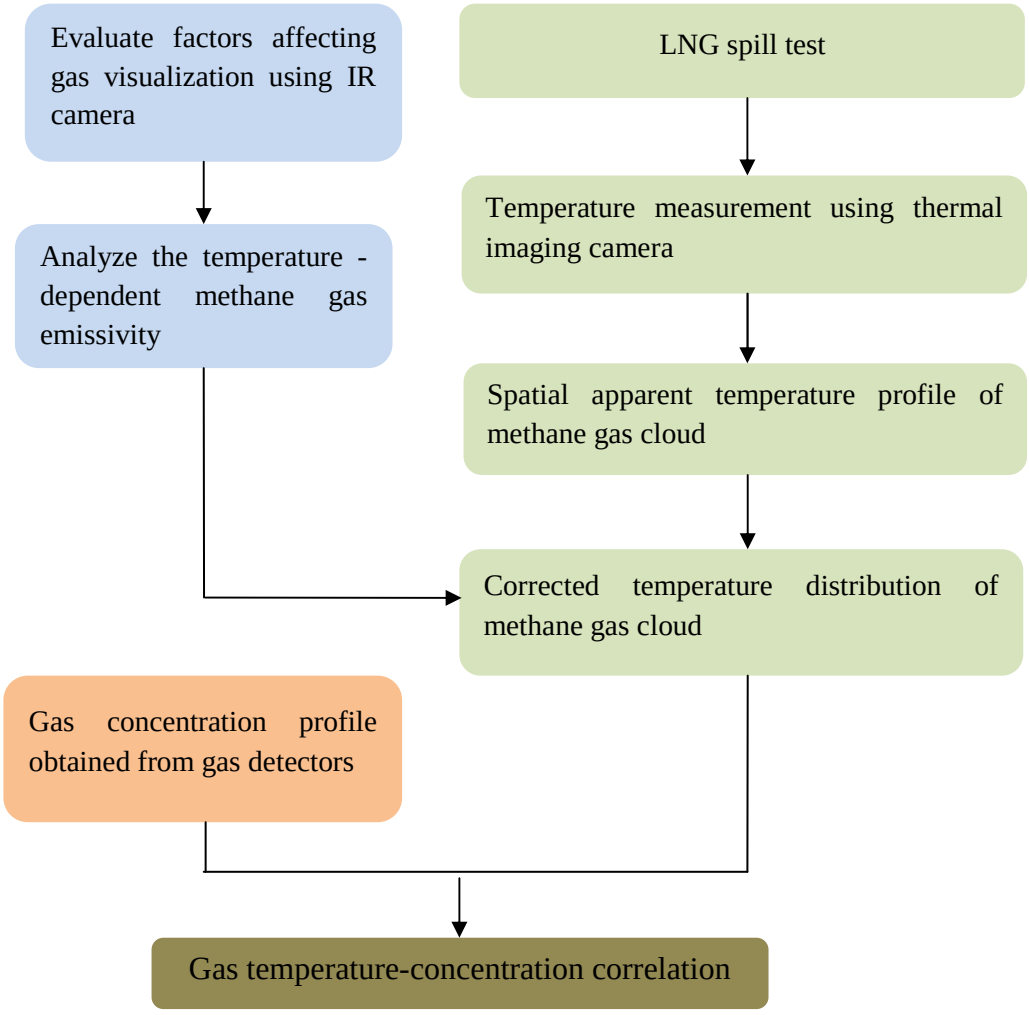

Figure 9. Research Methodology for LNG Systems

The thermal sensitivity for the FLIR GasFindIR is less than 25 mK. The operating temperature range of the camera is 233 K to 623 K. The FLIR system has a built-in video recording, visual camera and laser pointer. Based on the company's

specification, the minimum detected leak rate for methane is 0.8 g/hr using the FLIR Gas FindIR HSX. The output of the infrared camera depends on the object's temperature, reflections, and the medium condition between the camera's detector and target object. Table 7 provides the specifications for the infrared camera used in this work.

Table 7. Specification of the Infrared Imaging Camera

Imaging Performance	
Field of view	22° with 25mm lens
Thermal sensitivity	80 mK @ 30°C
Detector	
Type	Focal Plane Array (FPA), InSb, 320x240 pixels
Spectral range	3 - 5µm
Time constant	16 ms, user selectable
Power Input	
Voltage	6V
Power consumption	<6 W typ.
Environmental	
Operating temperature range	-15°C to +50°C
Storage temperature range	40° to + 70°C
Humidity	20-80% (non condensing) IEC 359
Image Specifications	
Image storage	Hand-held personal video recorder, commercial, off-the-shelf
Image out	NTSC/RS-170, S-video

The infrared camera was used to visualize LNG vaporization and dispersion from an LNG spill on concrete. The experiments were conducted in the LNG emergency response training facility at Brayton Fire School Facility of Texas Engineering Extension

Services, College Station, Texas. The LNG spill test was part of the LNG safety research conducted by Mary Kay O'Connor Process Safety Center.

The layout of the LNG facility and the schematic diagram of detectors for the LNG vapor dispersion tests are shown in Figure 10. The free spreading of LNG tests was conducted in the large pit (Pit 2).

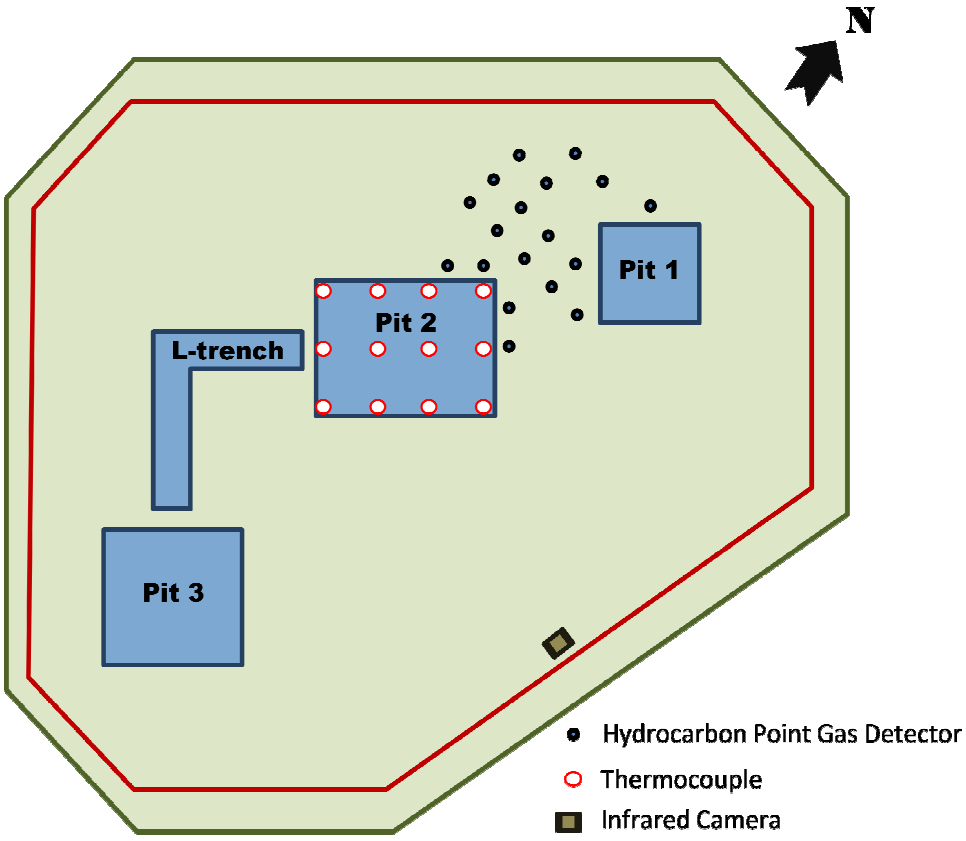

Figure 10. The layout of LNG Facility in BFTF

The LNG emergency response training facility consists of four pits that can contain an LNG spill. The specifications of each pit are given in Table 8.

Table 8. The Specification of LNG Pit in Brayton Fire Training Facility

Pit name	Size
Pit 1	10 ft (L) x 10 ft (W) x 4 ft (D)
Pit 2	33 ft (L) x 21 ft (W) x 4 ft (D)
L-trench	
Pit 3	22 ft (L) x 22 ft (W) x 8 ft (D, 4 ft below and 4ft above the ground)

During the test, gas detectors and thermocouples were being placed to monitor the LNG vapor concentration and temperature. Detailed locations of the gas detectors are given in Figure 11.

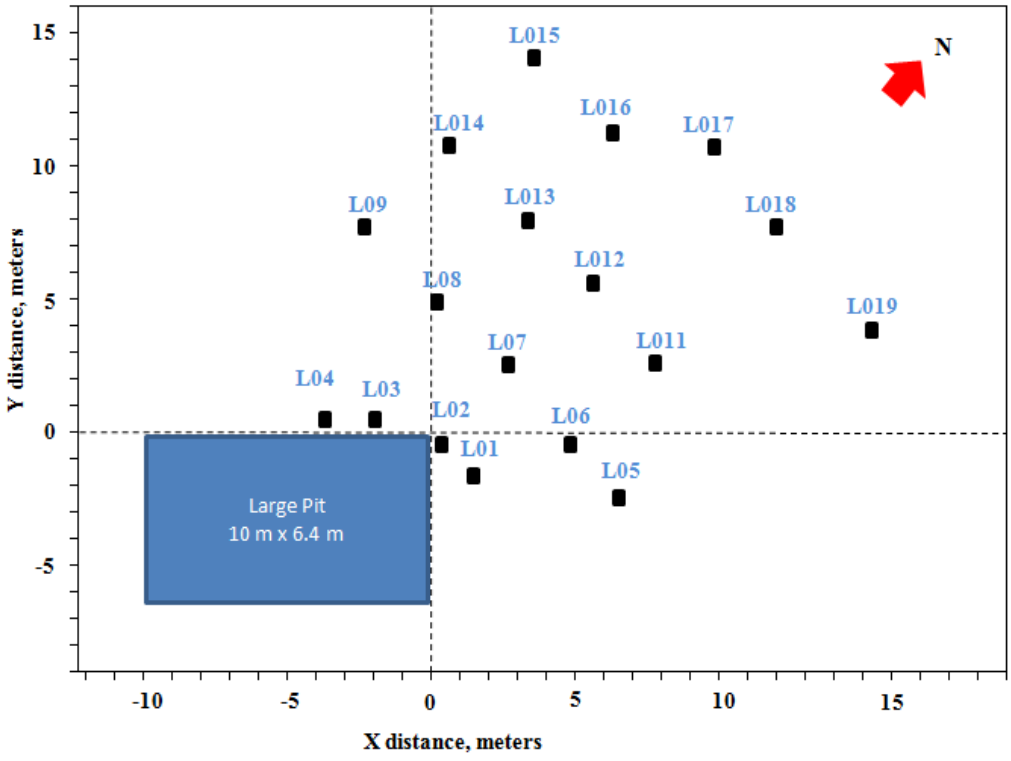

Figure 11. Gas Detector Grid during LNG Test on BFTF

The positions of the gas detectors in the Cartesian coordinate are given in Table 9. These gas detectors are place in the direction of downwind and crosswind.

Table 9. Position of Gas Detector during LNG Spill Tests

Pole #	Gas detector position				Position on grid	
	Low	Bottom	Middle	Top	X, m	Y, m
Location	**0.50**	**1.29**	**2.31**	**3.30**		
L01	-	GD02	GD01	-	1.2	-1.2
L02	-	GD05	GD04	GD03	0.4	-0.4
L03	-	GD08	GD07	GD06	-1.8	0.7
L04	-	GD10	GD09	-	-3.8	0.8
L05	-	GD12	GD11	-	6.6	-1.9
L06	-	GD14	GD 13	-	4.9	-0.2
L07	-	GD21	GD16	GD15	2.3	2.3
L08	GD22	GD18	GD17	-	-0.2	4.9
L09	-	GD 20	GD19	-	-2.8	7.4
L10	-	-	-	-	-	-
L11	-	GD32	GD31	-	8.4	2.9
L12	-	GD26	GD25	-	5.6	5.6
L13	-	GD28	GD27	-	3.9	7.3
L14	-	GD30	GD29	-	1.0	10.3
L15	-	GD24	GD23	-	5.8	13.5
L16	-	GD34	GD33	-	7.3	10.3
L17	-	GD35	GD36	-	10.7	10.7
L18	-	GD38	GD37	-	13.7	7.7
L19	-	GD40	GD39	-	17.1	4.3

The actual temperature distribution obtained by including the emissivity value of the gas mixture is then compared to the concentration profile of the LNG cloud obtained from gas detector measurements in order to obtain the gas temperature-concentration correlation. The developed correlation is useful to predict the LFL and UFL of the LNG vapor to determine the exclusion zone in case of a spill.

3.2.1 Infrared Camera Performance Parameters Evaluation

The factors affecting the infrared camera's performance have been described in the literature. These include the environmental parameters such as ambient temperature, humidity, and atmospheric content as well as optical path length, stimulated emissions, reflectance and operator experience. However, the significance of these parameters for the utilization of infrared optical imaging for gas visualization has not been evaluated. Therefore, in this research these parameters are observed during the tests and further analyzed to determine the significance of these parameters to temperature measurement. The environmental conditions are monitored through a weather station.

Radiation transmitted to the thermal camera depends on the atmospheric attenuation (humidity, incoming solar radiation, air content, e.g., dust particles, and aerosols), and reflectance or emittance from the surrounding objects. In addition, the environment also has a radiating power. When a target reaches thermal equilibrium with the environment, the amount of power radiating from the target is equal to that radiating from the environment. As a result, a target cannot be distinguished from the environment

and one cannot “see” the gas anymore. The atmosphere contains numerous gases and aerosols. These atmospheric constituents have the potential to absorb and scatter the radiation that is transmitted from a target object into the thermal imaging detector. This results in the signature reduction. The atmospheric transmittance depends on the atmospheric constituent, path length, temperature and spectral response of the imaging systems.

Thermal imaging systems cannot differentiate the emitted radiation from the reflected radiation. Hence, the radiation that appears to emanate from the target must also include the emission energy from the surrounding objects.

The effect of the distance between the target object to the camera is also evaluated, and finally, any interference from reflectance of surrounding object is analyzed. The effect of the operator‘s performance is not going to be discussed in this report because the author has been trained to operate the infrared camera prior to conducting the measurements.

The amount of radiation emitted by a target highly depends on the target emissivity. Emissivity is known to be the major cause of uncertainty in using the infrared camera for gas visualization. The emissivity of a target object may vary with temperature, surface quality, environmental conditions, wavelength, and viewing angle. The radiation measured by the camera detector depends on the target and its environment. Since most of time the emissivity of a target gas is not known, the emissivity value is often assigned to be unity. Thus, the apparent temperatures shown in the thermograms are described as the temperature when the emissivity of the target is

assumed to be one and its value does not reflect the actual temperature of the target object.

3.2.2 Emissivity Estimation of a Grey Gas

Emissivity is one important factor in determining the radiative power transmitted to the infrared camera detector. The infrared camera is used as qualitatively analytical tool for gas detection and visualization rather than as a quantitative tool because the temperature gradient depicted in the thermogram does not present the actual temperature of the gas. This happens because the camera detector response always assumes the emissivity of the target as one.

There is no available literature that analyzes the emissivity of LNG vapor. LNG is stored and transported at very low temperatures (111 K), whereas natural gas distribution is usually performed at ambient temperatures. The major composition of natural gas is methane gas; therefore, for the application of infrared imaging for natural gas plume visualization, the emissivity value of methane at a temperature between 110 K and ambient is important to determine the actual temperature distribution of the LNG vapor cloud. Hence, in this research the emissivity of methane gas at temperatures equal to LNG vapors (110 – 300 K) is evaluated and integrated into the Stefan-Boltzmann law in order to obtain the actual temperature distribution of the LNG vapor.

The emissivity of methane was evaluated using the band absorption model developed by Elsasser. The data of methane effective bandwidths from Lee and Happel’s

experiments are extrapolated to lower temperature with the curve fitting method. Band absorptions data for methane is utilized to determine the constants in band absorption equations. Using the band absorption data, the band emissivities and total emissivity can be predicted as a function of temperature and optical length.

3.2.3 Calculation of Gas Mixture Emissivity using Weighted Sum of Grey Gas Model

Although most available literature identifies the atmospheric attenuation as one of the major uncertainties in the application of an infrared imaging technique, there is no mathematical model or quantitative analysis to describe the reduction due to atmospheric contents to the atmospheric transmittance of the application of infrared camera for gas visualization.

The infrared camera detects the radiation transmitted by the target object to the camera detector. The uncertainties in this infrared imaging technique mainly rely on the unknown emissivity value of the target gas. In addition, the effects of atmospheric gases on attenuating the atmospheric transmittance have not been identified. The atmosphere consists of several gases including nitrogen, oxygen, argon, carbon dioxide, water vapor and traces of other gases. The concentration of water vapor in the atmosphere depends on the local relative humidity. Nitrogen, oxygen and argon are considered clear gases, which imply that these gases do not have active absorption within the infrared wave range. Conversely, carbon dioxide and water vapor have active absorption characteristics

in the mid-wave IR range and therefore their presence may result in the attenuation of atmospheric transmission to the infrared camera's detector.

The effect of atmospheric conditions and constituents on the performance and sensitivity of the infrared camera to detect methane vapor is evaluated. Changes in the absorbance and emittance of the target gas in the presence of atmospheric gases are analyzed. The atmospheric attenuation at different ambient temperatures is also assessed.

A model describing the effects of humidity, ambient temperature and optical length is very complex. There is no available published works elucidating these factors into a mathematical expression. The characteristic of atmospheric transmittance as a function of detector-to-target distance has been studied and is available in the literature. However, the effect of atmospheric gases in atmospheric transmissions has not been characterized.

The atmosphere contains many gases; some of the gases have an active absorption within the mid-wave infrared spectrum band, such as $CO_{2,}$ which absorbs radiation at 4.3 μm, and H_2O, which has an active absorption at 6.7 μm. As LNG is released, it is diluted with the atmospheric gases. When the infrared imaging technique is applied to detect LNG vapors, the camera's detector captures the radiation emitted by the methane gas and some other constituents in the atmosphere. The amount of the radiation emission is determined by the emissivity of the gas mixture. As the concentration of water vapor increases due to the increase in humidity, its influence on the total gas emissivity will be amplified.

Absorption and polynomial coefficients are determined using the curve fitting procedure that fits the model expressions to experimental spectral data. The model expressions are nonlinear; there is more data than the coefficients available. Therefore, a curve fitting procedure based on the minimization of error between the model and data can be used to obtain the coefficients. Any bias would be minimized by utilizing a form of regression analysis. The value of the absorption and correlation coefficients of a CO_2 and H_2O mixture as a result of combustion of gaseous fuel has been evaluated (Smith *et al.*, 1982). Most of real gases are characterized by three gray gases and four third-order gas temperature polynomial coefficients. Using numerical analysis and regression technique approach, the coefficients for the WSGGM were evaluated in order to estimate the total emissivity of carbon dioxide, water vapor, and mixtures of these gases. The model yielded a reasonable prediction of the property values compared to the data.

3.3 Estimation of Methane Emission Rates from Fugitive Leaks from Natural Gas Pipelines System

The semi-quantitative method used to determine emission factors for different components was a suitable approach to estimate the total mass emission rate of fugitive gas released from leaking components. However, this method evaluated the emission factor of a component by comparing the leak rate to the lowest threshold, or sensitivity level, at which the camera detector responded. The emission factor was calculated by summing the total emissions divided by the total count of the components. Furthermore,

this semi-quantitative measure was general for all hydrocarbons which an infrared camera could detect. This method was not able to identify the correlation between the sizes of detected gas plumes and the emissions rate for a specific gas. Different gases have different characteristic when released to the atmosphere. Some gases that are denser than air will have a tendency to stay on the ground before eventually warming up and lifting upwards, whereas, some gases are lighter than air and rise when released into the atmosphere. Accurate quantitative measures for specific gases are important; therefore, this paper proposes a solution for estimating the gas mass flow rate of methane emissions based on a dispersion modeling approach. The methodology for estimating methane gas emissions rates from natural gas distributions and pipeline systems is given in Figure 12.

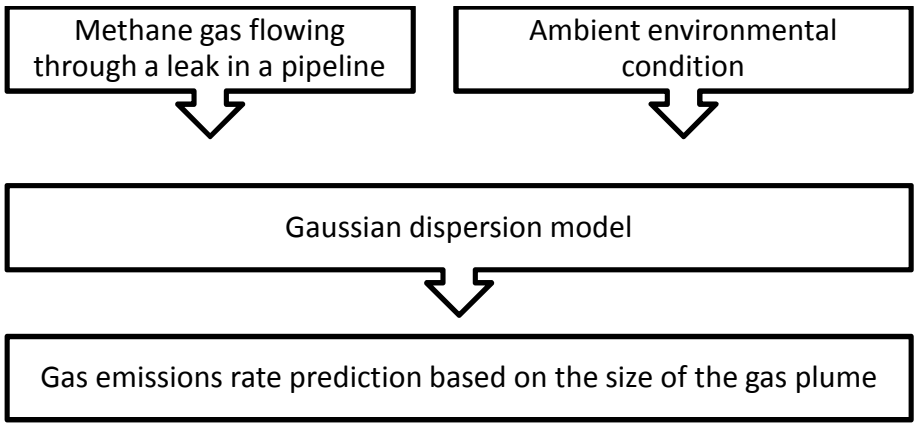

Figure 12. Methodology to Estimate Methane Gas Emissions Rate using Dispersion Simulation of Methane Gas Leak from Natural Gas Pipeline System

In the event that a leak occurs in a natural gas pipeline, a certain amount of gas will be released, mixed and diluted with air. The leakage rate from the emission source depends on the differential pressure between the upstream pressure and ambient pressure, the size of the leak, and the temperature of the gas inside the pipeline. The concentration of the gas as it is dispersed can be estimated using Gaussian dispersion modeling. Sensitivity analysis of the gas concentration at different meteorological conditions is simulated. Using a Gaussian dispersion model, the correlations between leakage rates and plume size, i.e. distance and plume height to minimum detectable downwind concentration for methane gas, can be predicted.

A dispersed gas can be recognized by the infrared camera to a certain threshold concentration. The concentration of the dispersed gas at a downwind distance from the release depends on the meteorological conditions including wind speed, wind direction and ambient temperature. Since the atmospheric conditions are constantly changing, it is impossible to assign a single value to those parameters and therefore the atmospheric parameters are generally presented in a time-average value. By examining the wind speed and the solar radiation conditions during measurement, the Pasquill-Gifford stability class can be assigned to the site where the scanning will be performed. The wind speed, direction and ambient temperature on site can be observed and recorded using weather station on real-time.

The dispersion of methane gas was calculated using the consequence modeling tool PHAST 6.53.1 and the unified dispersion model. The model solves the continuity equation, momentum balance and energy balance as described in Section 2.

The discharge of methane gas from a leak in a pipeline can be modeled using PHAST software as well. The results of the model are compared to the calculation using equations described in section 2. After the discharge term is established, the dispersion of methane is simulated at various stability class and wind speed. The correlation of the gas discharge rate to the distance of gas cloud to the minimum detectable concentration is then withdrawn.

3.4 Summary of Section 3

This section describes the methodology for conducting the research. The methodology for the application of infrared cameras for both cryogenic LNG vapors and methane gas at ambient temperatures is demonstrated. For the application of infrared cameras in the LNG system, a methodology was developed in order to obtain the actual temperature distribution of the LNG vapor cloud. For that purpose, data on gas emissivity values as well as the quantification of the atmospheric impact on temperature measurement are important. Therefore, the evaluation of methane gas emissivity and the analysis of atmospheric content and conditions are included in the overall research framework. The temperature distribution is compared to the concentration measurement using gas detectors in order to obtain a correlation between the temperature and concentration of the dispersed LNG vapor.

Secondly, the infrared camera is also used to detect fugitive methane gas leaks in natural gas pipelines. In this system, methane is discharged at an ambient temperature.

Hence, the aim for the infrared camera application is not to measure the temperature distribution of the gas but rather to measure the size of the gas plume, to be used to predict the gas emission rate. Dispersion modeling using the consequence modeling tool PHAST 6.53.1 based on the Unified Dispersion Model (UMD) is utilized to determine the correlation between the gas emission rate and the minimum gas concentration detected by the infrared imaging.

4. RESULTS AND DISCUSSIONS PART I: APPLICATION OF INFRARED IMAGING FOR LNG VAPOR CLOUD VISUALIZATION

In this section, the application of infrared imaging for LNG visualization is presented. The thermogram of the LNG vapor is evaluated to determine factors that may affect the temperature measurement. The emissivity of methane gas and the emissivity of the mixture of methane and atmospheric gases in the temperature range of LNG vapor during the test are also evaluated. The emissivity function obtained from the calculation is integrated into the radiation heat transfer law to obtain the actual spatial temperature distribution of the LNG vapor. The concentration profile of the gas cloud from the gas detector measurement is evaluated and compared to the spatial temperature profile of the LNG gas in order to obtain the temperature-concentration profile of the LNG gas cloud.

4.1 Analysis of the Thermogram of LNG Vapor Cloud

Mary Kay O'Connor Process Safety Center at Texas A&M University together with Brayton Fire Training Facility Texas Engineering Experiment Station conducted medium scale tests of LNG spills on water in November 2007, March 2008 and March 2009. During all experiments, two types of infrared cameras were used, Amber Radiance

1 Thermal Camera and FLIR System Gas FindIR^{TM}, to visualize the LNG vapor dispersion in the atmosphere. All infrared cameras work in the mid wave infrared range.

The average ambient temperature during an LNG spill test conducted in November 2007 was 287.3 K. LNG vaporizes at 111 K, and therefore a temperature range of 111 K to the ambient temperature of the LNG vapor cloud is expected. The Amber Radiance 1 Thermal Camera depicted that the highest temperature of the scene was 287.6 K and the lowest temperature was 283.5 K. The temperature shown in the thermal image (thermogram) had a significant discrepancy with the actual LNG temperature. The temperature values shown in the thermal camera did not present the actual temperature of the gas because the camera detector assumed the emissivity of the gas was equal to the unity during measurement. In addition, many other factors may influence the temperature measurement of the plume, including the water content of the atmosphere, atmospheric attenuation and the reflection from surrounding objects.

The thermogram of the LNG vapor cloud during the LNG test performed in November 2007 is shown in Figure 13. During the November 2007 test, the lowest wind speed was measured at 2.2 m/s in a South East direction and the highest was 6.3 m/s in a South direction. The average humidity measured during LNG vapor dispersion was 36.7 %. The figure shows that the LNG plume shape keep changing over time due to the effects of the weather condition and change in wind direction.

Figure 13. Infrared Images of LNG Spill on Water during November 2007 test at Brayton Fire Training Facility

During the LNG spill test that was conducted in March 2008, the ambient temperature was measured at 288.7 K. The infrared images of the LNG vapor dispersion during the March 2008 test are shown in Figure 14. The Amber Radiance 1 Thermal Camera depicted that the highest temperature of the scene was 288.9 K and the lowest temperature was 285.7 K. The lowest wind speed was 0.9 m/s and the highest was 2.7 m/s in an East direction. The average humidity measured during the LNG vapor dispersion was 38.2 %.

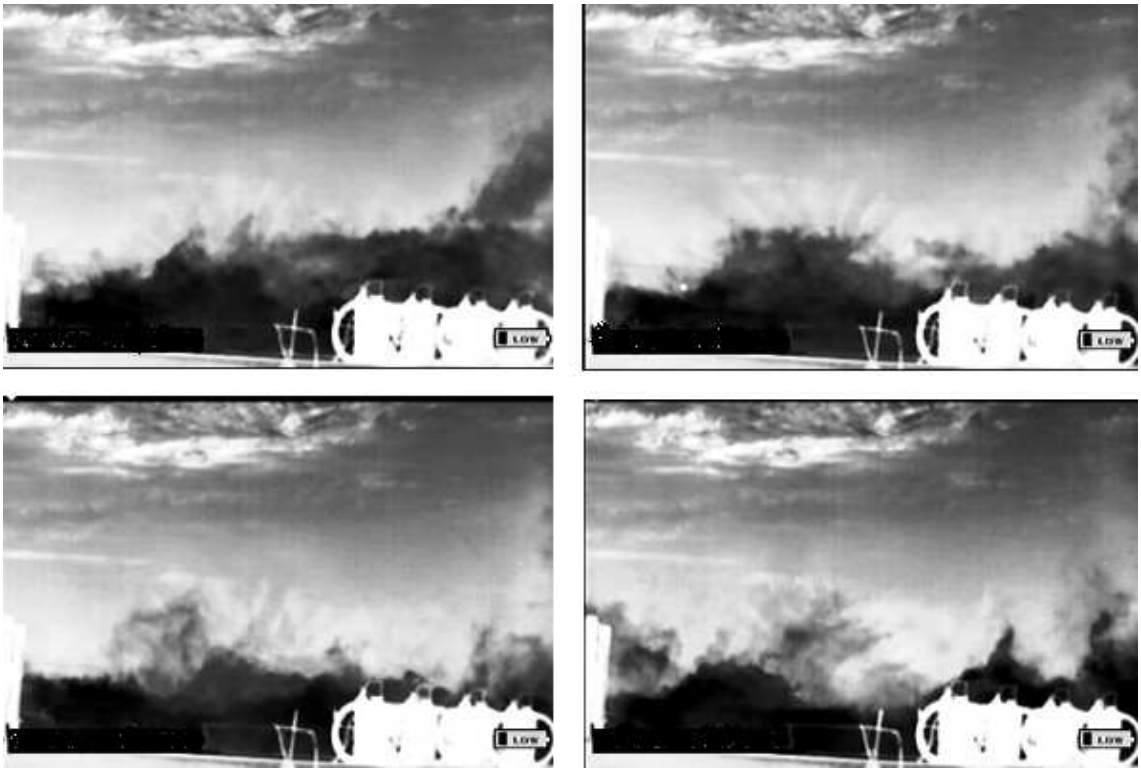

Figure 14. Infrared Images of LNG Spill on Water during March 2008 Test at Brayton Fire Training Facility

In the thermal images, or thermograms, temperature was presented as the grey shade against a uniform background. Depending on the polarity of the camera, lighter shades can represent both higher and lower temperatures. However, during the tests conducted at the Brayton Fire Training Facility the polarity of the infrared camera was set as to provide lighter shades for higher temperatures and darker shades for lower temperatures. The shade or color gradation was determined from the radiation intensity that was absorbed and emitted by the target.

From the thermograms shown in Figure 13 and Figure 14, it was indicated that background or ambient conditions determine the infrared image quality. The ambient

conditions affected the color contrast and sharpness of the image. At higher ambient temperatures there was better contrast between the LNG plume and the environment, e.g. the March 2008 test. The wind effect, which determined the turbulence of the gas plume, can be observed from the figures. The wind velocity during the experiments is higher in the November 2007 test compared to that of the March 2008 test. It can be observed that the gas dispersion was steadier for lower wind speeds.

The radiation emitted to and from an object fluctuated due to the presence of atmospheric transmittance. The atmosphere is composed of numerous gases and aerosols that absorb and scatter radiation as they travel from the target to the thermal imaging system. Water vapor and carbon dioxide are major absorbers in the infrared region. The water vapor concentration increases as the relative humidity increases. However, transmittance was not linearly related to absolute humidity. As the water vapor increased, the atmospheric transmittance decreased. This reduction in radiation is called the atmospheric transmittance. The radiation accumulated along the line of sight due to the scattering of ambient light into the line-of-sight caused a reduction in the target contrast. The radiation that reached the imaging system was the sum of the attenuated target radiation. The magnitude of the transmittance depended on the atmospheric constituents, path length, and spectral response of the thermal imaging system. However, the atmosphere was constantly changing over time, as indicated in the thermograms. Thus, it is rather impossible to assign a single number to the transmittance.

In addition to the atmospheric gases, other constituents in the atmosphere could also affect the radiation absorbed and emitted by the target object. Aerosols changed the

amount of radiation primarily by scattering the radiation out of the line of sight. High humidity might cause particles to grow and may result in the scattering of radiation, and eventually decreases in transmittance to the camera detector.

The water vapor in the atmosphere absorbed and scattered the radiation, which results in reduction of the target signature. The higher the water vapor content, the more magnified the effects of reduction on the target signature became. In addition, water that accumulated along the line from the target gas to the camera detector radiated energy at ambient temperatures and resulted in a reduction of the target contrast. The effects of water vapor on reducing the radiation energy are analyzed further in the third section of this section.

Another parameter that could alter the measurements was the reflectance from the surrounding objects, for example the reflectance from the metal structures and water tanks in the vicinity of the experiment location, which had the potential to attenuate the radiation traveling from the target to the camera. This is discussed briefly in the uncertainly analysis; however, quantifying the effects of reflectance on the infrared thermogram is not with the scope of this research.

4.2 Methane Gas Emissivity as a Function of Temperature

The most important factor in measuring the temperature using the infrared imaging system is the emissivity of the gas. Because thermal cameras always assume the emissivity of an object is equal to unity, the apparent temperatures depicted in the

thermograms did not reflect the true temperature of the gas. If the emissivity of the gas is unknown, the temperature measured using the thermal imaging system would not have any significance, and the values would be meaningless. This section provides an evaluation of methane gas emissivity at low temperatures using the band absorption model.

Most objects do not emit all the radiation; they only emit a fraction of it. The ratio of the actual radiation from an object compared to that of an ideal black body is known as emissivity. The emissivity varies with wavelength, the object's shape, temperature, surface quality and viewing angle (Holst, 2000). Thermal imaging systems measure an object's temperature by assuming that the emissivity is equal to unity. When the emissivity is not known, it is misleading to assume the apparent temperature is the true temperature of the object. The discrepancy between the apparent and true temperatures becomes larger for lower emissivity. Therefore, the emissivity is the main uncertainty in temperature measurement using the imaging system.

This research aims to estimate the emissivity of methane for a temperature range between the boiling temperature of LNG (111 K) and the ambient temperature (298 K). There is no available literature in the past which evaluates the methane emissivity within this temperature range. Thus, in this research work, the emissivity of methane at 111 – 298 K was calculated using the band absorption method developed by Elsasser and the data of methane effective band width and absorption band collected by Lee and Happel (Ostrander, 1951; Lee & Happel, 1964).

Using this information, methane gas emissivity was estimated by fitting the data from Lee and Happel into the Elsasser correlation to obtain the constants in Equations 15 – 18. With the known constants, the data was then extrapolated to calculate the band emissivities and total emissivity of methane at low temperatures.

The data for the effective band width of methane gas at 3.31 and 7.65 μ band from Lee and Happel are shown in Table 10. Since the absorption at 2.37 μ was considered weak absorption, the band absorption in this wavelength did not depend on the effective band width. The absorption band of methane at gas 2.37 μ only depends on the gas temperature and the optical length.

Table 10. Effective Bandwidths of Methane Gas at 3.31 and 7.65 μ (Lee & Happel, 1964)

		3.31μ Band			**7.65 μ Band**		
T (K)	Jmax	ω_{v3}(R)	ω_{v2+v4}(P)	$\Delta\omega$ (cm^{-1})	ωv4(R)	ωv4(P)	$\Delta\omega$ (cm^{-1})
295	20	3207	2706	501	1396	1190	206
373	23	3231	2688	543	1404	1172	232
473	25	3246	2676	570	1408	1160	248
573	28	3268	2658	610	1413	1142	271
673	30	3282	2646	636	1413	1130	283
773	32	3296	2634	662	1419	1118	301
873	34	3309	2622	687	1422	1106	316
973	36	3322	2610	712	1422	1094	328
1073	38	3335	2598	737	1422	1081	341
1173	40	3347	2585	762	1422	1069	353
1273	42	3357	2573	784	1422	1057	365
1473	45	3377	2555	822	1422	1038	384
1673	48	3393	2536	857	1422	1020	402
1873	50	3404	2524	880	1422	1007	415
2073	53	3419	2505	914	1422	988	434
2273	56	3433	2486	947	1422	970	452

By plotting the effective band width data for methane given in Table 10, the relationship of effective band widths and temperature for 3.31 μ and 7.56 μ bands can be obtained and used to calculate the effective band width at lower temperatures. The plot of the effective band widths as function of temperature for 3.31 μ is given in Figure 15.

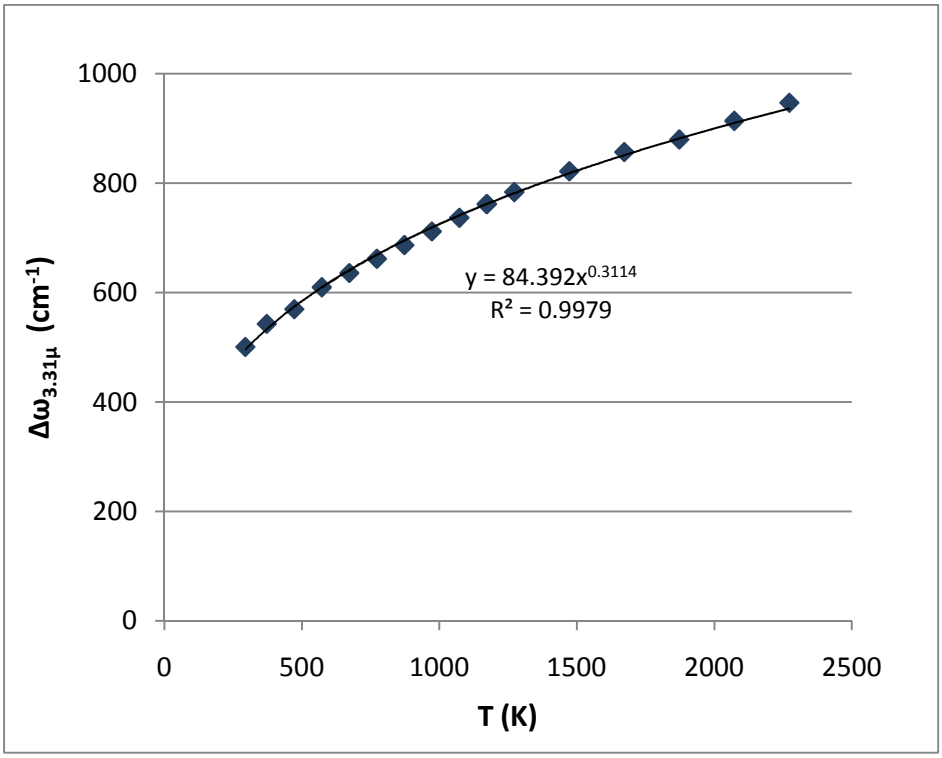

Figure 15. The Effective Bandwidth of Methane at Different Temperatures for 3.31 μ Band

From Figure 15, one can obtain the relationship between temperature and effective band width for methane at 3.31 μ as following:

$$\frac{\Delta\omega_{3.31\mu}}{(\Delta\omega_{3.31\mu})_0} = \left(\frac{T_g}{T_{g0}}\right)^{0.311} \qquad \textit{(Equation 63)}$$

The plot of the effective band widths as function of temperature for 7.65 μ is given in Figure 16.

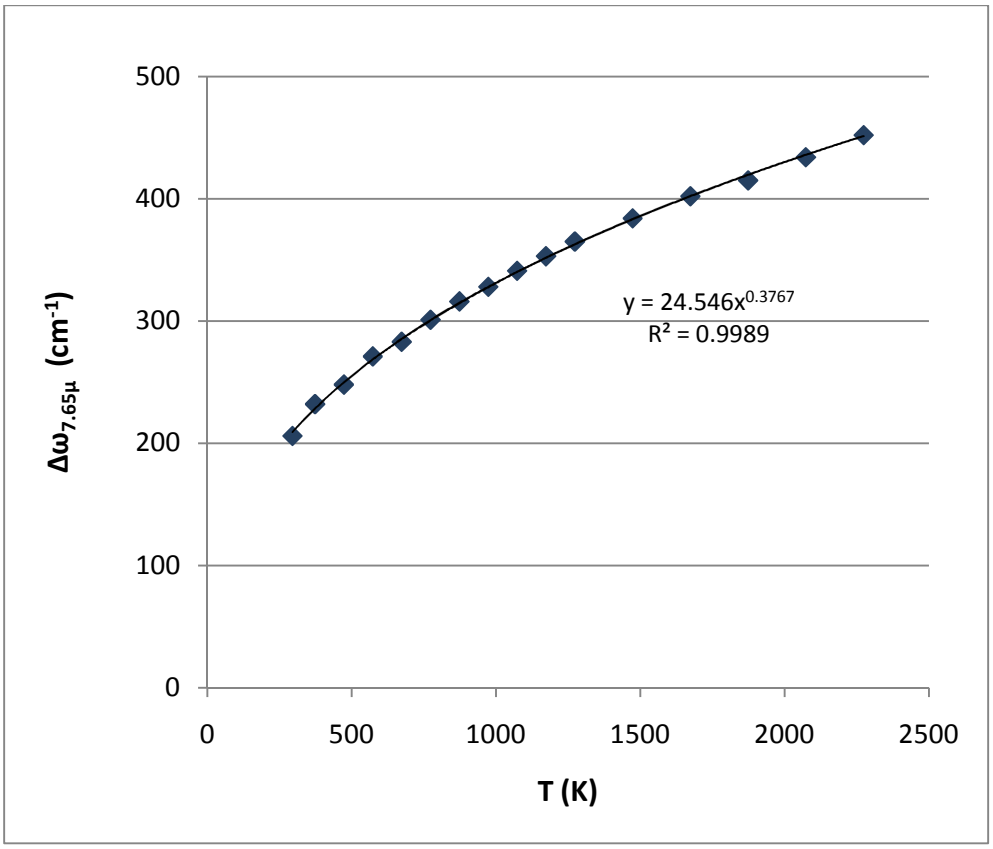

Figure 16. The Effective Bandwidth of Methane at Different Temperatures for 7.65 μ Band

From the figure, the relationship between the effective bandwidth to gas temperature for methane at 7.65 μ can be determined. The relation is given as:

$$\frac{\Delta\omega_{7.56\mu}}{(\Delta\omega_{7.56\mu})_0} = \left(\frac{T_g}{T_{g0}}\right)^{0.377} \qquad \textit{(Equation 64)}$$

The data of methane absorption at three different wavelengths (2.37, 3.31 and 7.65 μ) as a function of temperature obtained by Lee and Happel in 1964 is presented in Table 11. These data is used further to determine the relationship of gas band absorption to temperature at a specific optical depth.

Table 11. Band Absorption of Methane at 7.72 cm-atm Optical Depth and Different Temperatures (Lee & Happel, 1964)

T (K)	$A_{2.37\,\mu}$ (cm^{-1})	$A_{3.31\mu}$ (cm^{-1})	$A_{7.65\mu}$ (cm^{-1})
295	106.3	193.2	124
375	102.3	189.5	126
378		187.9	
471	85.7	181.3	131.8
473	88.2	184.1	129.9
569	71.8	192.3	139.5
668	60.7	214	146
674	53	221	149.9
768	66.6	234.2	152.3
873	58.7	238.7	152.9
873	56.8	242.3	151.7
974	63.2	265	
1008	51.6		161.7
1079	61.9	254.8	
1084			164.7
1118	51	279.2	
1138	52.8	273.7	

The absorption band for methane gas at 2.37 μ wavelength is plotted against temperature to find the constants D_{i0} and $(\xi_i + \zeta_i)$ in Equation 17 as given in Figure 17.

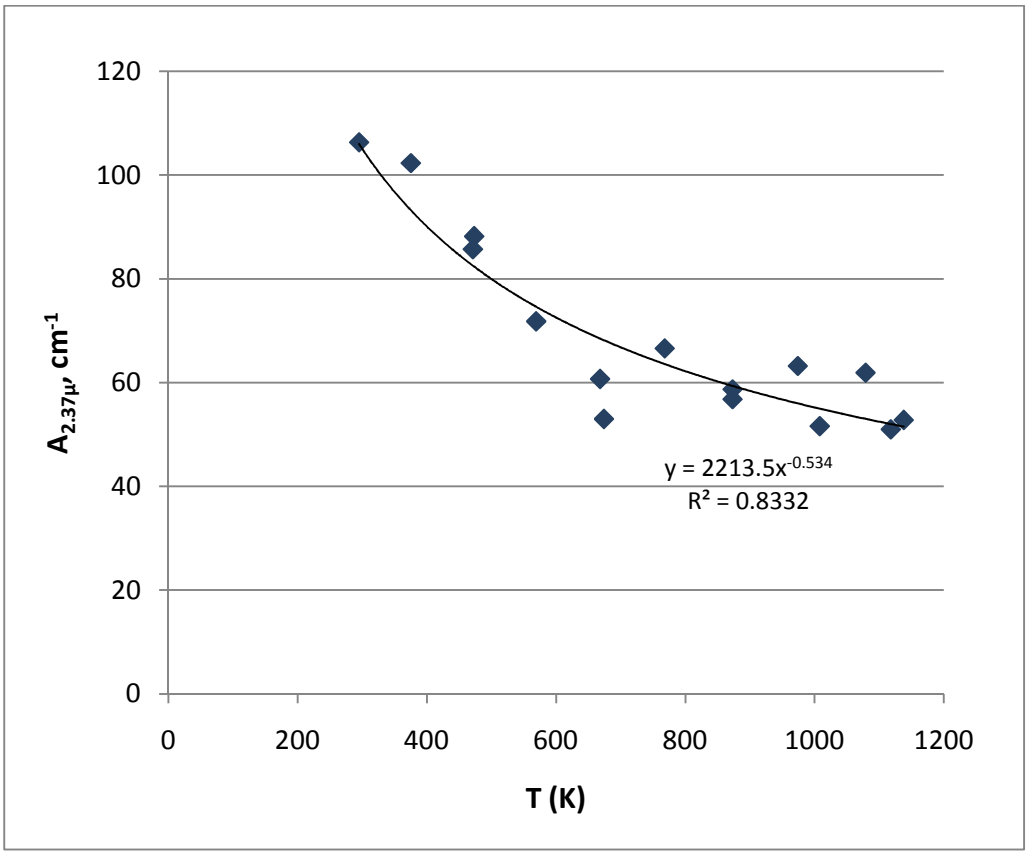

Figure 17. Band Absorption as a Function of Temperature for Methane Gas at 2.37 μ Wavelength and 7.72 cm-atm Optical Length

The relationship between temperature and absorption band for methane at 2.37 μ is obtained from the plot as given in the following equation:

$$\frac{A_{2.37\mu}}{(A_{2.37\mu})_0} = \left(\frac{T_g}{T_{g0}}\right)^{-0.534} \qquad \textit{(Equation 65)}$$

The value of the constant $(\xi_i + \zeta_i)$ obtained from the plot is -0.534 and by taking T_{g0} = 295 K the constant D_{i0} is equal to 38.2 with standard deviation equal to 3.7. Thus for 2.37 μ band, equation 17 can be rewritten as following:

$$A_{i,2.37\mu} = 38.2\left(\frac{T_g}{295}\right)^{-0.534}\sqrt{X} \qquad \textit{(Equation 66)}$$

Band emissivity was determined from Equation 9. The band emissivity at a certain temperature and optical depth is the product of the absorption band width and the Planck radiation function divided by the total energy emitted by a perfect black body at that temperature determined by the Stefan-Boltzmann law.

By using equation 66 in the emissivity calculation, the band emissivity of methane at 2.37 μ as a function of temperature can be obtained. The band emissivities of methane gas at temperature 110 – 350 K are given at 2.37 μ is shown Figure 18.

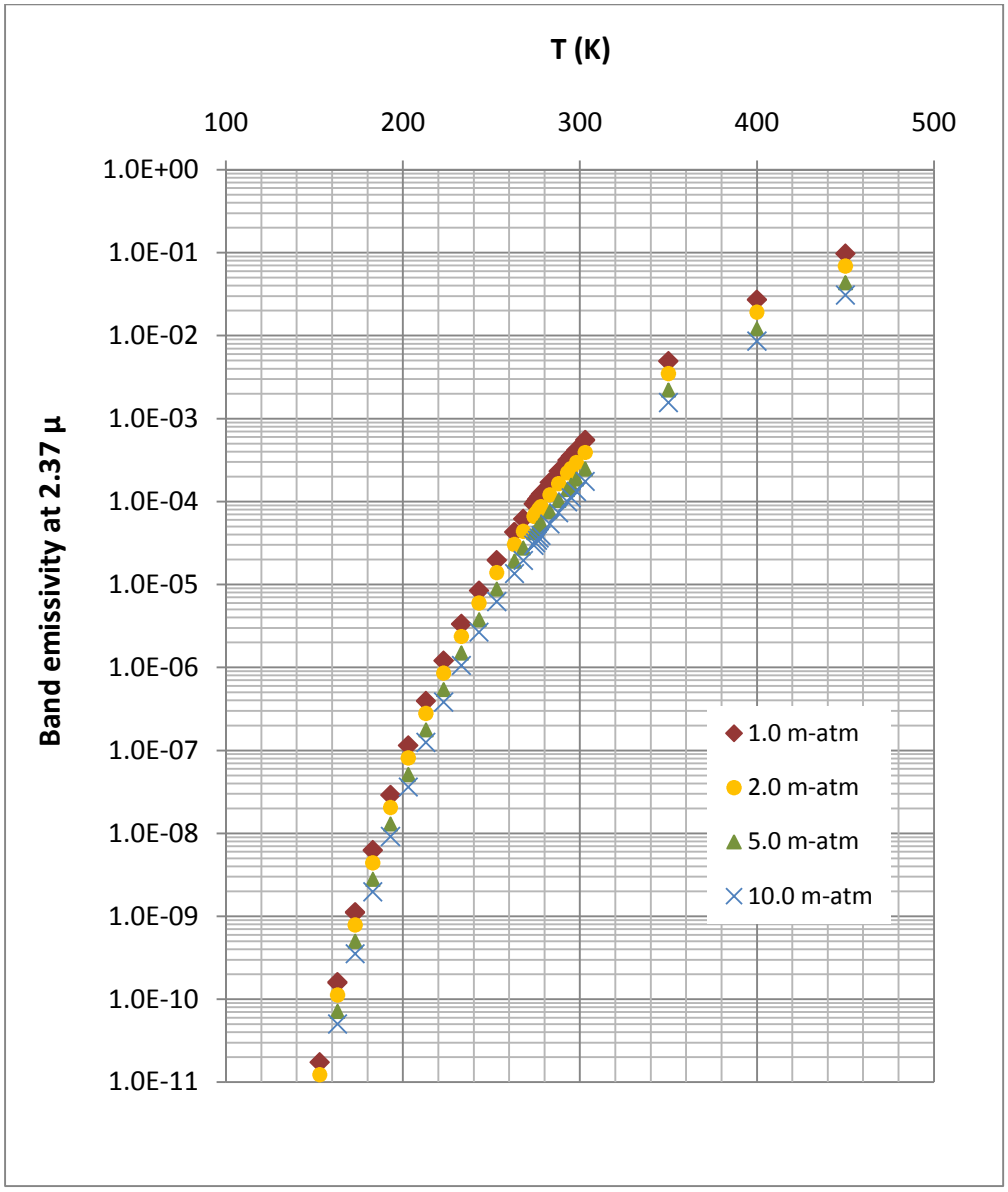

Figure 18. Band Emissivity of Methane Gas at 2.37 µ at Various Temperatures and Optical Path Lengths

The 3.31 μ and 7.65 μ wavelength are categorized as strong absorption bands and the magnitude of the absorption band is function of their effective band widths for methane gas. The absorption band for methane gas at 3.31 μ wavelength and 7.72 cm-atm is plotted against temperature and shown in Figure 19.

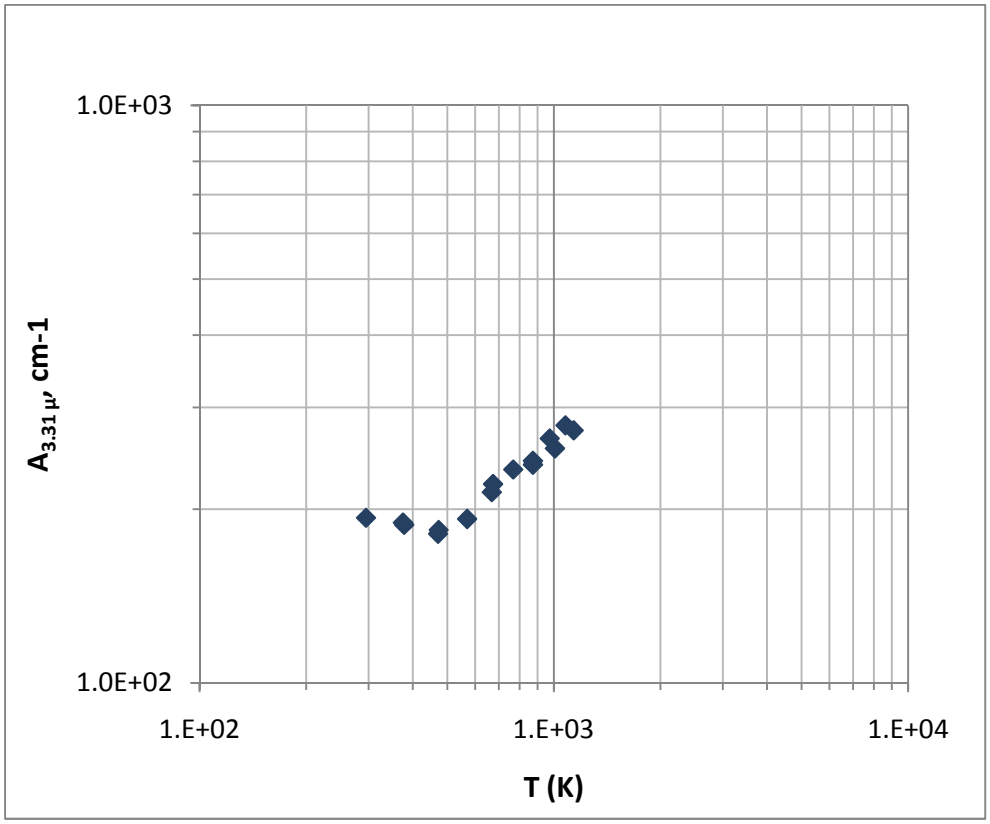

Figure 19. Band Absorption of Methane Gas as a Function of Temperature for Methane Gas at 3.31μ and 7.72 cm-atm

Equation 15 was used to fit the data of the absorption band as function of temperature for the strong, or overlapping, band (3.31 and 7.65 μ). For 3.31 μ band, the plot of the absorption band against the temperature demonstrated two different regions.

The two regions can be observed in Figure 20: a) at T < 473 K, the absorption band decreases as the temperature increases and b) at T ≥ 473 K, the absorption band increases with temperature.

For methane at 3.31 μ wavelength, Figure 20(a) shows the plot of $erf^{-1}(A_i/\Delta\omega_i)$ against the temperature at temperature < 473 K and Figure 20(b) is the plot for methane at temperature ≥ 473 K. The constant, ξ_i, obtained from these plots are -0.477 for T < 473 by setting T_{g0} = 295 K and for $T \geq 473$ K, the constant, ξ_i = 0.185 by setting T_{g0} = 473 K.

The value of constant C_{i0} for T < 473 K is equal to 0.129 with standard deviation = 0.001. Thus for 3.31 μ band at T < 273, equation 4.15 can be rewritten as follows:

$$A_{i,3.31\,\mu} = \Delta\omega_i(T_g) erf\left\{0.129\left(\frac{T_g}{T_{g0}}\right)^{-0.477}\sqrt{X}\right\} \qquad \textit{(Equation 67)}$$

The value of constant C_{i0} for $T \geq 473$ K is equal to 0.103 with standard deviation = 0.003. Thus for 3.31 μ band at $T \geq 273$, Equation 15 can be rewritten as following:

$$A_{i,3.31\,\mu} = \Delta\omega_i(T_g) erf\left\{0.103\left(\frac{T_g}{T_{g0}}\right)^{0.185}\sqrt{X}\right\} \qquad \textit{(Equation 68)}$$

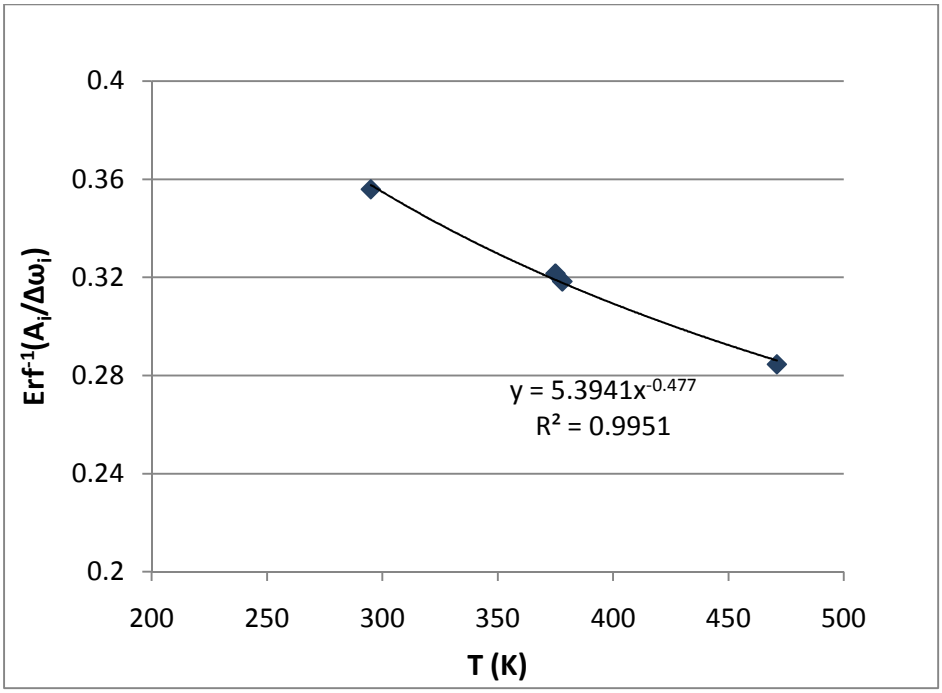

(a)

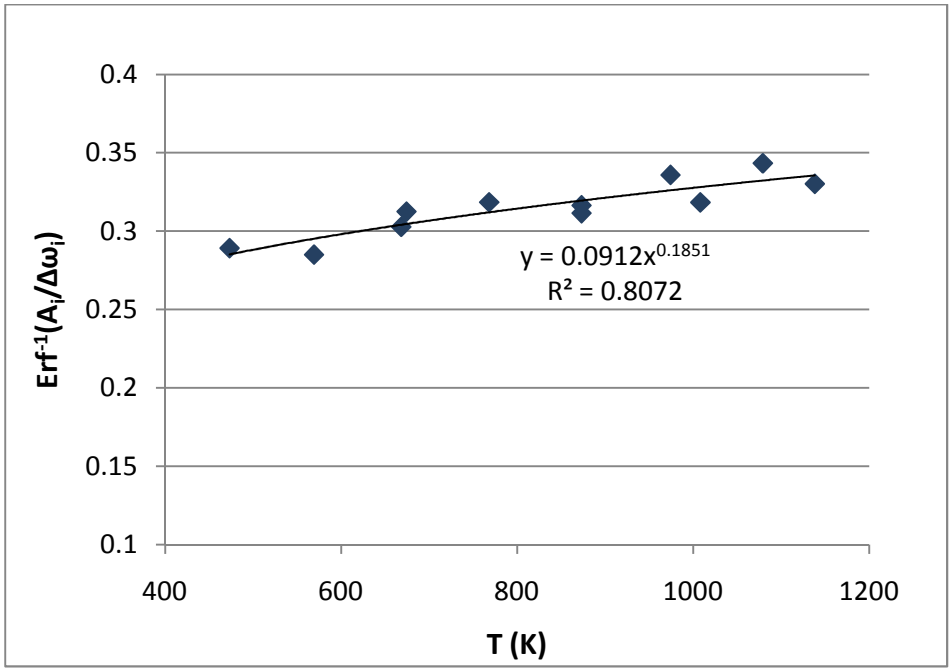

(b)

Figure 20. Plot of $Erf^{-1}(A_i/\Delta\omega_i)$ for Methane Gas at 3.31 μ, 7.72 cm-atm and at: a) T < 473, and b) T ≥ 473 K

By applying Equation 9, the band emissivity of methane gas at 3.31 μ was obtained. Figure 21 shows the band emissivity at 3.31 μ at various temperature and optical path length. The emissivity of methane gas at 3.31 μ is higher than the emissivity at 2.37 μ because methane has a stronger absorption in this bandwidth.

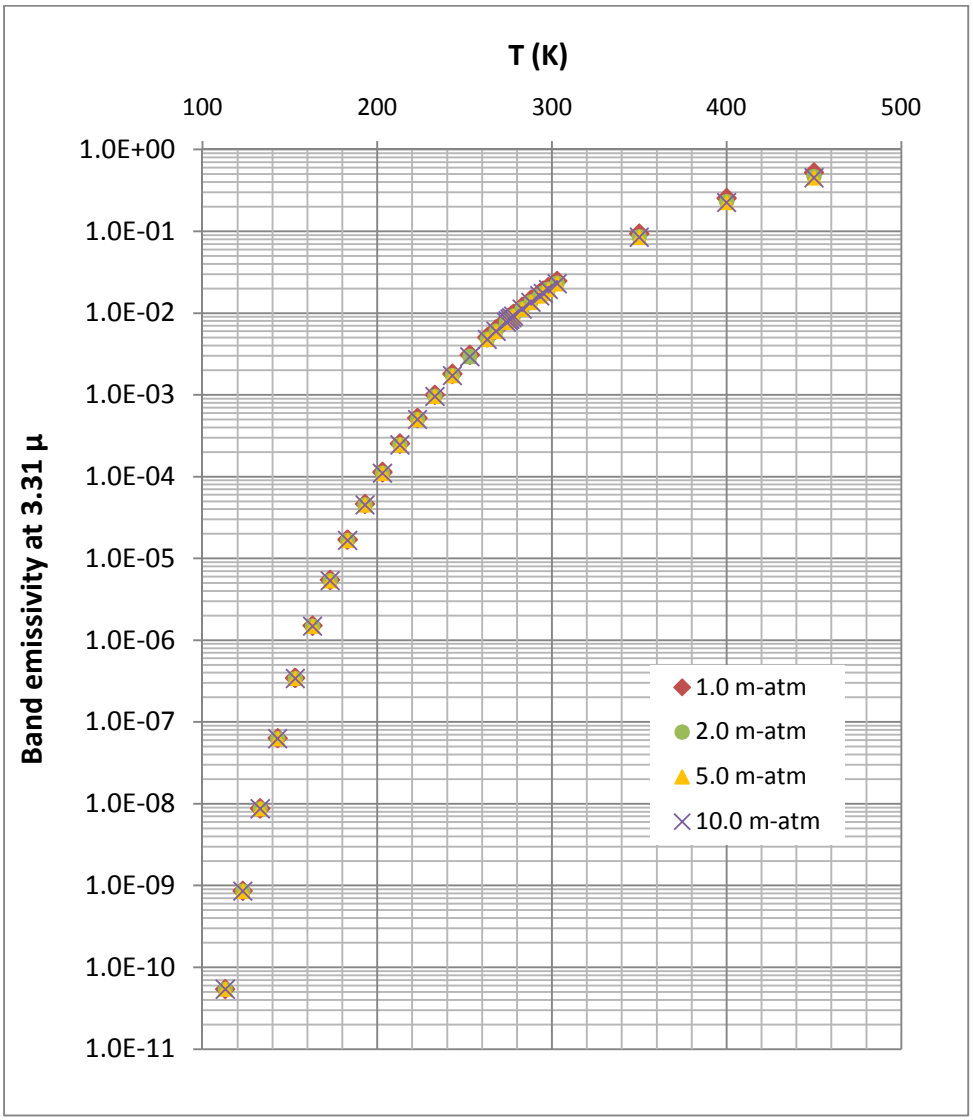

Figure 21. Band Emissivity of Methane Gas at 3.31 μ at Various Temperatures and Optical Path Lengths

For 7.65 μ band, the plot of the absorption band against the temperature is shown in Figure 22.

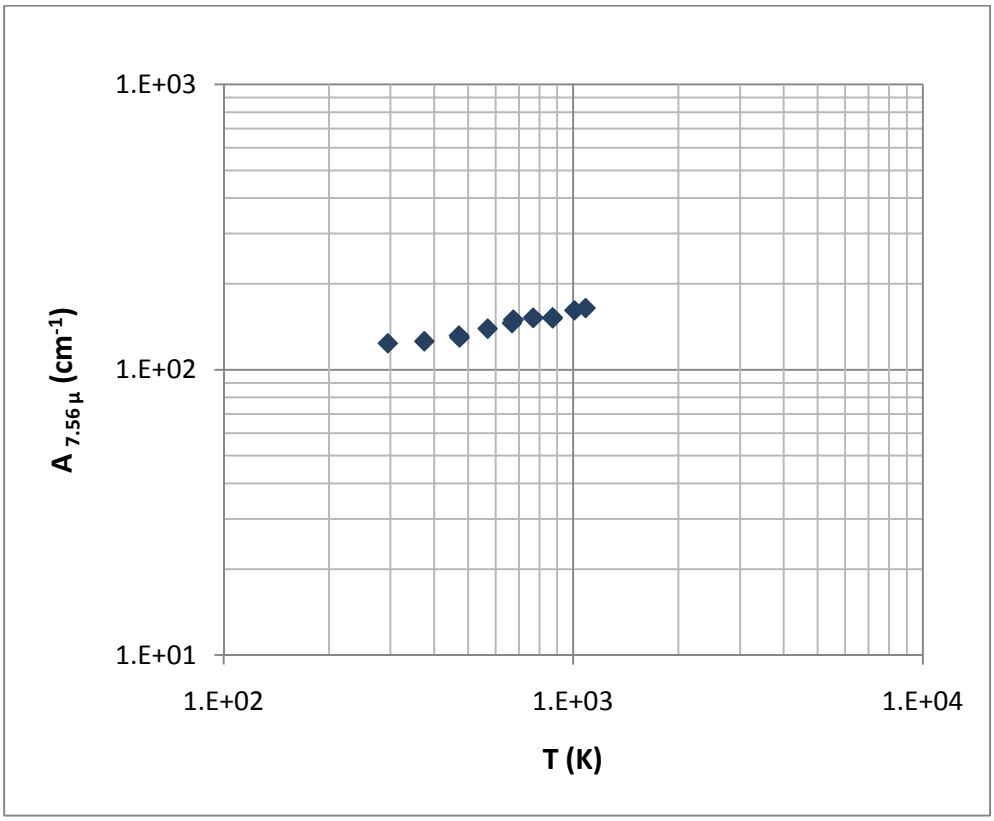

Figure 22. Absorption Band of Methane Gas at 7.56 μ and 7.72 cm-atm

Figure 23 gives the relationship between $erf^{-1}(A_i/\Delta\omega_i)$ and the temperature for methane gas at 7.56 μ band.

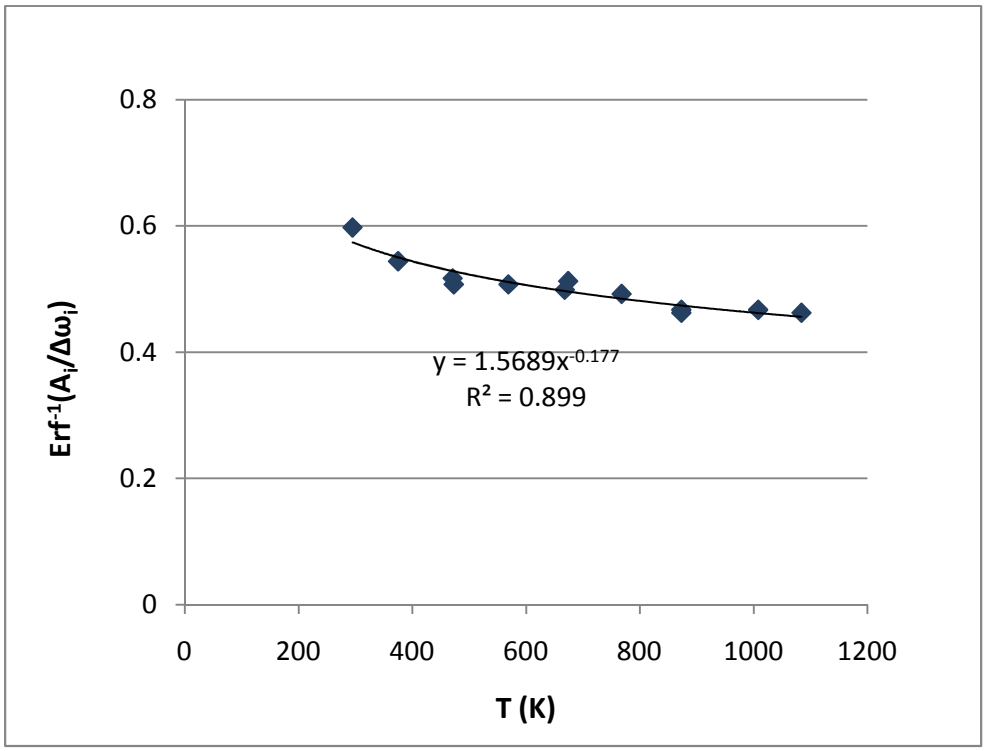

Figure 23. Plot of $Erf^{-1}(A_i/\Delta\omega_i)$ for Methane Gas at 7.65 μ

The value of the constant ξ_i obtained from the plot is -0.177, and by taking T_{g0} = 295 K the constant C_{i0} is equal to 0.207 with a standard deviation equal to 0.005. Thus for 7.56 μ band, equation 15 can be rewritten as follows:

$$A_{i,7.65\,\mu} = \Delta\omega_i(T_g) erf\left\{0.207\left(\frac{T_g}{T_{g0}}\right)^{-0.177}\sqrt{X}\right\} \qquad \textit{(Equation 69)}$$

For 7.65 μ band, the plot of the band emissivity against the temperature at various optical path lengths is given in Figure 24.

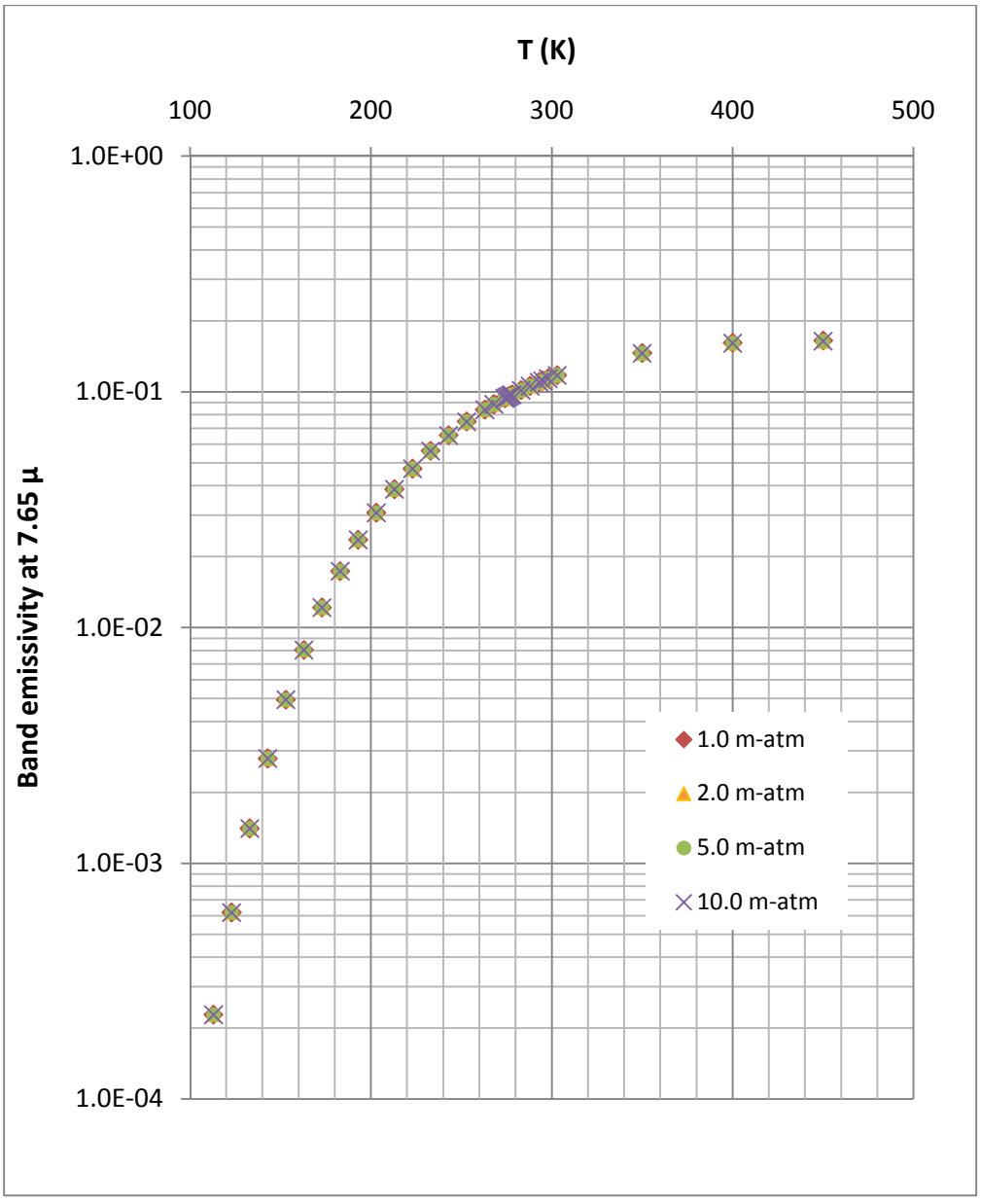

Figure 24. Band Emissivity of Methane Gas at 7.65 μ at Various Temperatures and Optical Path Lengths

The total emissivity was obtained by summing the band emissivities. The total emissivity of methane gas at temperature 110 – 350 K is given in Figure 25.

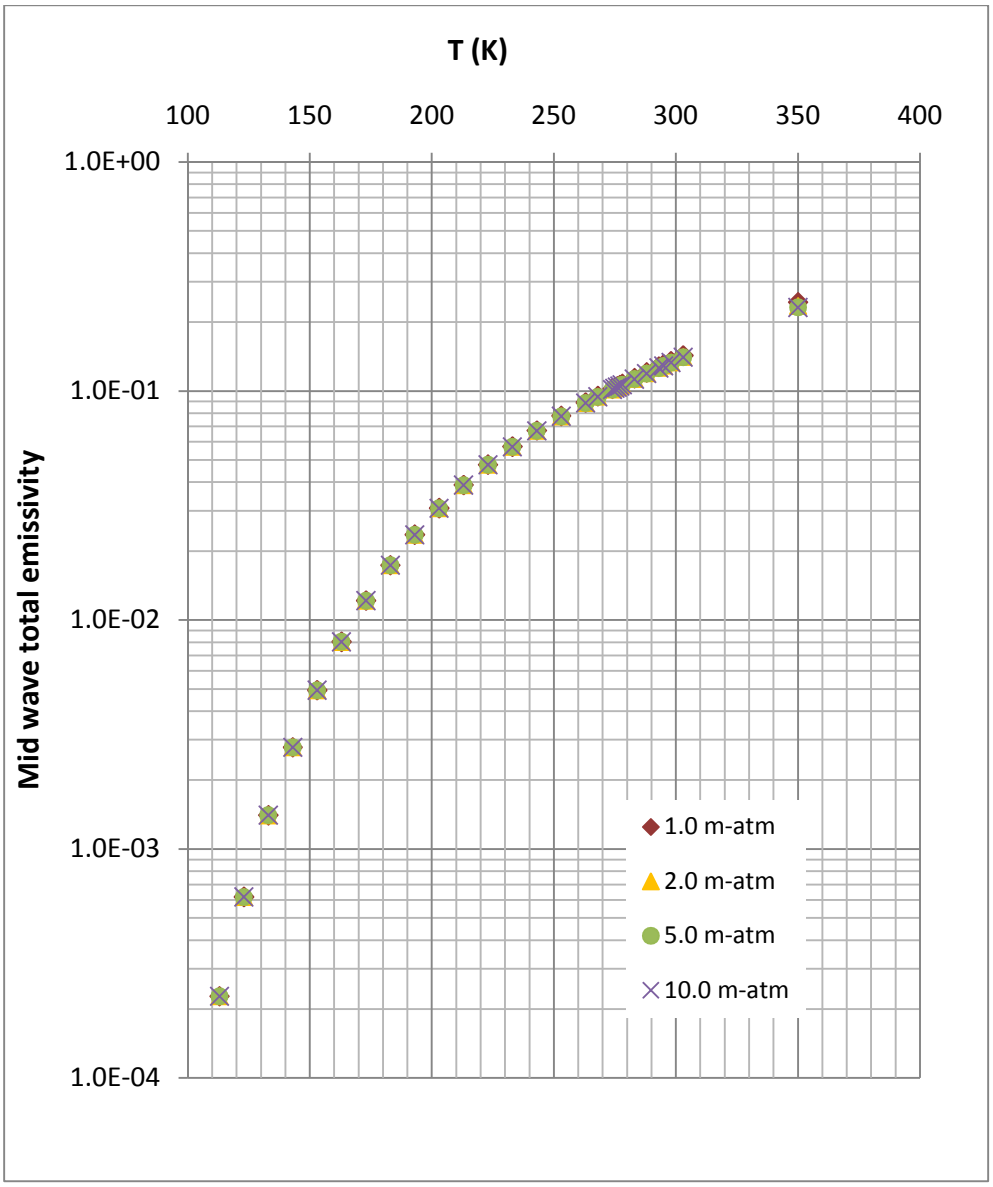

Figure 25. Total Emissivity of Methane Gas at Various Temperatures and Optical Path Lengths

4.3 Emissivity of Mixture of Methane and Atmospheric Gases

This section discusses the evaluation of the emissivity of a mixture of hydrocarbon gas and air in the atmosphere. As already described in the section 4.1, humidity, ambient temperature and optical path length are among the factors which are affecting the performance of infrared cameras in visualizing a target hydrocarbon gas. Water vapor and carbon dioxide are two gases in the atmosphere which have active absorbance within the mid-wave IR range. The contribution of these gases to absorbing and emitting the infrared energy depends on the partial pressure of each individual gas.

The local humidity and water vapor may significantly influence the quality of an infrared image in visualizing a dispersed hydrocarbon gas. Higher humidity will result in higher water vapor concentration in the atmosphere and thus higher absorbance of infrared radiation by this gas. The vapor pressure of water increases with temperature.

The temperature dependent of water vapor pressure was obtained from the experimental data taken from the Dortmund data bank. Figure 26 shows how the saturation water pressure increases as temperature increases.

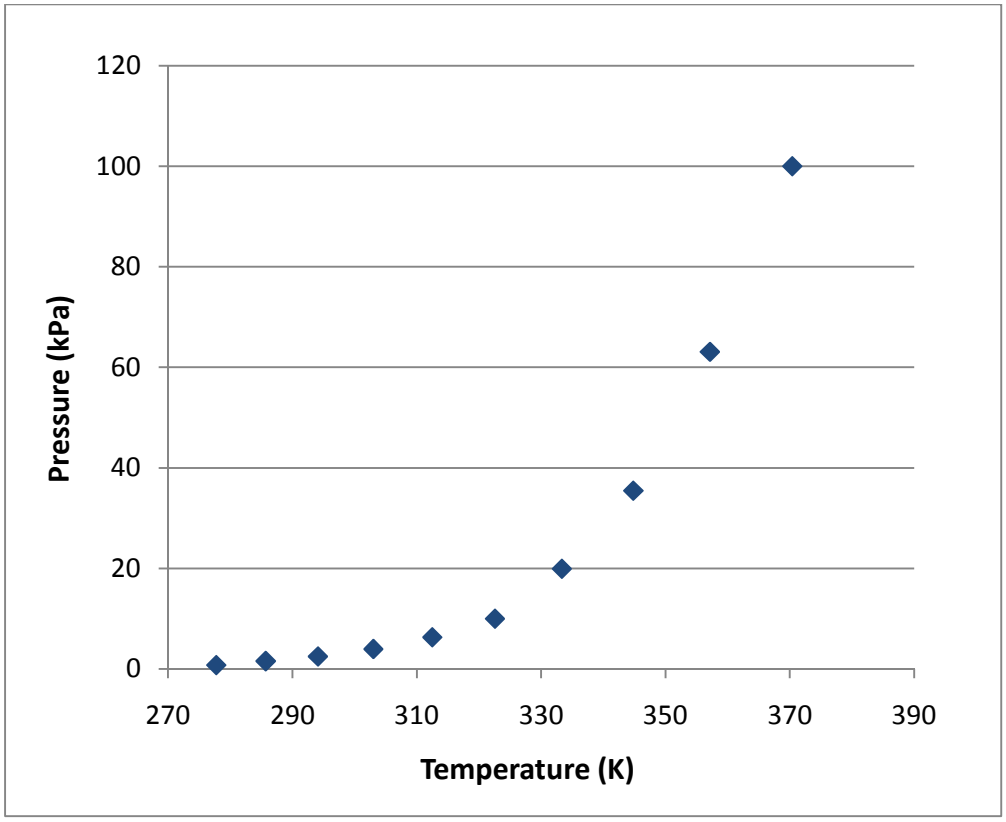

Figure 26. Saturation Vapor Pressure of Water as Function of Temperature

The amount of water vapor in the atmosphere is generally represented by relative humidity which is described as the ratio of the actual vapor density to the saturation vapor density. The saturated vapor density can be calculated from the saturation vapor pressure and temperature. Figure 27 shows the saturation vapor density of water as function of temperature.

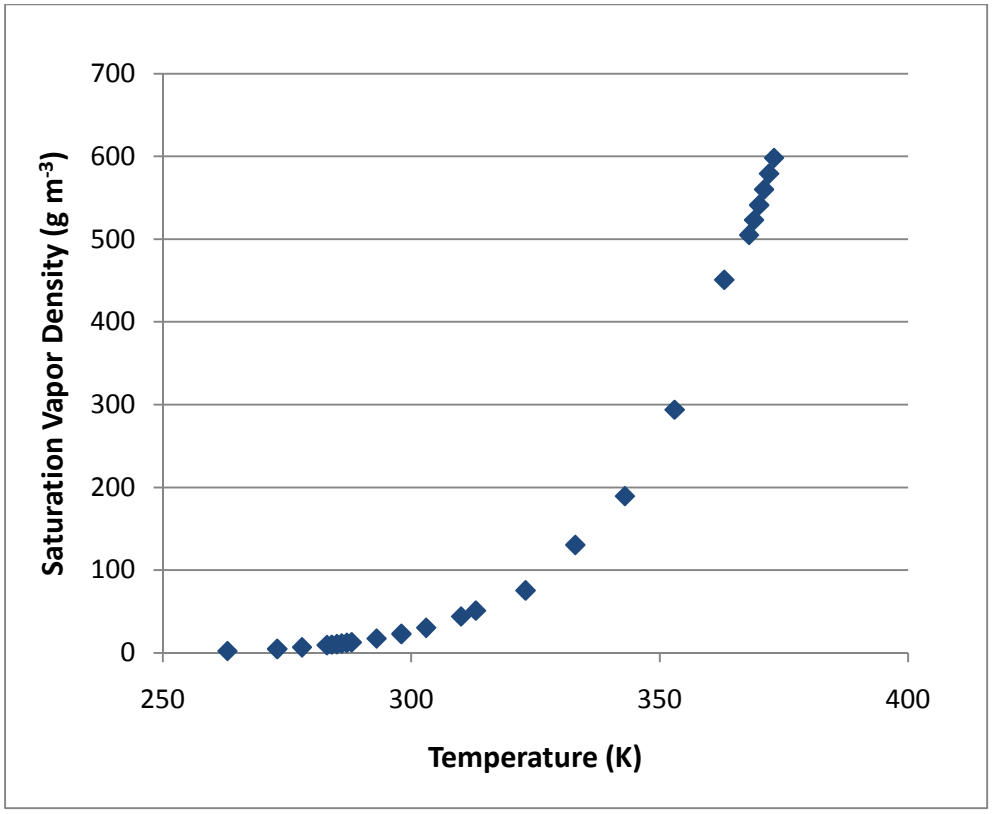

Figure 27. Saturation Vapor Density of Water

The partial pressure of water vapor in the atmosphere will increase when the relative humidity becomes higher. Since the saturation pressure of water vapor increased by temperature, the partial pressure of water in the atmosphere will also increase at higher temperature for the same relative humidity. Thus, the atmospheric water content is enhanced by increasing ambient temperature and relative humidity. Figure 28 shows the composition of the gases in the atmosphere for various humidity levels and ambient temperatures.

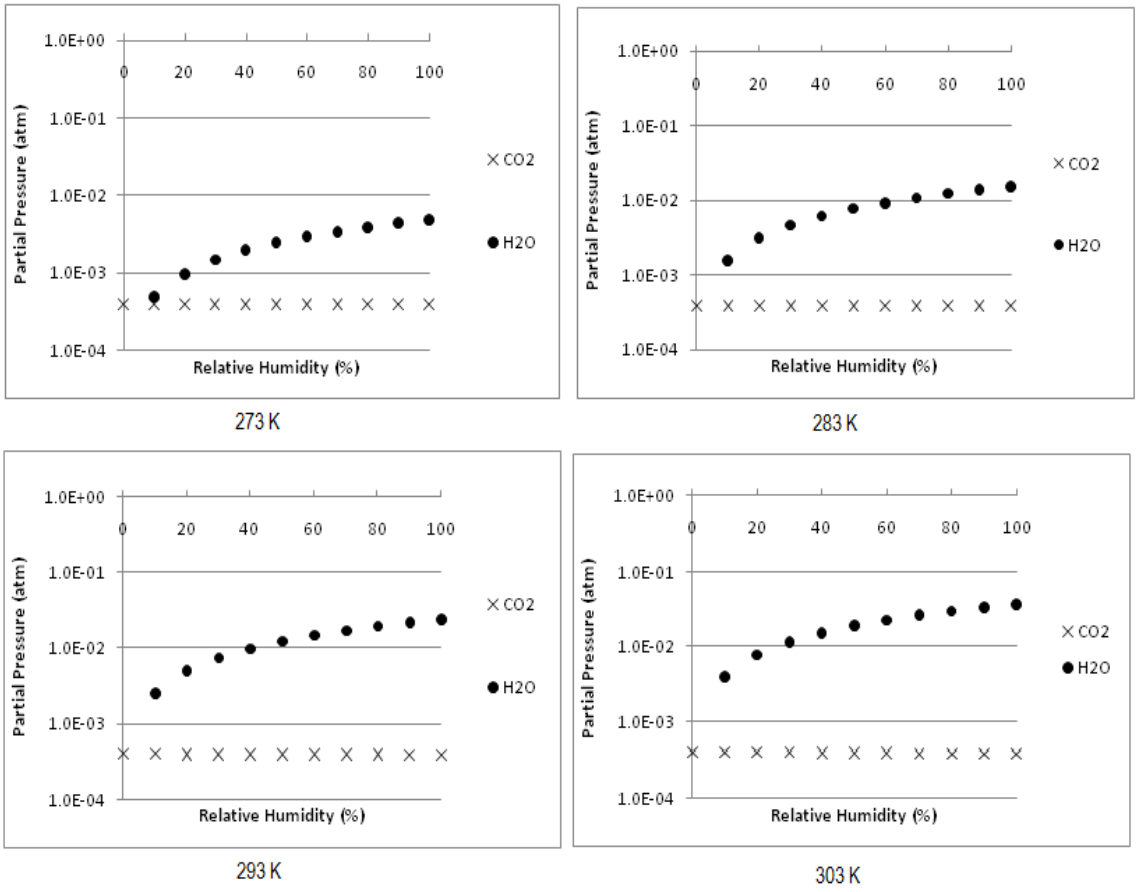

Figure 28. Partial Pressures of Atmospheric Gases at Various Temperatures and Humidity Levels

From Figure 28, it can be inferred that increasing the ambient temperature by 10 K from 273 K to 283 K will increase the partial pressure of water vapor by a factor of approximately 3. Increasing the ambient temperature by 20 K from 273 K to 293 K will result in an increase in concentration by a factor of 5. If the ambient temperature is increased by 30 K from 273 K to 303 K, the partial pressure of water vapor will increase by a factor of 12. This indicates that ambient temperature has a significant effect on determining the partial pressure of water vapor. As the relative humidity rises, vapor partial pressure also increases.

Relative humidity will have an effect on the gas mixture emissivity and the total radiation emitted by the object to detector. The emissivity of the atmospheric gas mixture was estimated using a weighted sum of grey gases models described in Equations 20 - 22. The equations show that the emissivity of a mixture is the sum of the product of the emissivity of an individual gas and the emissivity weighting factor. The emissivity of gas is a function of gas pressure and optical path length. The emissivity weighting factor was calculated by a polynomial function of temperature using the values given in Table 4 as the constants in the polynomial expression.

Some of the atmospheric constituents, including oxygen, nitrogen and argon, do not absorb infrared radiation in the mid wave range. Therefore, these gases are considered clear gases and the presence of these gases will not affect the emittance from the air mixture. However, carbon dioxide and water vapor have active absorbance in this range, so the presence of these two gases will influence the emissivity of the gas.

The concentration of carbon dioxide in air is small and relatively constant; therefore the absorbance by carbon dioxide is negligible. On the other hand, water vapor concentration may significantly increase at higher humidity levels; hence the absorbance by water vapor will also increase.

The emissivity of atmospheric gas mixtures as a function of relative humidity at various ambient temperatures and 1 m optical length is given in Figure 29. The figure shows that the emissivity of the gas mixture increases with higher relative humidity. Ambient temperature also has significant impact on the gas emissivity.

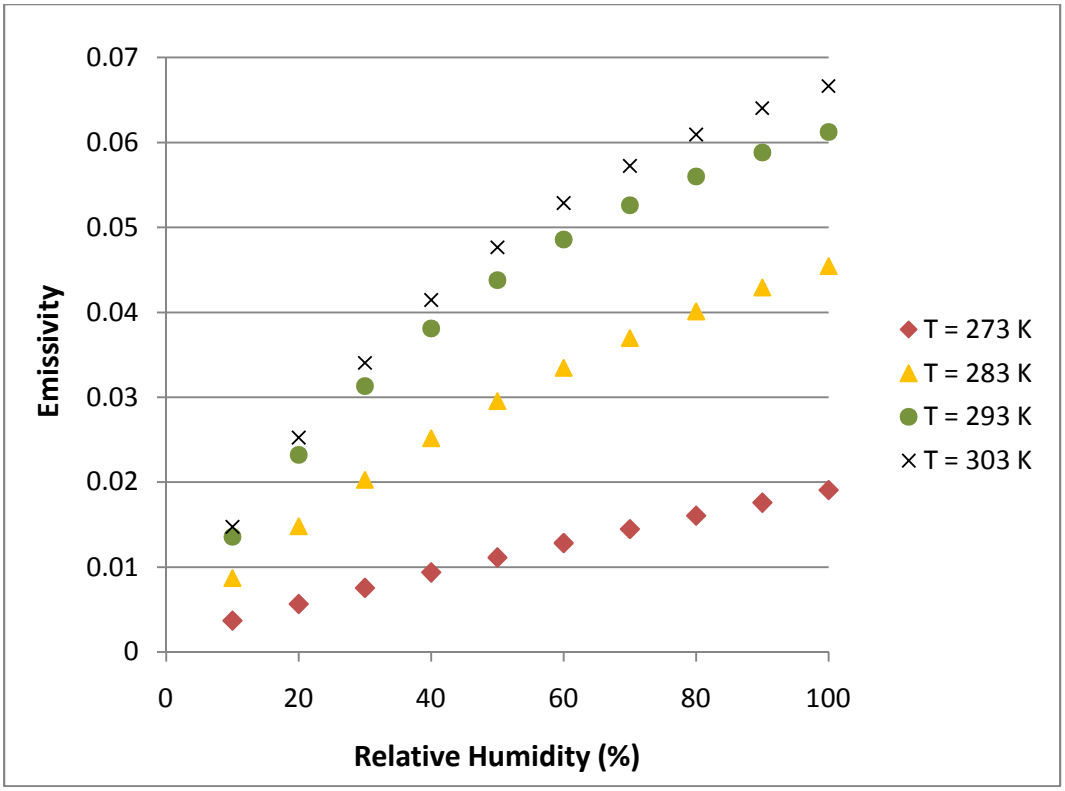

Figure 29. Emissivity of the Mixture of Atmospheric Gases as a Function of Water Vapor Concentration at Various Ambient Temperatures with the Absence of Hydrocarbon Gases

For a specific relative humidity, a higher ambient temperature results in a higher water vapor concentration (partial pressure). Higher ambient temperatures also cause an increase in the emissivity weighting factor. The emissivity value corresponds with the weighting factors and absorbing gas partial pressures and the significance of these parameters can be observed.

Several hydrocarbon gases absorb and emit radiation at a narrow mid wave range. When infrared optical imaging is used to visualize the hydrocarbon gases, it measures the radiation emitted from the gas to the camera's detector. As the hydrocarbon gas is released into the atmosphere, it will be mixed with air and dispersed

due to the air turbulence. Due to this air mixing process, the radiation impinging upon the camera's detector appears not only from the hydrocarbon gas but also from other gases in the atmosphere, including water vapor and carbon dioxide. In the presence of hydrocarbon gases, Equations 20-22 of the WSGGM can be utilized. However, the $k_i P$ term in Equation 22 is calculated by taking into account the partial pressure of the hydrocarbon gas as given in Equation 24. An evaluation of the emissivity of the mixture of methane gas and atmospheric gases was carried out in this work. The graph shown in Figure 30 demonstrates how concentration of the dispersed methane affects the emissivity of methane gas and air mixture.

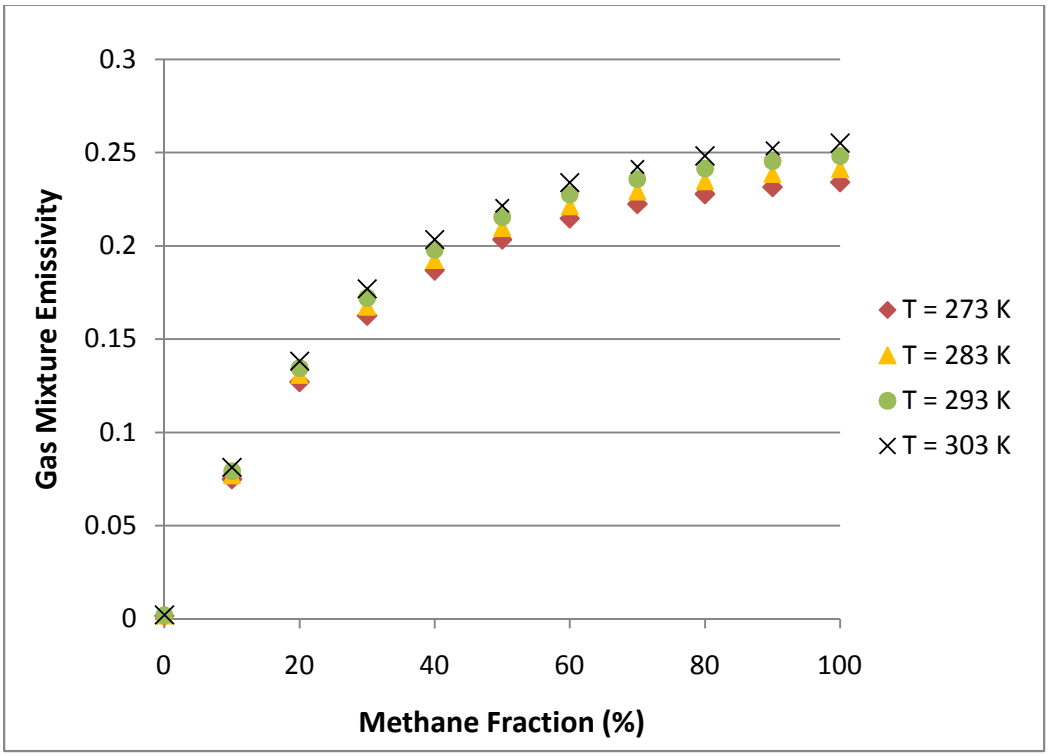

Figure 30. Emissivity of the Mixture of Dry Air and Methane Gas at Various Methane Concentrations and Temperatures

Compared to the emissivity of atmospheric gases alone as shown in Figure 29, the emissivity of the gas mixture with the presence of methane gas becomes higher as the methane gas concentration increases. Methane has a strong absorption in the mid wave IR range. The absorption coefficient of methane gas is tabulated in Table 4. The *kiP* term in equation 22 becomes larger at higher methane gas concentrations. The emissivity of the gas mixture in the presence of methane gas is also affected by the ambient temperature. At higher ambient temperatures, the emissivity of the gas mixture increases, as can be seen in Figure 30. At low methane concentrations the effect of temperature on the gas mixture emissivity is negligible. However, the effects of the increasing ambient temperature on gas mixture emissivity can be noticed at higher methane concentrations (> 20 %-v/v methane in air).

Figure 30 presents the emissivity of a mixture of methane gas and atmospheric gases when the air has no water content (dry air). In the presence of water vapor, the infrared radiation will not only be absorbed by methane gas but also the water molecules. At lower methane concentrations, the emissivity of the gas mixture is reduced by the presence of water vapors. The reduction in emissivity becomes more significant as the humidity level increases. From this evaluation, it is evident that the presence of water vapor attenuates the emissivity of the gas so that the amount of radiation transmitted to the camera detector decreases. However, when methane gas disperses to the atmosphere, the emissivity of the gas mixture is reduced at higher humidity. This reduction occurs because water has a lower absorption coefficient compared to methane and thus the total irradiation power transmitted to the camera

detector becomes lower. The attenuation due to the presence of water molecules is more apparent at lower methane concentrations. At higher methane concentration, the presence of water vapor does not significantly change the emissivity value of the gas mixture due to a lower concentration of water in the gas mixture.

The reduction in gas emissivity at different humidity levels is shown in Figure 31. The graph illustrates that in the absence of methane gas, higher humidity results in higher emissivity. In the presence of methane, the emissivity of the gas mixture increases at higher methane concentration.

The reduction in the emissivity value becomes more significant as the humidity level increases. Figure 32 shows the reduction in the emissivity value of a gas mixture when the water vapor reaches its saturation in the air mixture. The maximum reduction by water vapor in the atmosphere reaches 25% from a methane concentration of 20 – 60% in air at 303 K and 100% relative humidity.

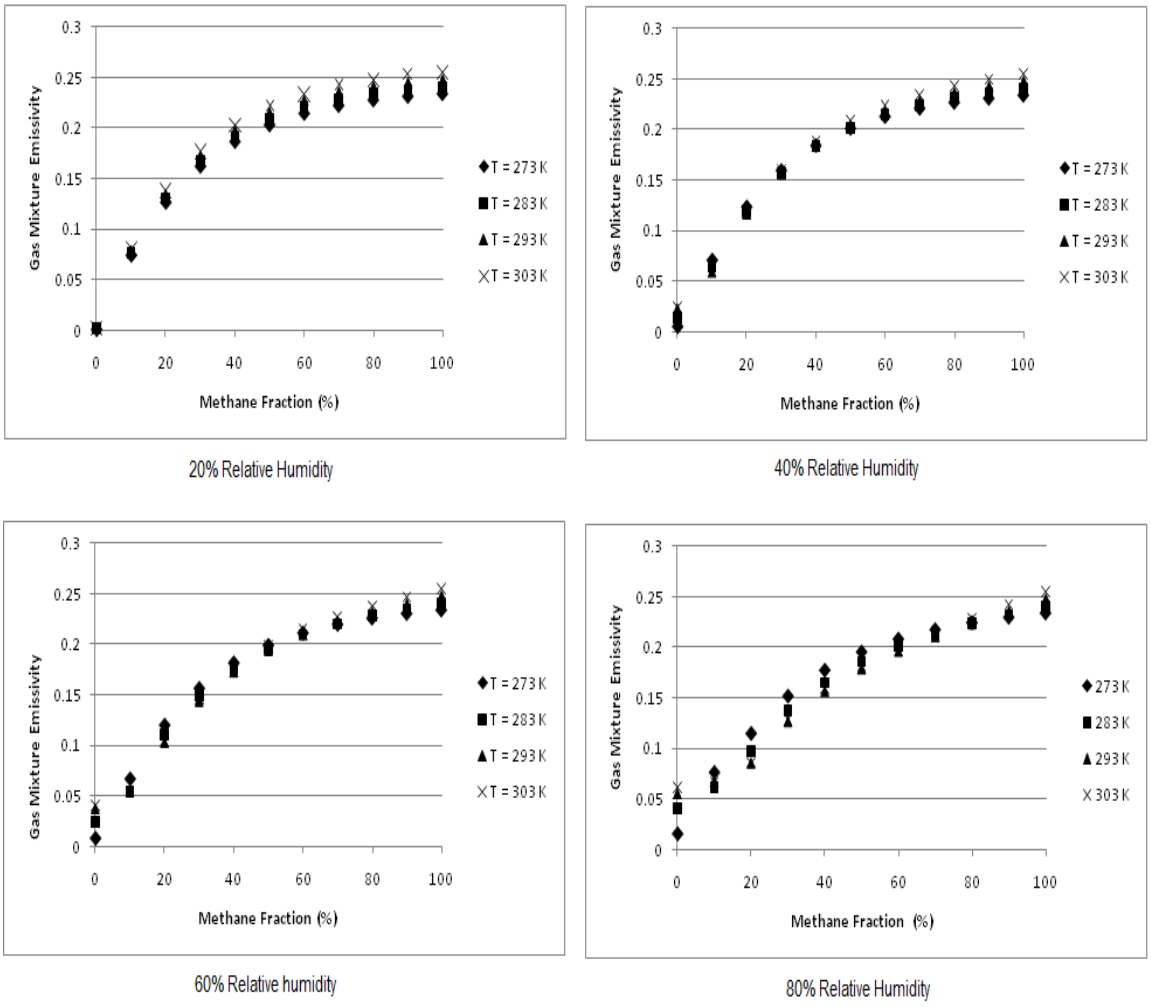

Figure 31. Emissivity of the Mixture of Dispersed Methane Gas and the Atmospheric Gases as a Function of Methane Gas Concentration at Various Humidity Levels and Ambient Temperatures

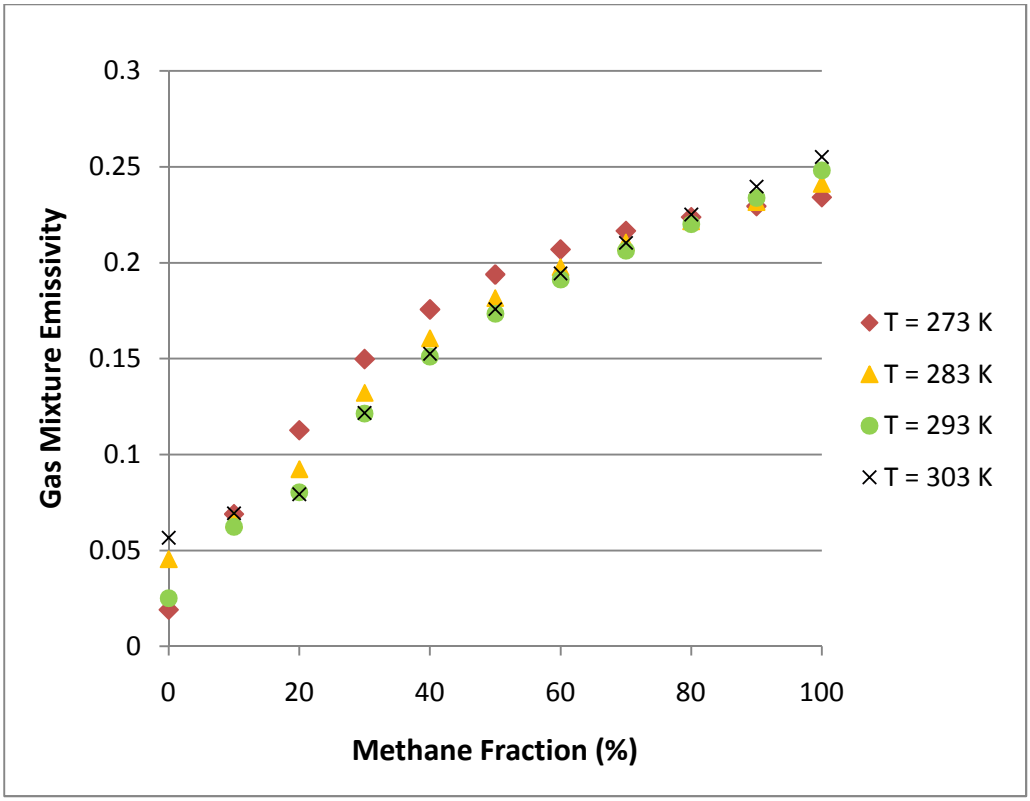

Figure 32. Emissivity of the Mixture of Dispersed Methane Gas and the Atmospheric Gases at 100% Relative Humidity at Various Ambient Temperatures

The concentration of water in the atmosphere is temperature dependent. For similar relative humidity, higher temperatures will cause higher water vapor pressure. Due to the increase in water vapor concentration, the emissivity of the mixture of methane and air will decrease at higher temperatures. Figure 33 demonstrates the changes in the emissivity value of gas mixture as ambient temperature increases.

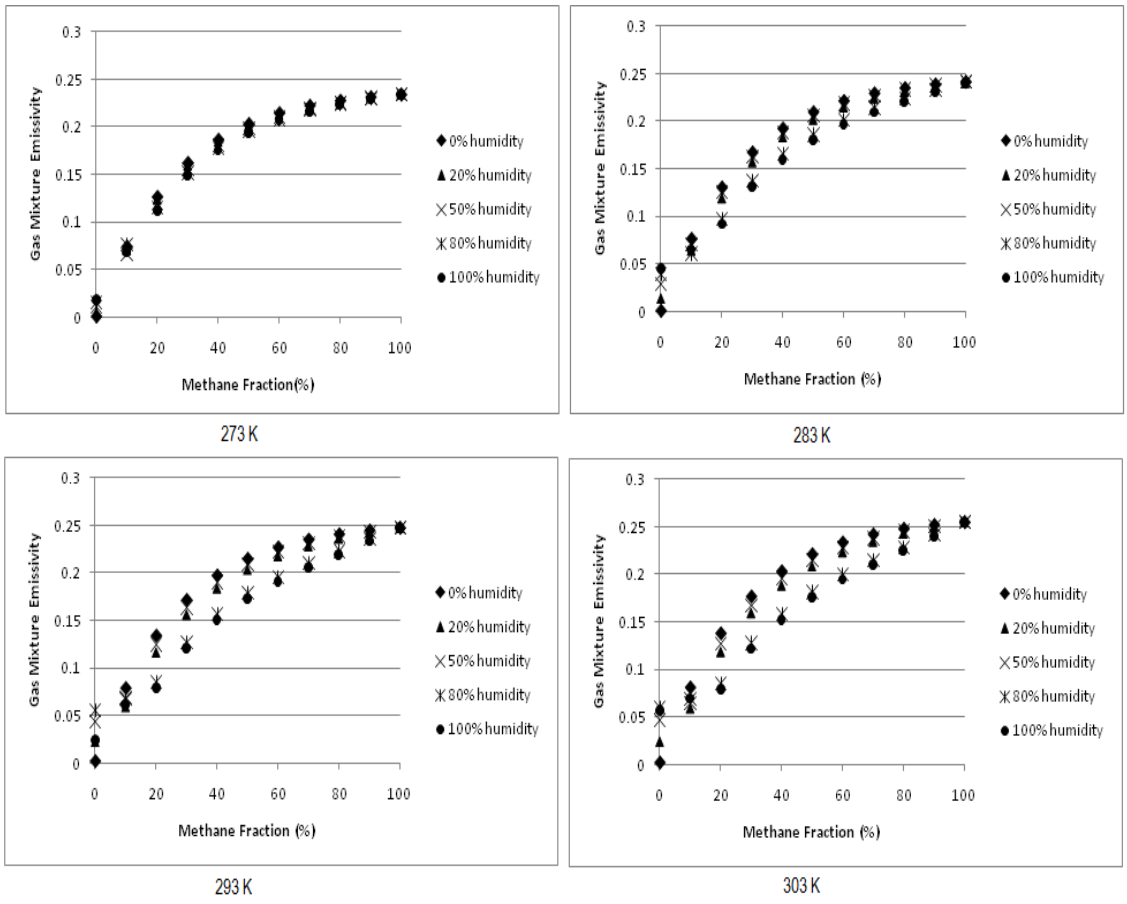

Figure 33. Emissivity of the Mixture of Dispersed Methane Gas and the Atmospheric Gases at Different Humidity Levels and Various Methane Gas Concentrations

From Figure 33, it can be inferred that at a lower temperature (273 K), the effect of humidity is a rather insignificant influence on the value of gas mixture emissivity. However, at a higher ambient temperature (303 K), the presence of water vapor can considerably reduce the emissivity of the gas mixture.

4.4 Estimation of LNG Vapor Temperature Profile by Including the Temperature-Dependent Emissivity Function

Analyses of the emissivities of pure methane at 111 – 350 K and mixtures of methane and atmospheric gases were presented in previous section. The emissivity value obtained is integrated into the Stefan-Boltzmann law or radiation in order to predict the actual temperature of the LNG cloud. The temperature of the gas cloud is determined by the different amounts of radiation emitted from the target and the background. For a target cooler than its background, the power difference is:

$$\Delta M = M_B - M_T \qquad \textit{(Equation 70)}$$

$$\Delta M = \sigma(T_B^4 - T_T^4) \qquad \textit{(Equation 71)}$$

For grey body, the emissivity is included into the expression to get the following:

$$\Delta M = \sigma\left(\varepsilon_{(T_B)} T_B^4 - \varepsilon_{(T_T)} T_T^4\right) \qquad \textit{(Equation 72)}$$

where T_T and T_B are the target and background temperatures, respectively. It is practical to specify it by its target-background difference *(ΔT)* where $\Delta T = T_T - T_B$.

By integrating the emissivity values, the actual net equivalent temperature difference (NETD) can be determined. Figure 34 shows how the emissivity function influences the radiation power transmitted to the infrared optical detector.

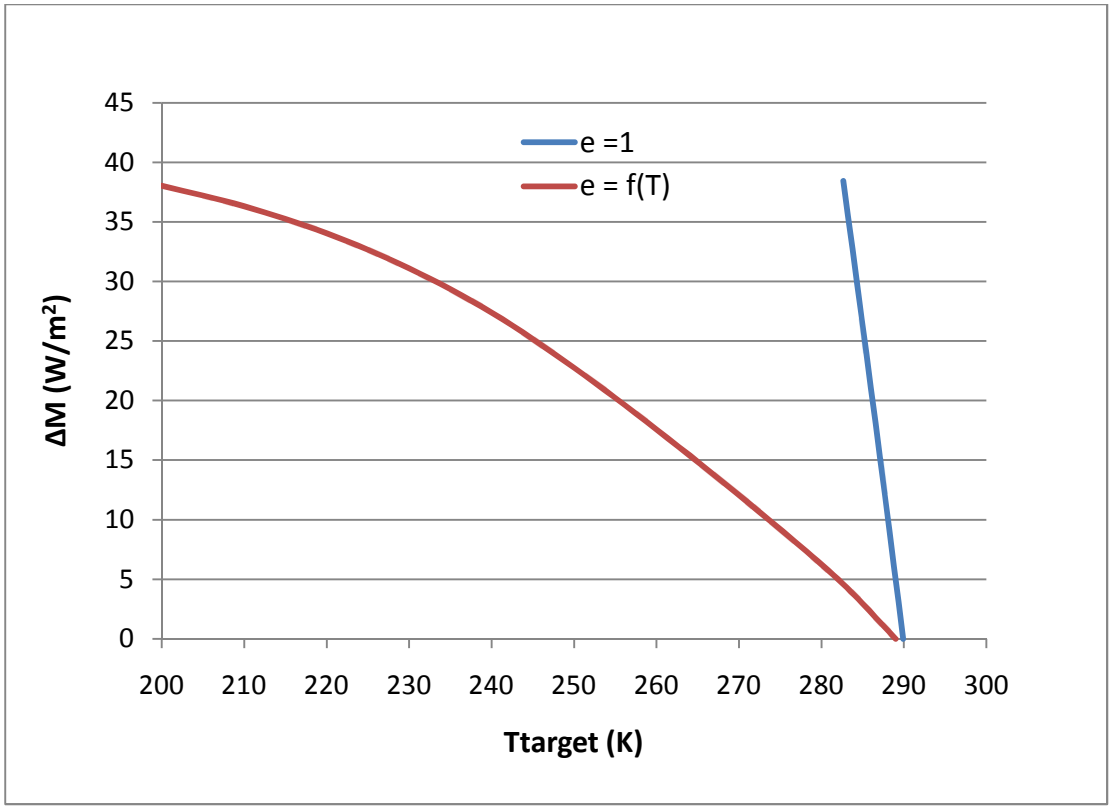

Figure 34. Comparison of Radiative Power of Methane Gas when Emissivity is Assumed to be Unity to the Radiative Power that Integrates the Emissivity Function into the Stefan-Boltzmann Expression

From Figure 34, it can be seen that at a constant ambient temperature, the NETD will be much smaller for radiation which assumes an emissivity value equal to unity. For the same amount of radiation, integrating the emissivity function into the radiation law will result in a larger temperature difference. The graph shown in Figure 34 was used to estimate the temperature profile of the cloud over time.

4.5 Development of Temperature-Concentration Correlation of Dispersed Liquefied Natural Gas

The temperature measurements taken using infrared imaging during the LNG spill tests were performed in real time in video format. The infrared camera was placed at 10 m distance from the pit in the crosswind direction. The LNG used for the purpose of these experiments contained 99.8% methane. Gas detectors were placed in the downwind direction to measure the methane concentration. The temperature of the LNG vapor increased as the LNG vaporizes and dispersed in the air due to the heat transfer process from the water in the environment. As it dispersed, LNG was diluted with the entrained air and resulted in a decrease in methane concentration. For those reasons, it can be assumed that there is a correlation between temperature and concentration.

In order to confirm that there is a strong correlation between temperature and concentration, the temperature and concentration changes over time were collected and plotted. Figure 34 was employed in order to estimate the actual temperature distribution of the gas cloud from the apparent temperature distribution shown in the thermogram. During this process it was assumed that the temperatures shown in the thermogram were depicting the temperatures at which the concentration of methane is the highest i.e. the cloud centerline. It is necessary to give this assumption since the cloud was a three-dimensional body but the thermograms were two-dimensional. This assumption was made because it can be expected that the maximum radiation transmitted to the camera detector came from the concentration absorbing the most gas, which was attained at the

highest methane concentration. Figure 35 shows several clips of the thermal images during the LNG dispersion process.

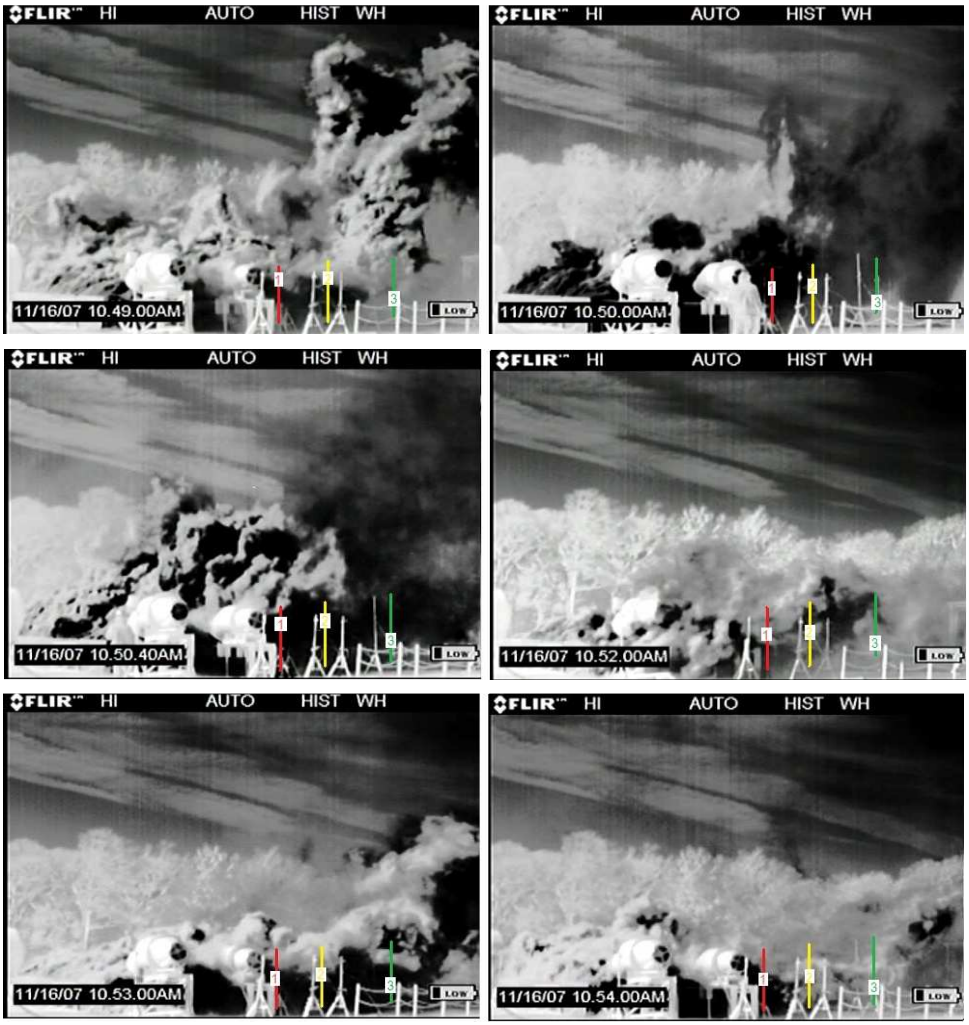

Figure 35. Thermal Images of LNG Vapor Dispersion over Time during the LNG Spill on Water Experiments

The gas detectors were placed at the poles shown in the east side of the figures. In order to develop the temperature-concentration relationship, three locations in the downwind direction were chosen, given as position 1 (0.4 m, -0.4 m, 2.3 m), 2 (2.3 m,

2.3 m, 2.3 m) and 3 (5.6 m, 5.6 m, 1.3 m) in the figures. Using the emissivity function demonstrated in the Figure 35, the actual temperature profile over time for each position could be calculated. Table 12 shows the comparison between the apparent temperatures shown in the thermograms and the actual temperatures.

Table 12. Apparent and Actual Temperatures of LNG Vapor Cloud

Time	Tambient	Tapp1	Tact1	Tapp2	Tact2	Tapp3	Tact3
	K	K	K	K	K	K	K
10:49:00	287.2	285.3	268	287.2	284	287.7	287
10:49:10	287.2	285.5	269	286.6	279	287.7	287.1
10:49:20	287.2	284.9	264	286.6	279	287.7	287.1
10:49:30	287.2	284.9	264	286.5	278	287.7	287.1
10:49:40	287.2	284.9	264	287.1	283.5	286.8	280
10:49:50	287.2	285.3	267	286.5	278	286.5	278
10:50:00	287	284.5	260	286.6	279	287.7	286.7
10:50:10	287	285.2	266	287.3	285	287.7	286.7
10:50:20	287	284.8	263	286.9	281	287.3	285
10:50:30	287	284.8	263	287.3	285.5	287.1	283
10:50:40	287	284.8	263	286.7	279	286.9	281
10:50:50	287	286.4	277	287.6	285.7	287.7	286.8
10:51:00	287.1	287	283	287.5	285.5	287.7	287
10:51:10	287.1	285.9	272	287.3	285	287.7	287
10:51:20	287.1	286.4	277	287.1	282.5	287.7	287
10:51:30	287.1	285.9	272	287.2	284	287.7	287
10:51:40	287.1	285.9	272	287.4	285.7	287.7	287
10:51:50	287.1	285.9	272	287.4	286	287.7	287.1
10:52:00	287.3	286	273	287.2	284.5	287.7	287.1
10:52:10	287.3	285.8	271	286.9	281	287.7	287.2
10:52:20	287.3	285.6	270	287.6	286	287.7	287.2
10:52:30	287.3	285.6	270	287.6	286	287.7	287
10:52:40	287.3	285.1	265	287.6	286	287.7	287.2
10:52:50	287.3	284.8	263	287.65	286.5	287.7	286.8
10:53:00	287.7	285.4	268	287.3	285	286.5	279
10:53:10	287.7	283.5	251	287.3	285	287.65	286.5
10:53:20	287.7	284.8	263	287.4	285.5	287.7	287
10:53:30	287.7	285.3	267	287.6	286	287.7	287
10:53:40	287.7	284.7	262	287.6	286	287.7	287
10:53:50	287.7	285.3	268	287.6	286	287.7	287
10:54:00	287.7	285.2	266	287.6	286	287.7	287

Figure 36 presents the methane concentration measurements from the gas detectors which were placed on the cloud centerline in the downwind direction. During the November 2007 test, the LNG spill was initiated at 10:30:45 am.

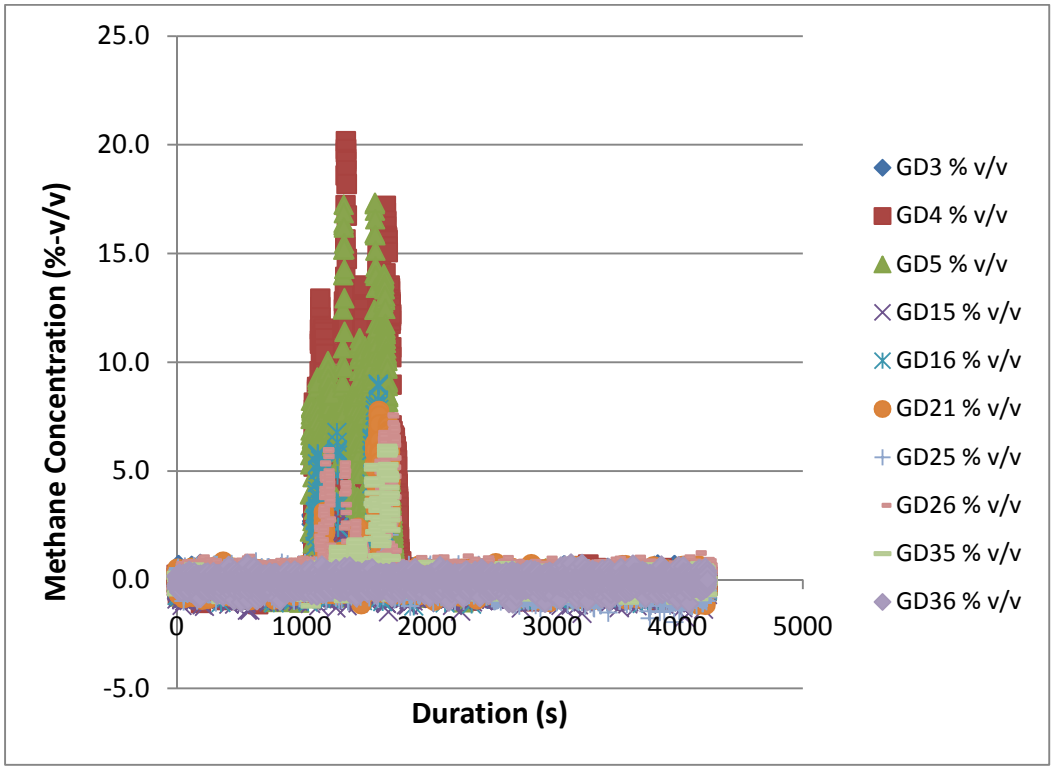

Figure 36. Concentration Profile of LNG Vapor at the Cloud Centerline from November 2007 LNG Spill of Water Test

From figure 36, it is indicated that the LNG was spilled on the water inside the pit at 1050 s. The figure also demonstrates that the concentration of methane decreased the farther downwind it traveled. GD03, GD04 and GD05 are the gas detectors at position (0.4 m, -0.4 m) at height 1.3 m, 2.3 m and 3.3 respectively. GD15, GD 16 and GD 21 are the gas detectors at position (2.3 m, 2.3 m) at the same height distribution as the previous set. GD25 and GD 26 are positioned at (5.6 m, 5.6 m) at the height of 1.3 m and 2.3 m respectively while GD 35 and GD 36 are the detectors at (10.7 m, 10.7 m) at the height 1.3 and 2.3 respectively.

It is shown in Figure 36 that GD04 (0.4 m, -0.4 m, 2.3 m) provides the highest methane concentration. The concentration continued to decrease as it moved downwind, and at position (10.7 m, 10.7 m) the methane gas concentration become negligible.

In order to develop the T-C correlation, the temperatures and concentrations for the 5 minute duration between 10:49:00 AM to 10:54:00 AM were to be compared. Figure 37 shows the concentration profile of the LNG plume at different positions within the chosen time span, as well as the temperature profile at the top portion of the wall pit measured by a thermocouple.

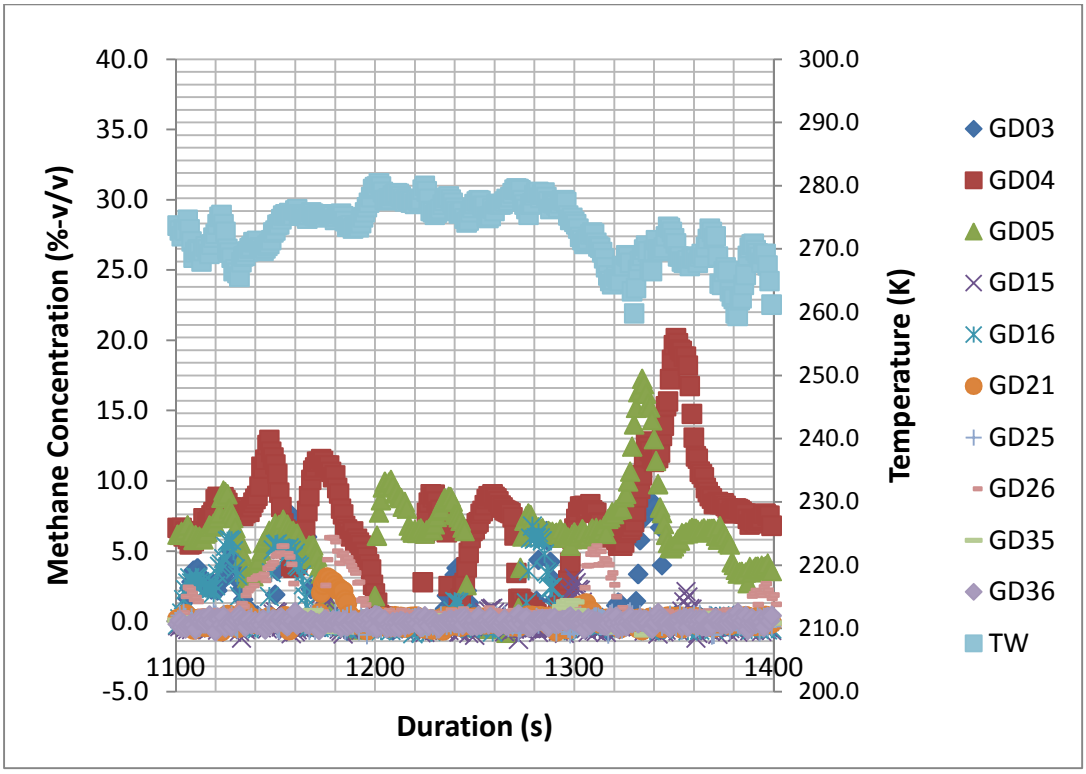

Figure 37. Concentration Profile of LNG Vapor and Temperature Profile Measured at the Edge of the Pit Wall

Figure 38 shows the comparison of apparent temperature shown in the thermogram to the predicted temperature and the temperature measured by thermocouple at position (0.4 m, -0.4 m, 2.3 m), The predicted temperature is obtained by correcting the apparent temperature by using the emissivity function.

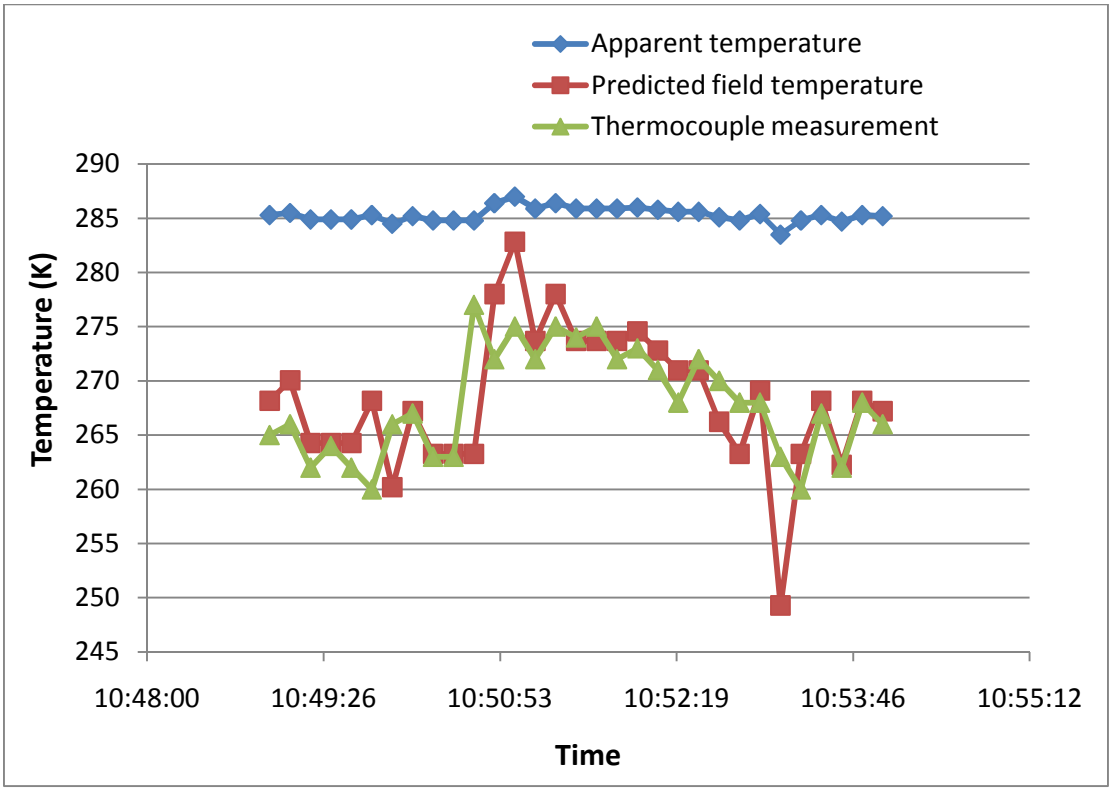

Figure 38. Temperature Profile of LNG Vapor at Position (0.4 m, -0.4 m, 2.3 m) from the Thermograms Compared to the Thermocouple Measurements

Temperature and concentration point measurements were collected within the time range for every 10 s for the three selected position. Position 1 (0.4 m, -0.4 m, 2.3 m) was chosen because the higher concentration of methane was observed at this position followed by position 2 (2.3 m, 2.3 m, 2.3 m) and position 3 (5.6 m, 5.6 m, 1.3 m) in the downwind direction.

Figure 39 demonstrates the concentration measured using the gas detector and the predicted field temperature profile obtained using the methodology developed in this research. As can be observed from this figure, the concentration was changing reversely

to the temperature. This behavior was expected because mixing a cold dense LNG gas with air causes a decrease in air temperature. If the LNG is at a higher concentration, the temperature drop will become more significant.

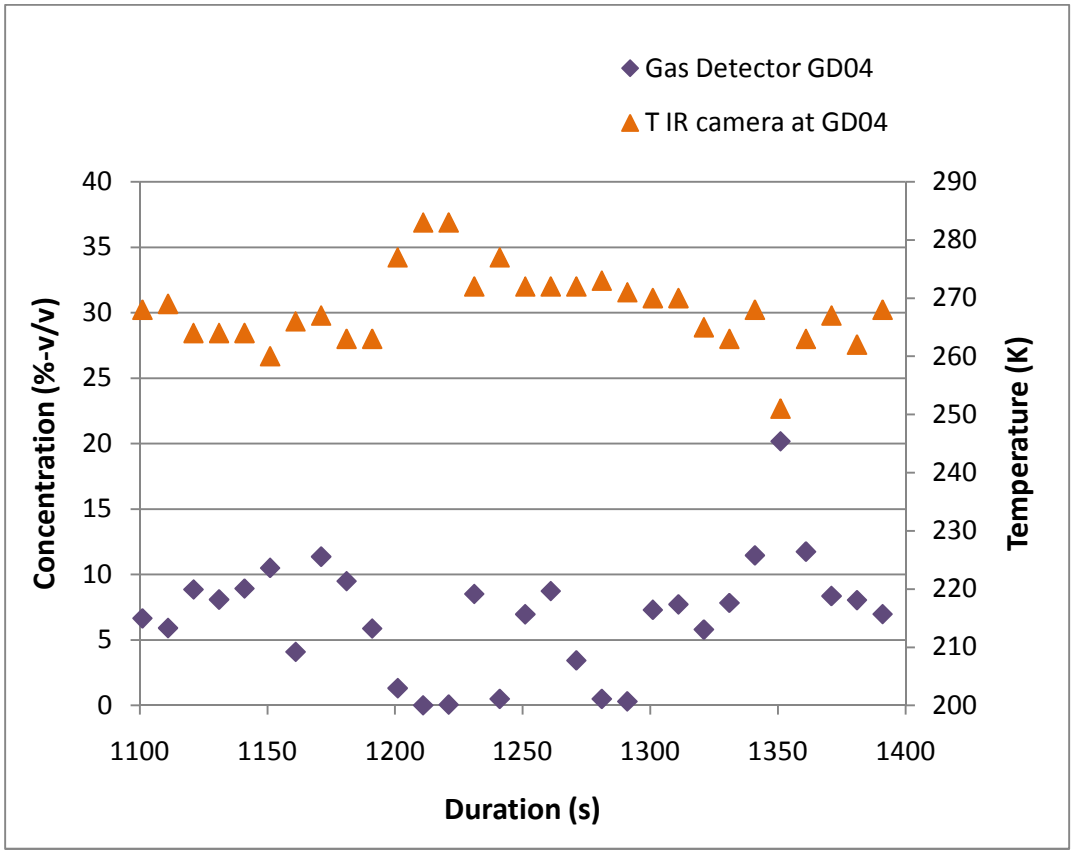

Figure 39. Temperature-Concentration Profile over Time of LNG Cloud at Position (0.4 m, -0.4 m, 2.3 m)

The concentration was then plotted against the temperature to obtain the correlation model. A linear regression was performed to obtain the constant in the correlation equation as well as the correlation coefficients. Figure 40 shows the

correlation for the concentration and temperature of methane vapor cloud at detector position 04 (0.4 m, -0.4 m, 2.3 m). Based on the solution for the molar budget and enthalpy budget, the correlation of gas concentration and temperature is linear. There are some scattering from the data collected; however, a trend for linear behavior can be observed from the concentration plot against temperature.

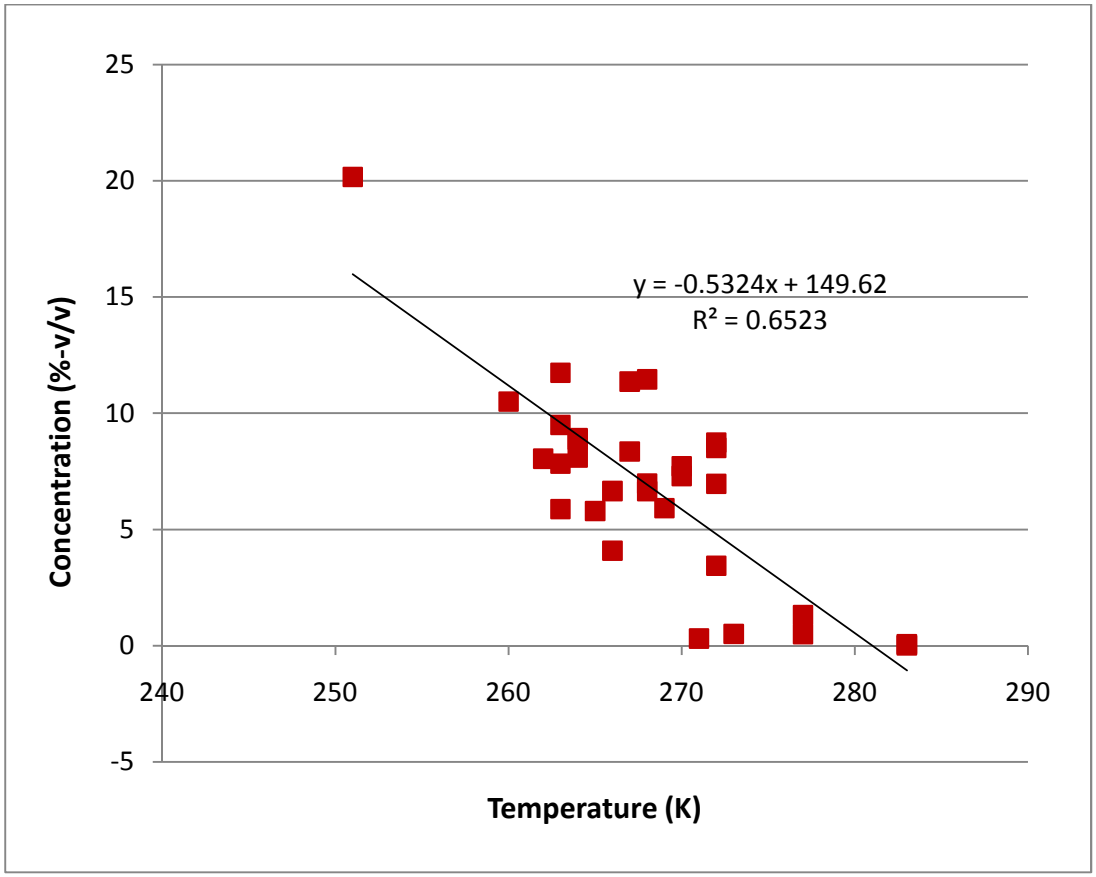

Figure 40. Linear Relationship of Temperature and Concentration for LNG Vapor Cloud at Position (0.4 m, -0.4 m, 2.3 m)

The comparison of temperature estimated from converting the apparent temperature to the predicted field temperature with the temperature measured using thermocouple at position (2.3 m, 2.3 m, 2.3 m) is shown in Figure 41. As can be seen in the figure, prediction using of the LNG field temperature by including the emissivity function into the Stefan-Boltzmann law shows a good agreement to the temperature measured by thermocouples.

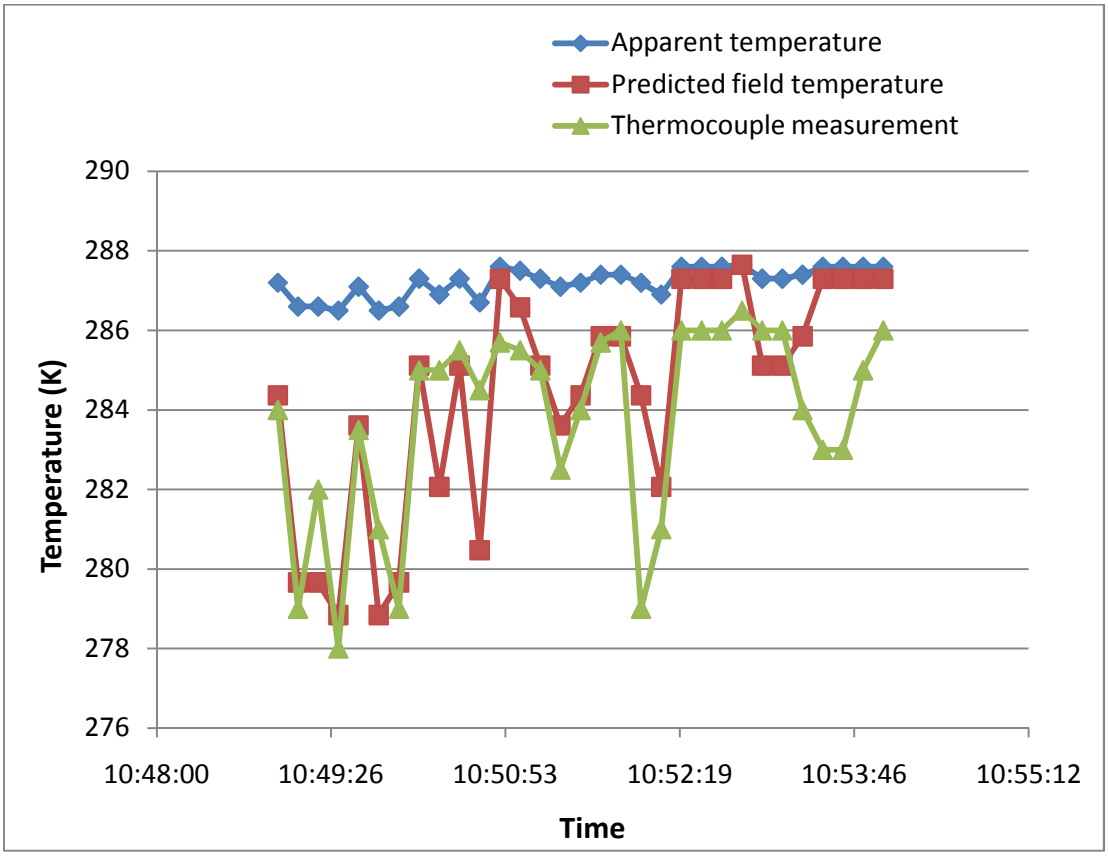

Figure 41. Temperature Profile of LNG Vapor at Position (2.3 m, 2.3 m, 2.3 m) from the Thermograms Compared to the Thermocouple Measurement

Similarly, the temperature and concentration profile for gas concentration and temperature at position 16 and 26 are compared. Correlation coefficients are obtained by plotting the concentration against temperature. Concentration and temperature data at a distance of 2.3 m downwind at position GD16 (2.3 m, 2.3 m, 2.3 m) from the pit is demonstrated in Figure 42.

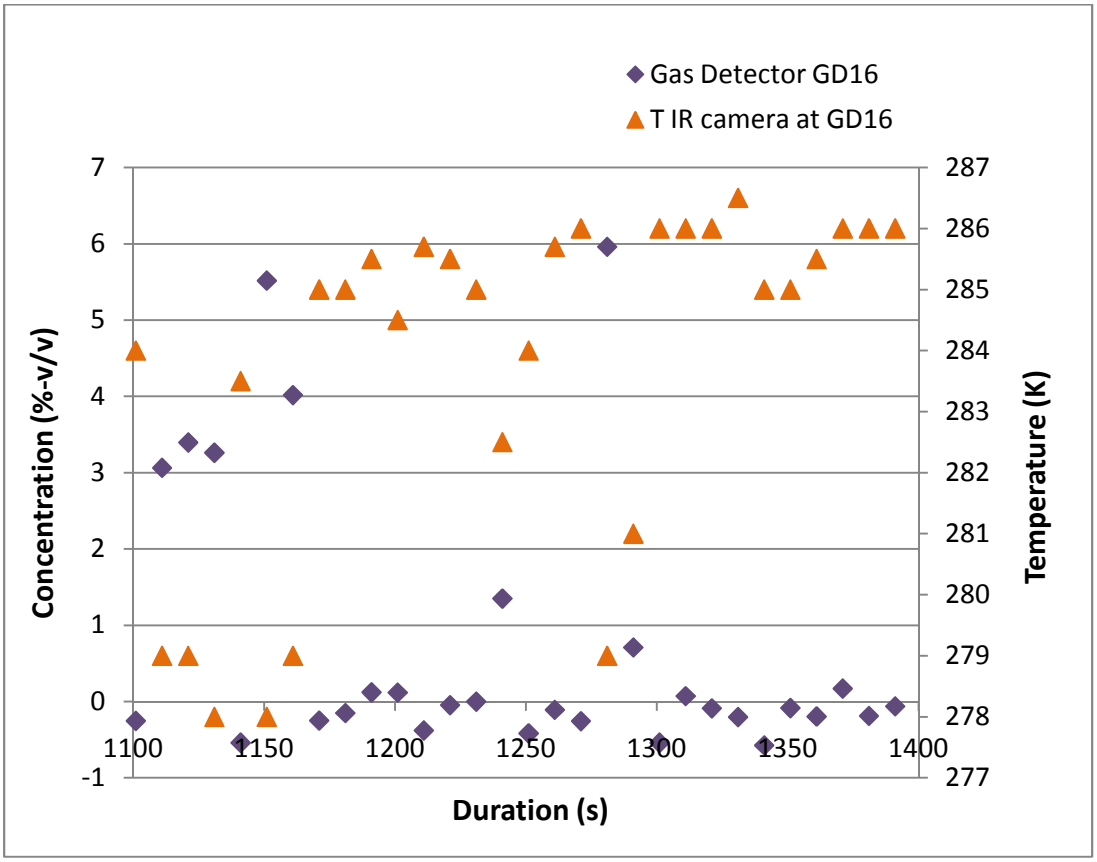

Figure 42. Temperature-Concentration Profile over Time of LNG Cloud at Position (2.3 m, 2.3 m, 2.3 m)

The trend which correlates the gas concentration and temperature from measurement at position (2.3 m, 2.3 m, 2.3 m) is given in Figure 43. The trend also shows a linear relationship between the concentration and temperature of the LNG vapor.

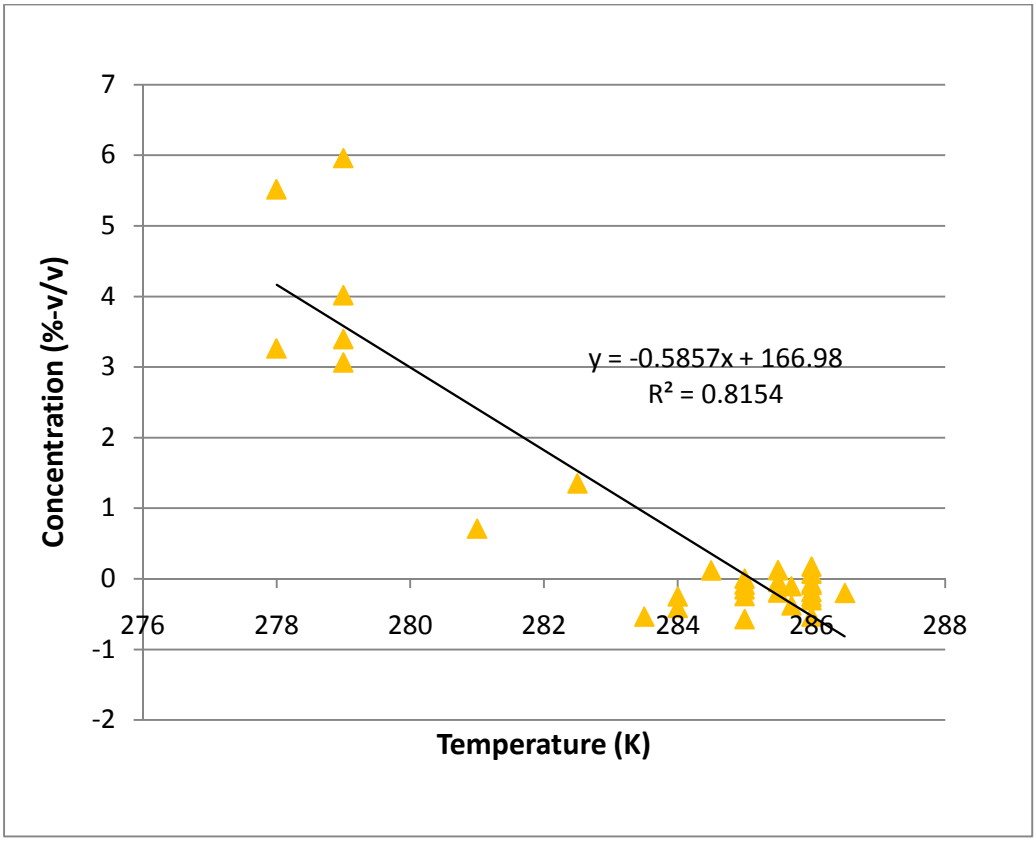

Figure 43. Linear Temperature and Concentration Relationship for LNG Vapor Cloud at Position (2.3 m, 2.3 m, 2.3 m)

The temperature profile obtained from the thermogram image and the corrected temperature distribution is compared to the temperature distribution from thermocouple measurement at position (5.6 m, 5.6 m, 1.3 m) in Figure 44. At this position, the conversion of the apparent temperature by using the emissivity factor also shows good prediction to the actual field temperature of the LNG vapor.

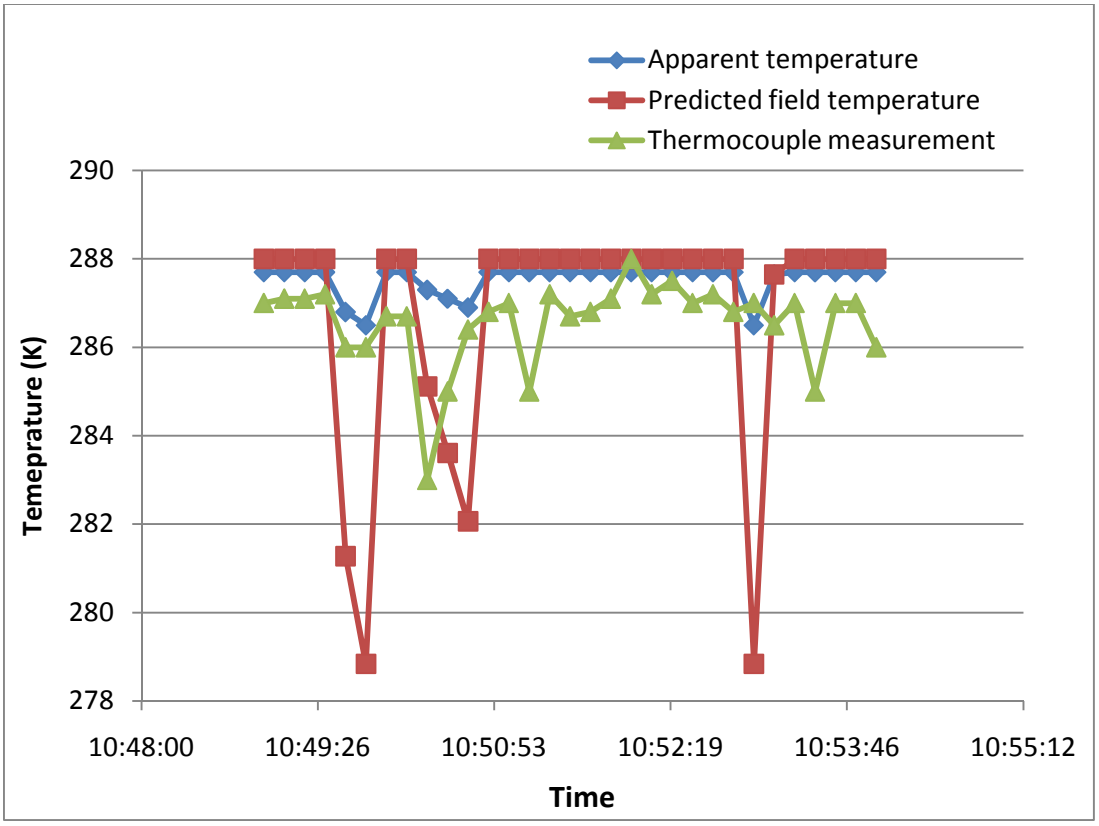

Figure 44. The Temperature Profile of LNG Vapor at Position (5.6 m, 5.6 m, 1.3m) from the Thermograms Compared to the Thermocouple Measurements

Concentration and temperature data at a distance of 2.3 m downwind at position GD 26 (5.6 m, 5.6 m, 1.3 m) from the pit is depicted in Figure 45.

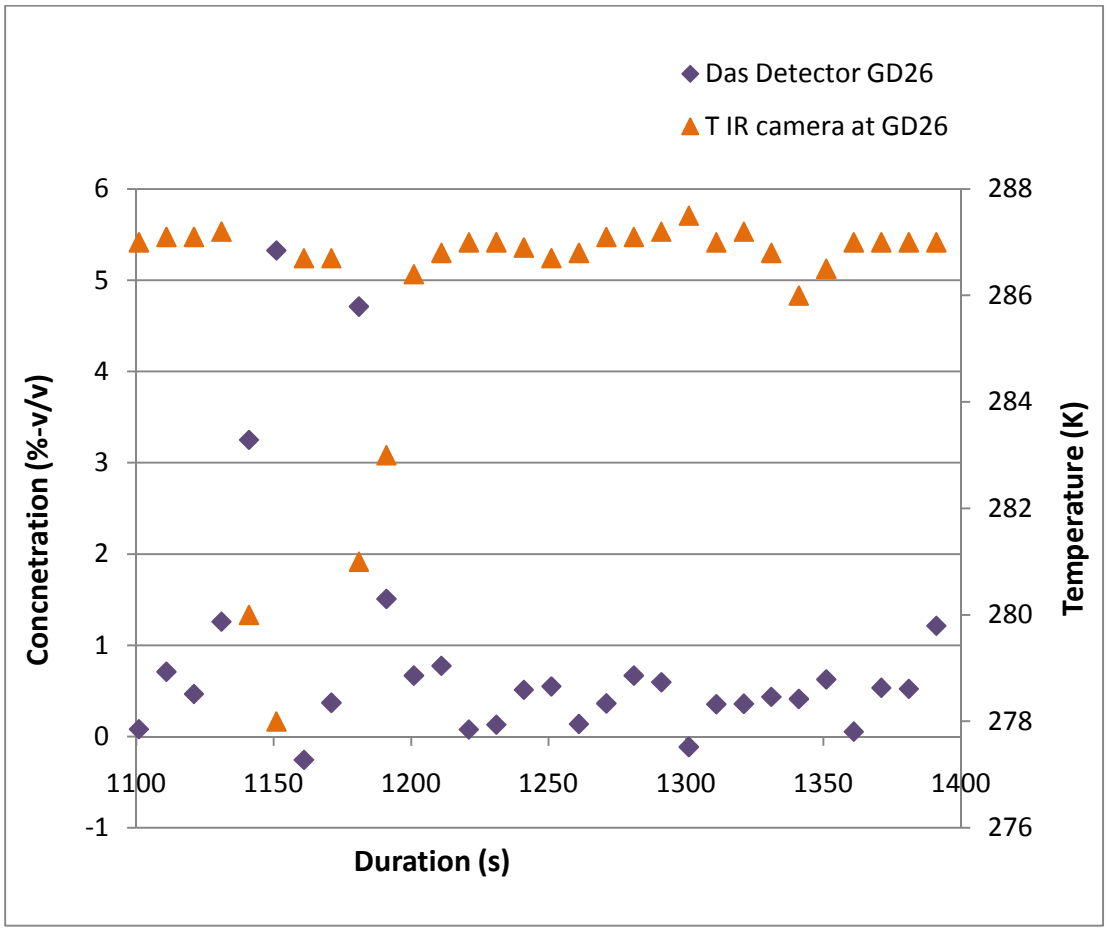

Figure 45. Temperature-Concentration Profile over Time of LNG Cloud at Position (5.6 m, 5.6 m, 1.3 m)

The trend which correlates the gas concentration and temperature is given in Figure 46. Similarly, it is observed that concentration is linearly correlated to the temperature at this position as well.

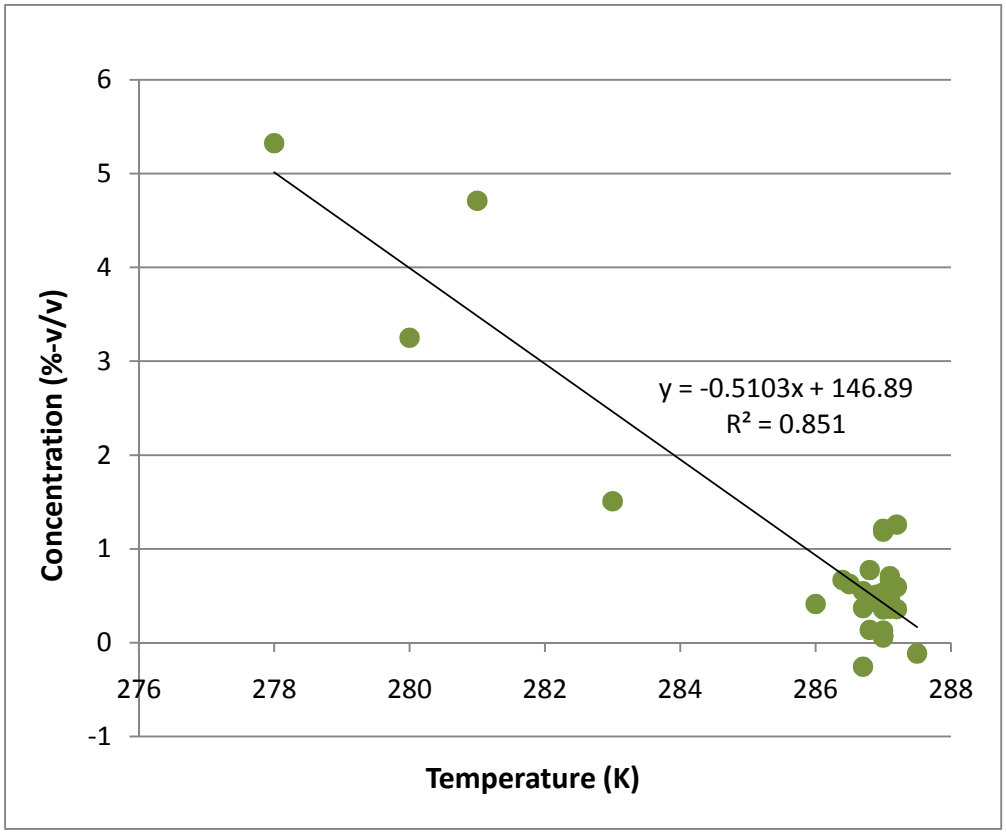

Figure 46. Linear Behavior of Temperature and Concentration Relationship for LNG Vapor Cloud at Position (5.6 m, 5.6 m, 1.3 m)

From the overall plot of gas concentration and temperature, it is revealed that there is a strong relationship between concentration and temperature. Although there are some scattering of the data, it can be seen clearly that the values are posed in the vicinity

of a diagonal line, thus it can be concluded that there is a good approximation of the gas concentration and temperature correlation.

As can be observed in the figures above, the changes in concentration occur conversely to the changes in temperature. A linear regression in the form of C = a – bT can be drawn from the plot. The coefficients and correlation coefficients used to predict the gas concentration of an LNG vapor cloud from the gas temperature for three observed positions are given in Table 13. The correlation coefficients obtained from the experimental data is compared to the coefficients model obtained from simulation by Sklavounos & Rigas (2005).

Table 13. Comparison of Coefficients and Correlation Coefficients for Linear Regression Model C = a – bT between Concentration and Temperature for LNG Vapor Cloud Obtained from the Experimental Data Compared to Simulation Model

	Coefficient Value		**Correlation coefficients, R^2**
	a	**b**	
Position 1 (0.4 m, -0.4 m, 2.3 m)	-0.53	149.62	0.65
Position 2 (2.3 m, 2.3 m, 2.3 m)	-0.58	166.98	0.82
Position 3 (5.6 m, 5.6 m, 1.3 m)	-0.51	146.89	0.85
Model (Sklavounos & Rigas, 2005)	-0.42	125.4	0.98

Using the linear expressions, the gas concentrations versus temperatures are plotted for the experimental data and simulation results are given in Figure 47. From the figure, it can be seen that the regression model is in a good agreement with experimental data for higher gas temperatures. However, for lower temperatures the deviation between the model and experimental data show higher deviation.

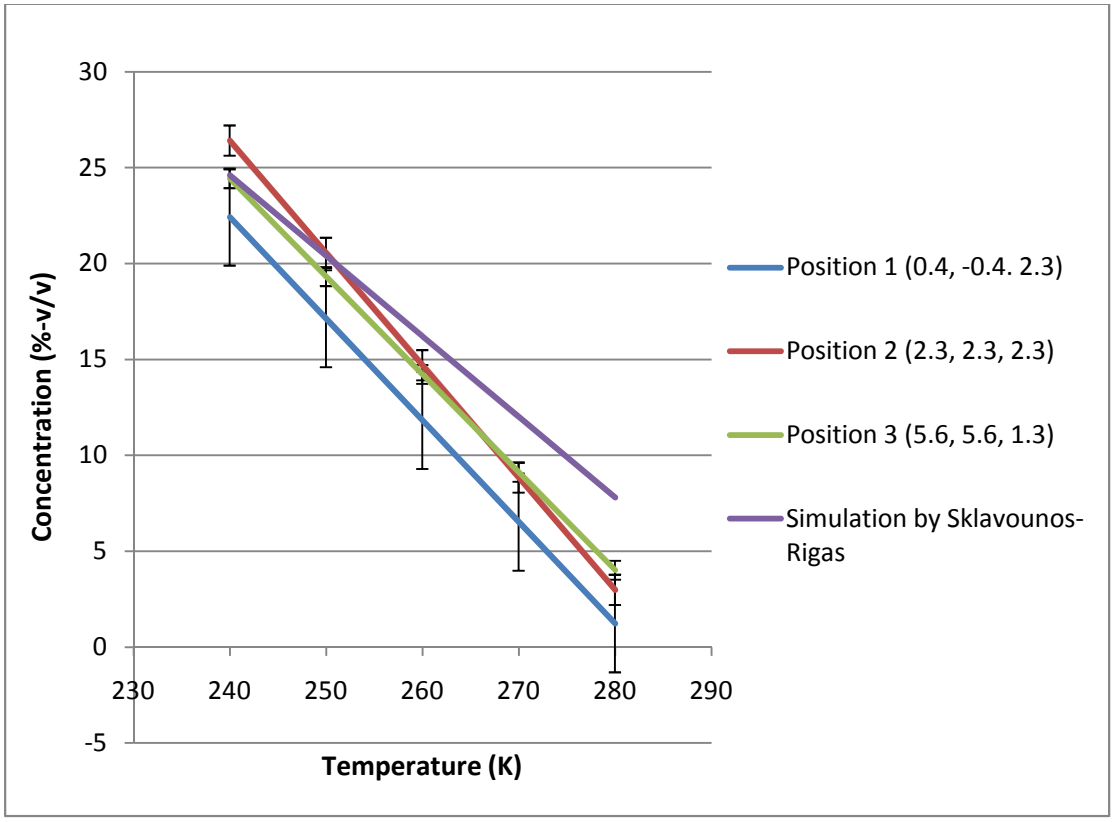

Figure 47. The Correlation for Methane Gas Concentration and Temperature from the Experimental Data Compared to the Simulation Performed by Sklavounos & Rigas (2005)

4.6 Summary of Section 4

The application of the infrared imaging technique for monitoring and visualizing the LNG vapor cloud is demonstrated in this section. The infrared camera can be used as a non-contact temperature measurement of the gas. However, from the field tests, a discrepancy between the actual gas temperatures and the temperatures depicted by the thermogram is exhibited. Several published works indicated that the discrepancy occurred due to the assumption of the emissivity value of the camera detector's algorithm. The camera detector assumes the emissivity of the object equal to unity. However, the emissivities of gas and mixture of gas have lesser value than unity.

In this section, the emissivities of methane gas at various temperatures and optical lengths are approximated using the band absorption model. The emissivities of the mixture of methane and atmospheric gases are estimated using the weighted sum of the grey gases model. The emissivity function is embedded into the Stefan-Boltzmann law or radiation in order to obtain the prediction of the actual gas temperature distribution. The model predicts the gas temperature very well compared to the temperature measurement using thermocouples.

Finally, the obtained gas temperature distribution is compared to the concentration obtained from the gas detector measurement. The data from three locations in the downwind direction are chosen to compare the gas concentration and temperature distribution in order to develop a relationship between the concentration and temperature. The results show that the changes in concentration happen inversely to the

changes in temperature. A linear regression model is obtained by plotting the concentration against temperature. Compared to the model published in the literature for LNG vapor gas concentration and temperature correlation, the experimental data demonstrate good agreement with the model.

5. RESULTS AND DISCUSSIONS PART II: APPLICATION OF INFRARED IMAGING FOR THE DETECTION AND MEASUREMENT OF EMISSIONS FROM NATURAL GAS SYSTEMS

In this section, the results from the study on the application of the infrared imaging techniques for detecting fugitive gas leaks from natural gas pipeline systems are presented. The aim of this part of research was to develop a correlation between the gas discharge rate, the distance the methane gas plume travels and the concentration at which it is still detectable by the infrared optical imaging system.

A methodology was developed which correlates the gas discharge rate of a natural gas leak in a pipeline with the size of the plume and the distance the gas travels before it is of a minimum concentration detectable by the infrared optical imaging system. The gas release rate from a hole in a pipe is calculated. The correlations are developed for different meteorological conditions. Using these correlations, one could estimate the emission rate of a fugitive gas from a pipeline by observing the distance the gas travels from the source to the minimum detectable concentration.

5.1 Simulation of Methane Gas Discharge and Dispersion

The leak rate of methane gas at different upstream pressures and temperatures is calculated using Equation 26 and Equation 27 described in the previous section. At upstream pressures higher than 187 kPa, the gas becomes choked and the gas velocity reaches sonic velocity. The gas mass flux keeps increasing at sonic conditions because the density of the gas is increased. A slight temperature decrease of the natural gas inside the pipeline will not affect the amount of gas discharged from the leak source. The gas mass flux as a function of upstream pressure is given in Figure 48.

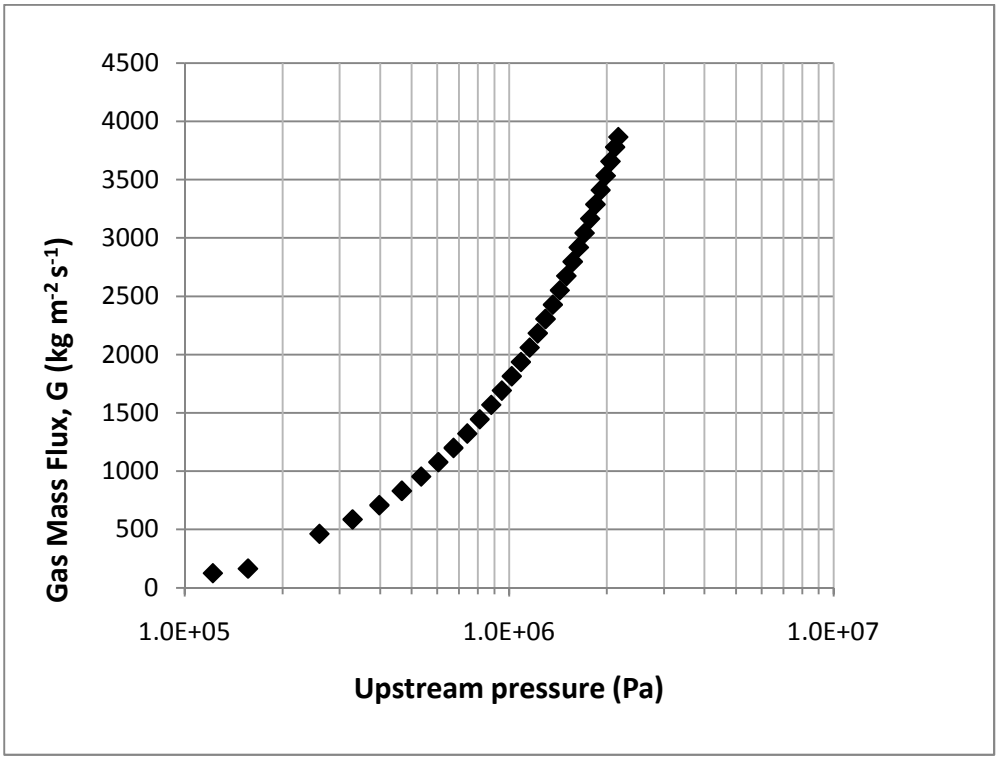

Figure 48. Methane Gas Mass Flux at Various Upstream Pressures

Gas is usually transported at ambient conditions, except for underground pipelines in which the temperature of the gas is slightly lower than the ambient temperature during warm weather and higher than ambient temperature during cold weather. Figure 49 shows the mass discharge rate of the gas from 2.5 mm leak at various pressures and temperatures. From the figure, it can be concluded that the mass flow rate highly depends on the upstream pressure, but the effects of a slightly increasing or decreasing temperature is insignificant to the gas mass flow rate.

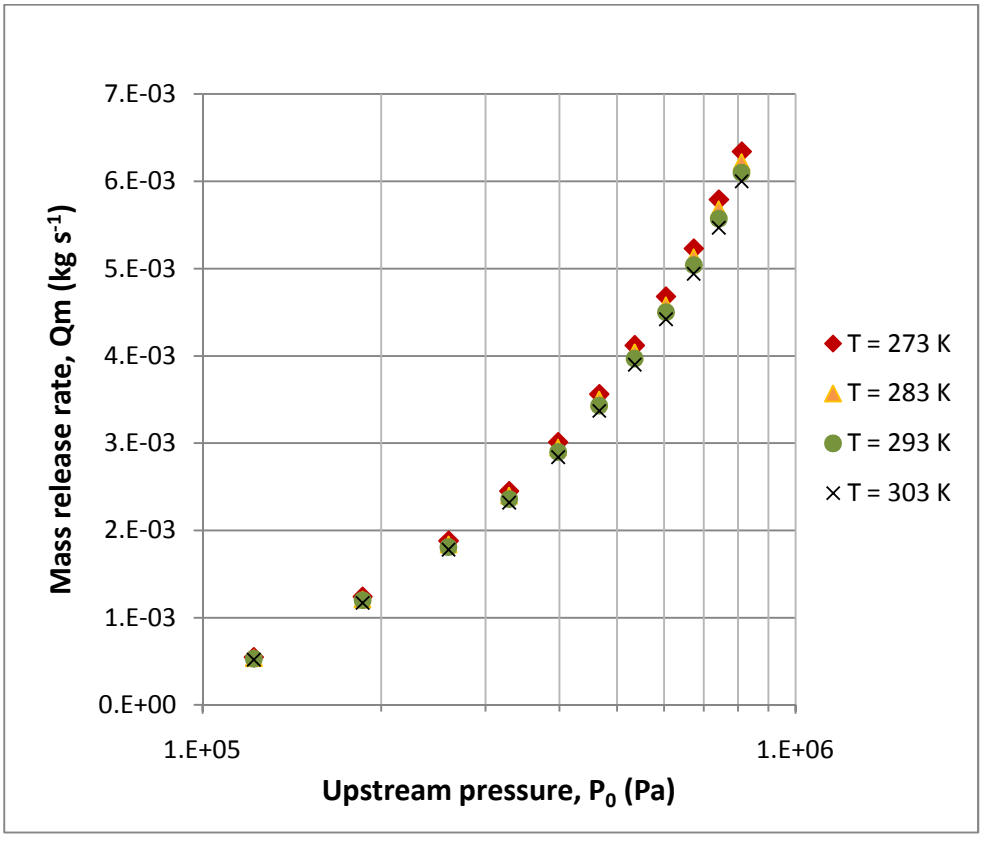

Figure 49. Mass Discharge Rate of Methane Gas from a Leak in a Pipeline at Various Pressures and Temperatures from 2.5 mm Leak Source

Parameters at the gas exit point can indicate the transition of the gas from a critical (choked) to non-critical condition. The exit pressures at various upstream pressures are shown in Figure 50. From that figure, it can be seen that at upstream pressures higher than 2 bar absolute (2 kPa), the gas becomes choked and therefore, the exit pressure increases as upstream pressure increases. The exiting gas will experience a highly non-isentropic series of shocks until it reached the ambient pressure.

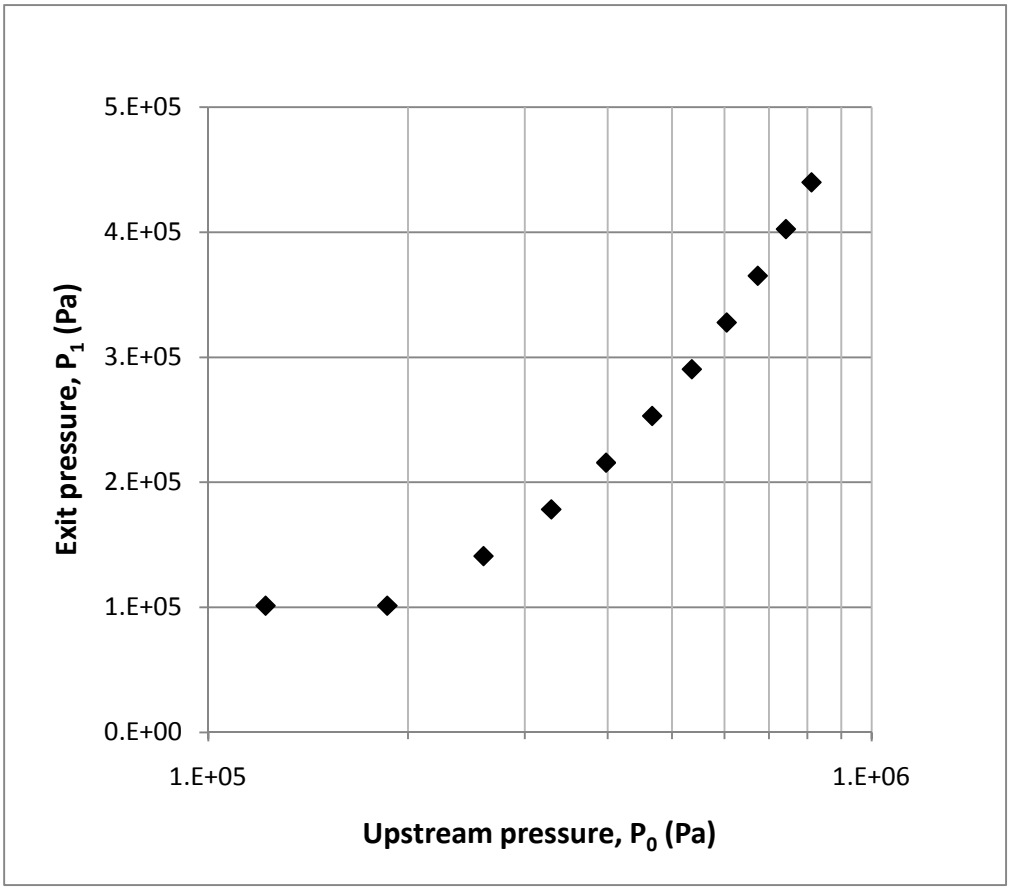

Figure 50. Pressures of Methane Gas at the Release Point as a Function of Upstream Pressures Inside the Pipeline

As the gas reaches critical, sonic, or choked condition, the exit temperature becomes constant although the pressure in the upstream is increased. Figure 51 shows the gas temperature profile at the exit (release) point for different initial temperatures. The exit temperature decreases as the upstream pressure increases until it reaches the sonic condition, and it becomes constant afterward, as shown in Figure 51.

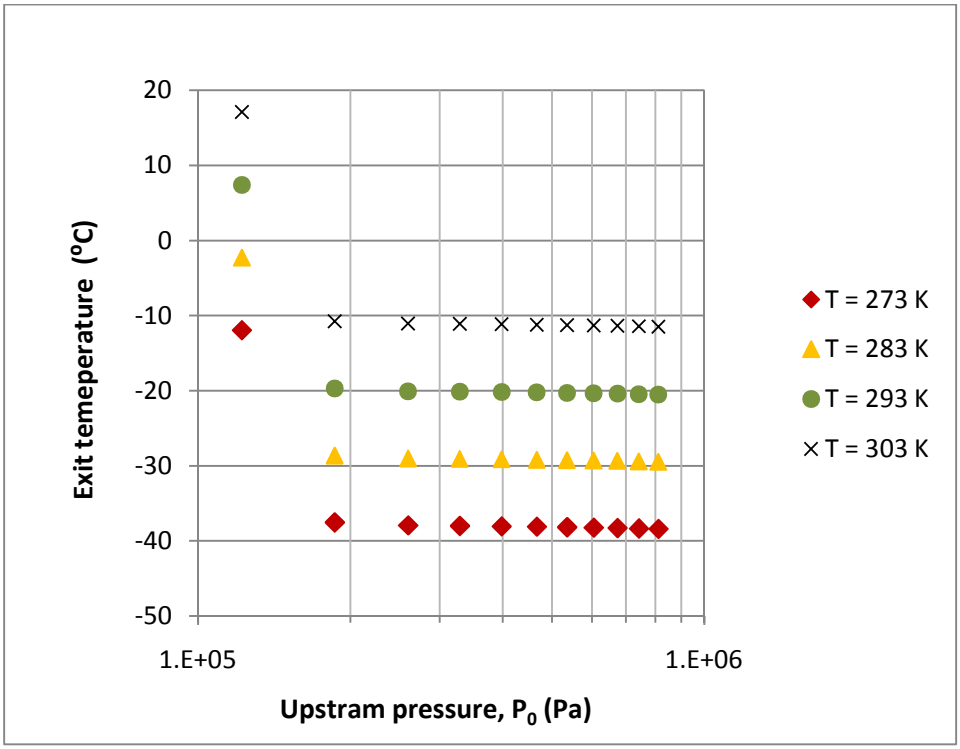

Figure 51. Exit Temperatures of Methane Gas as a Function of Upstream Pressures at Various Initial Gas Temperatures

The exit parameters, i.e. pressure and temperature, are important to determine the phase of methane gas being released in order to determine whether condensation had

occurred due to the expansion of gas from a pressurized source into atmospheric conditions. The boiling point of methane gas is at temperature 0 ºC and 810 kPa is -133 ºC. Therefore, for methane gas released at an upstream temperature range between 0 - 30 ºC and a pressure range of 120 – 810 kPa, the exit pressures and temperatures indicate that the phase of the methane being released is still at 100 % gas.

The density of gas as a function of the pressure and temperature is given in Figure 52. The gas becomes denser as the pressure increases due to compression. However, upon increasing the temperature, the density decreases because the molecules are more spread out at higher temperatures.

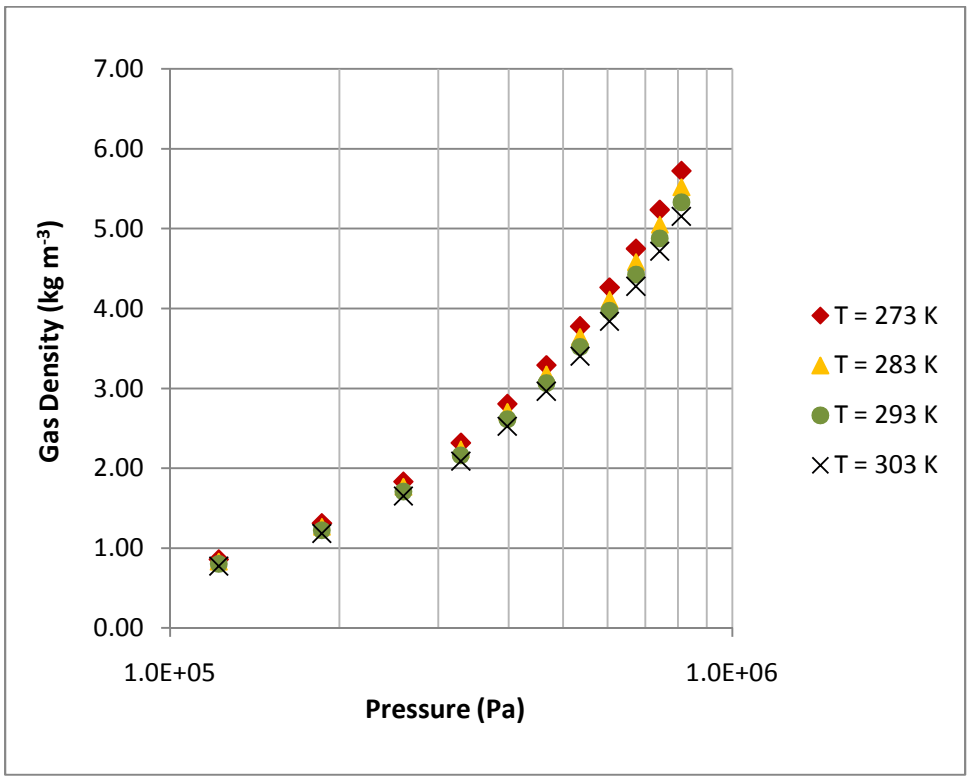

Figure 52. Methane Gas Density as Function of Pressures

The volumetric flow rate of the gas exiting from 2.5 mm hole at various pressures and temperatures is given in Figure 53. The volumetric flow rate of the gas increases significantly at subsonic conditions and stabilizes as the velocity of the gas exiting reaches the sound velocity. For a hole with the same diameter, increasing pressure and temperature does not change the volumetric flow rate dramatically.

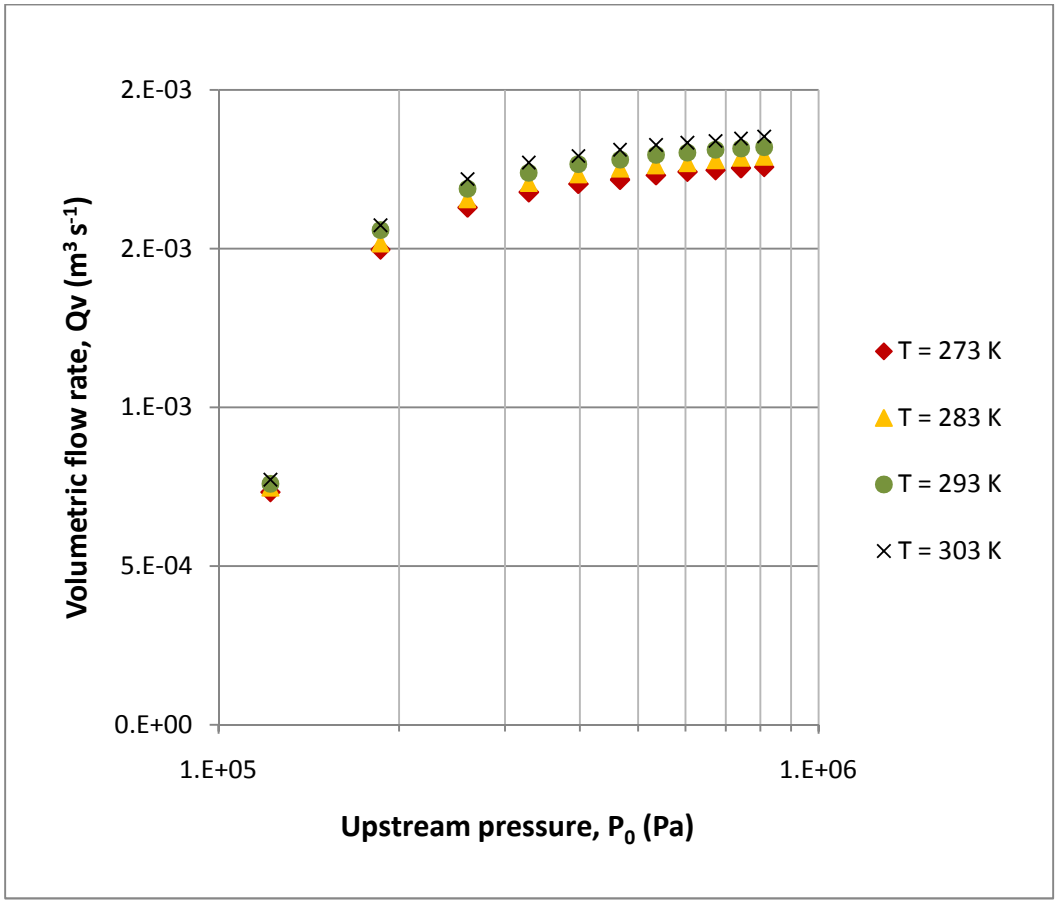

Figure 53. Volumetric Flow Rate of Methane Gas Released from 2.5 mm Diameter Hole for Various Upstream Pressures and Temperatures

The gas mass release rate at various leak sizes with constant gas flow and ambient temperature is shown in Figure 54. The mass flow rate was calculated for a leak diameter range of 2.5 – 25 mm based on the typical size of fugitive leaks in pipelines coming from flanges, connections, fittings and valves. The mass release rate increases rapidly for larger leak areas. In real situations, releases from a large leak will result in a decrease in upstream pressure. However, in this calculation a large inventory of gas inside the chamber is assumed. Therefore, the stagnant upstream condition is applied and a decrease in upstream pressure is not taken into account.

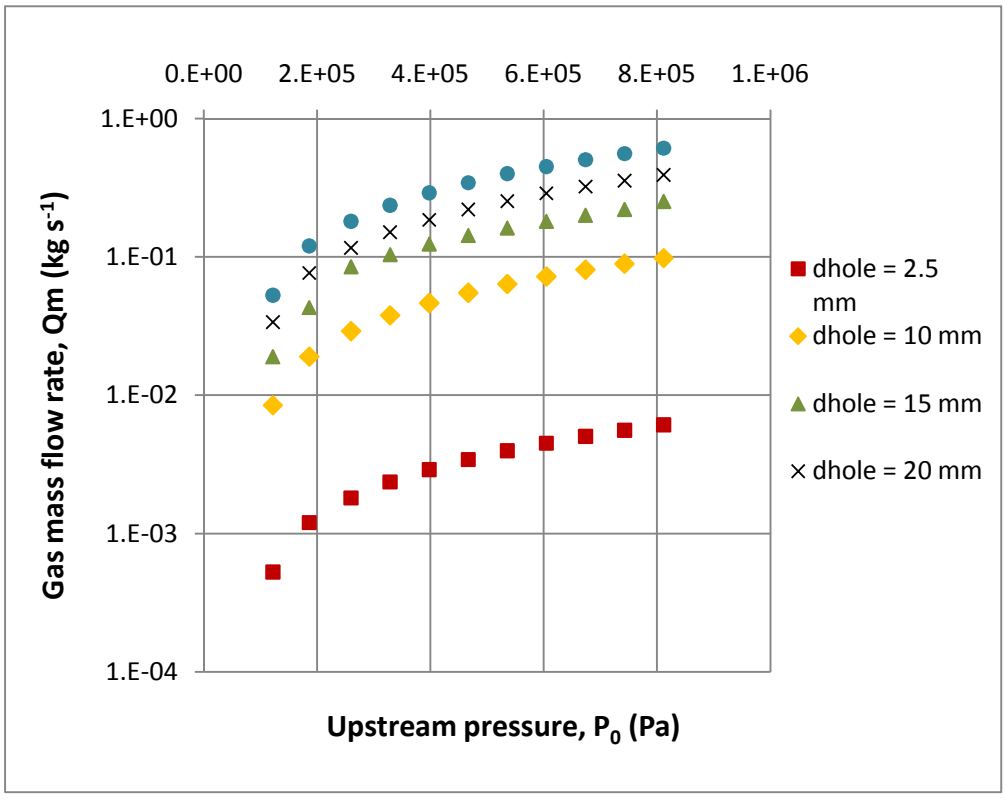

Figure 54. Gas Mass Discharge Rate at 298 K for Various Upstream Pressures and Leak Sizes

The volumetric flow rate at various pressures and leak sizes at temperature of 20 °C is given in Figure 55. As the gas flow becomes choked, the volumetric flow rate becomes constant with regard to pressure for a similar leak size and constant temperature.

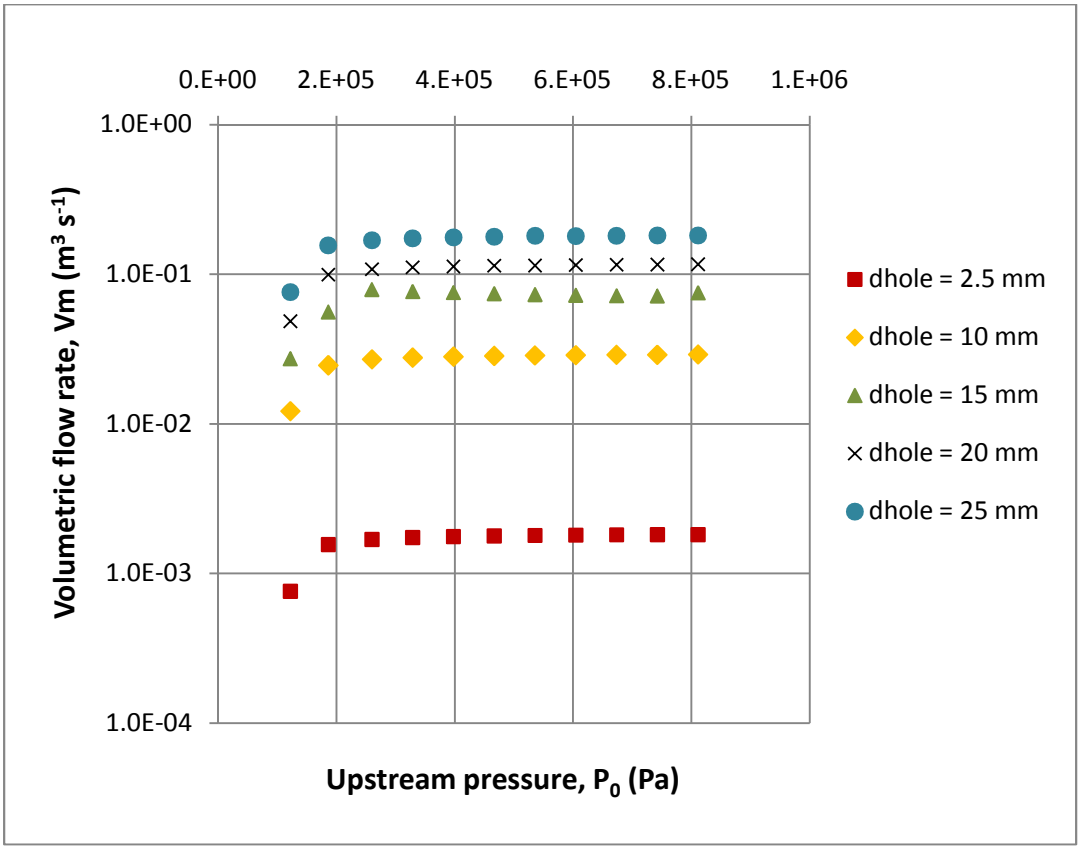

Figure 55. Volumetric Flow Rate of Methane Gas at 298 K for Various Pressures and Leak Sizes

5.2 Prediction of Methane Gas Emissions Rates from the Methane Gas Downwind Distance to Minimum IR-Detectable Concentration

After the source or discharge term is identified, the dispersion of gas is simulated using the generalized Gaussian model calculate the concentration profile along the downwind and vertical direction. The Pasquill-Gifford stability classification is empirically determined based on the amount of incoming solar radiation, the wind velocity, and the terrain surface condition. In the dispersion calculation, the mass discharge rate is assumed to be constant and the gas in the pipelines is at a stagnant condition, so the reduction in the gas inventory upstream is assumed to be negligible. Using this assumption, the concentration downwind and crosswind is merely a function of meteorological conditions. In this paper, the dispersion of methane gas is carried out for three different weather conditions: (i) stable weather conditions (Stability Class F) with 2 ms^{-1} wind speed, (ii) neutral weather conditions (Stability Class D) with a low wind speed (2 ms^{-1}), and (iii) neutral weather conditions (Stability Class D) with medium wind speed (5 ms^{-1}).

The sensitivity of infrared imaging to detect methane gas concentrations in real weather conditions is up to 600 ppm, as described in Table 2. Therefore, the gas emissions rate is calculated based on the size of the cloud up to this minimum detectable concentration.

Figure 56 shows the downwind distance to the minimum detectable concentration as a function of the gas mass release rate at various weather conditions. From that figure it can be implied that the downwind distance is highly affected by the wind speed; however, the change due to different weather stability is not very significant for Class F and Class D. Based on the prediction using the Gaussian model, the downwind distance to 600 ppm of methane gas is increased approximately by a factor of two when the wind speed escalates from 2 ms^{-1} to 5 ms^{-1}.

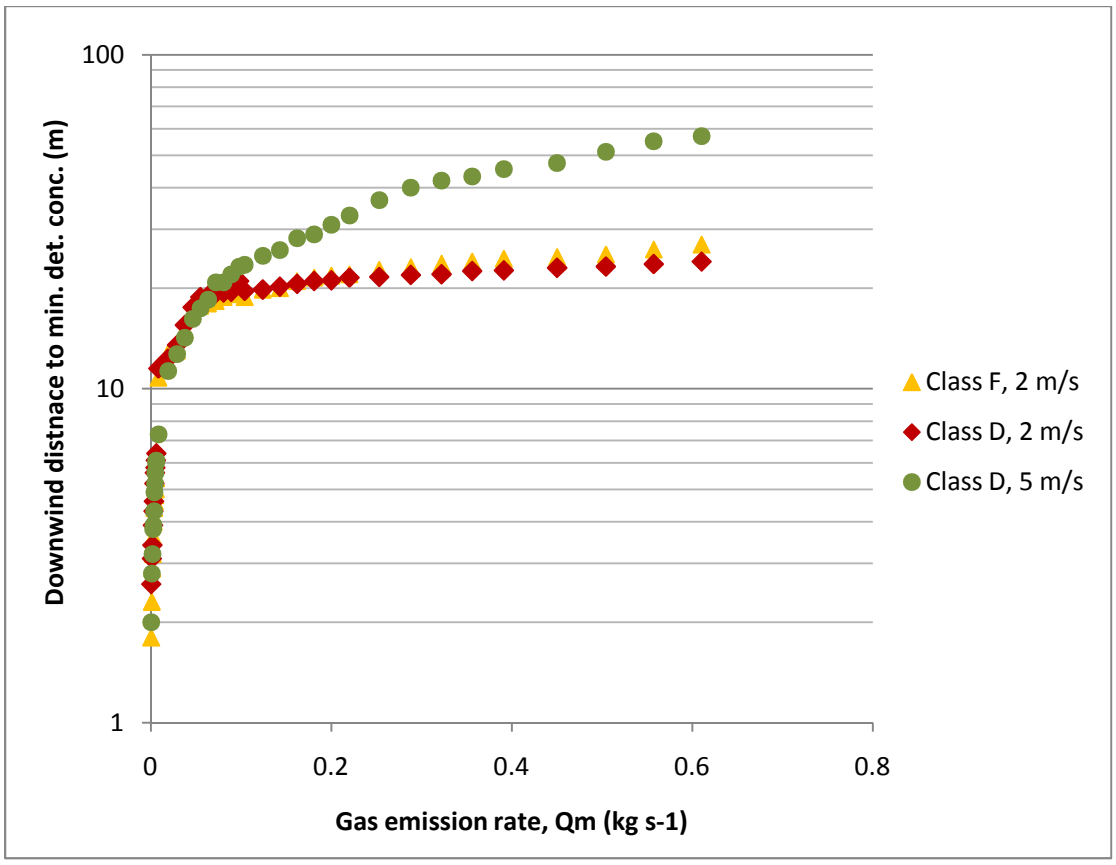

Figure 56. Downwind Distance to Minimum Detectable Concentration as a Function of Gas Release Rate for Different Stability Classes

The effects of the wind speed are also apparent in the height of the cloud. At 600 ppm concentration, the height of the cloud at lower wind speeds is higher than the height of the cloud at higher wind speeds, as shown in Figure 57. This could occur because at higher wind speeds the horizontal momentum from the wind is much larger than the vertical momentum and is a buoyant force on the gas. However, for the same wind velocity, the distance to minimum detectable concentrations is similar for stable and neutral conditions, so the incoming solar radiation or cloudiness has an insignificant effect on the travel distance of dispersed gas.

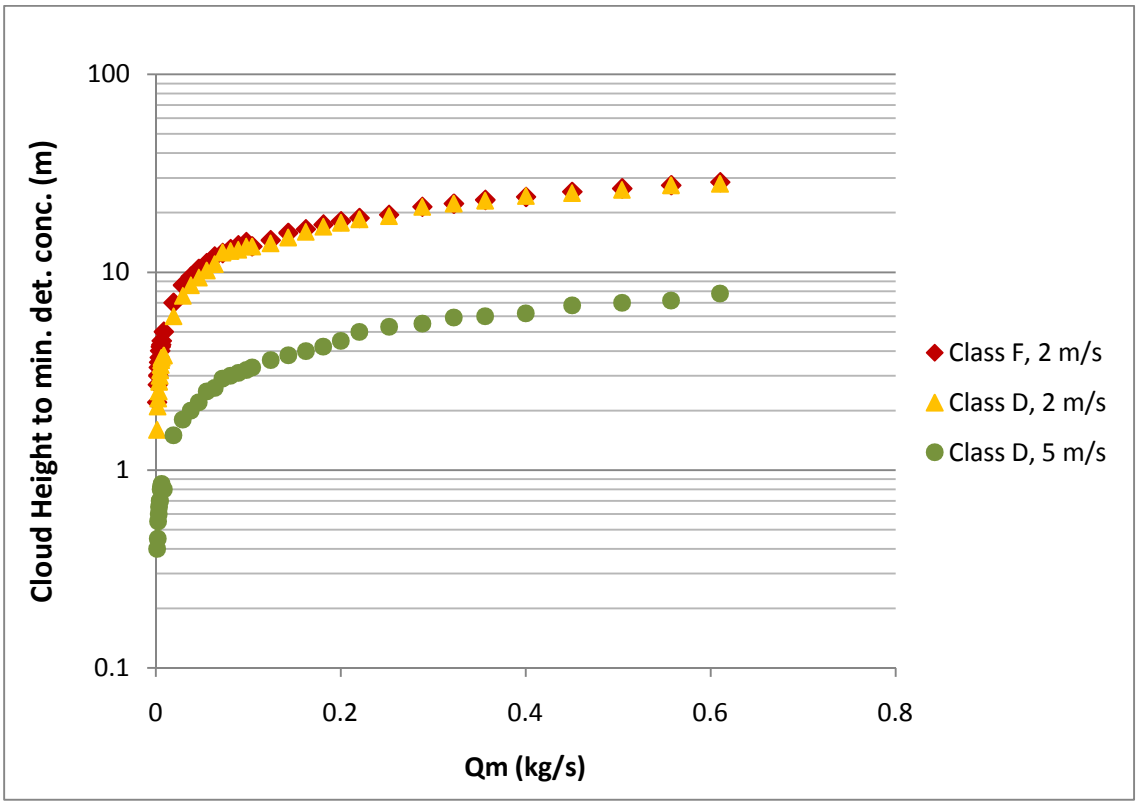

Figure 57. The Height of the Cloud to Minimum Detectable Concentration as a Function of Gas Release Rate for Different Stability Classes

The graphs shown in Figure 56 and Figure 57 demonstrate that the prediction of the gas emission rate based on the cloud size using the Gaussian model works very well for relatively small cloud sizes (less than 30 m in downwind direction and 20 m in height). For larger cloud sizes, the prediction of the emission rate might be inaccurate. Therefore, predicting the discharge rate of gas from a leaky pipeline using optical imaging is suitable for fugitive leaks but not for large leaks or ruptures.

5.3 Summary of Section 5

In this section, the utilization of the infrared imaging technique for gas leak detection is described. A methodology for gas emission quantification is also developed. The gas discharge rate from a leak in a pipeline is a function of the upstream pressure and the size of the leak. However, most of the time the size of the leak is unknown and therefore it was difficult to quantify the emission rate. The infrared imaging technique is able to detect a gas leak and is able to visualize the gas plume. Several previous works have identified the minimum detectable gas concentration which the infrared imager could recognize. Based on this information, a method to estimate the gas emission rate is developed and described in the section. Using a dispersion modeling approach, the correlation between the gas emission rate, the size of the gas cloud and the minimum detectable concentration can be withdrawn. Meteorological conditions such as wind speed and meteorological stability class play an important role in determining how the

gas travels. These parameters affect the downwind distance and the height of the plume to the minimum detectable concentration.

6. CONCLUSIONS AND RECOMMENDATIONS

6.1 Conclusions

Infrared imaging techniques have been considered as smart gas detection methods because they have leading characteristics compared to the point detection method using a total vapor analyzer or gas sniffer. Utilization of the optical imaging method to detect gas leaks in pipelines and components potentially increases process efficiency and an emission control as well as reduces the risk of fire and explosion due to the release of flammable materials.

The limitation of the current technology in infrared imaging techniques for gas detection and visualization relies on the incapability to measure the gas concentration and gas emissions rates. This dissertation aimed to provide a methodology to obtain a more quantitative measure from the thermal image. Two applications of infrared imaging techniques were exhibited, e.g., i) the application of the infrared camera to visualize LNG vapor dispersion from LNG spills on water and ii) the application of infrared imaging for detection of gas leaks in natural gas pipeline systems.

The LNG spilled onto the water at a cryogenic temperature and immediately evaporated into the atmosphere due to the heat transfer process between the LNG and water. In the atmosphere, adiabatic mixing occurred between the LNG vapor and entrained air and caused an increase in the LNG vapor temperature. The thermograms showed the temperature distribution of the dispersed gas, however there was a

discrepancy between the temperatures shown in the thermogram and the thermocouple measurements.

This dissertation presents the evaluation of the thermogram of LNG vapor cloud and determination of the key parameters which affect the temperature measurement of the target gas. The parametric study on the thermal images reveals that the emissivity of the target gas is a major factor in determining the amount of radiation that is transmitted to the camera detector. The emissivity of pure methane gas as a function of temperature and optical length is analyzed. The results show that the assumption that the emissivity value is equal to unity in the camera's algorithm will result in poor accuracy of temperature measurement because the calculation of emissivity of the methane gas at temperature range of 111 – 350 K demonstrates a value range of 0.0002 – 0.25, which are significantly lower than one.

The effect of the atmospheric content and atmospheric conditions were also evaluated. It is evident from the study that water vapor and carbon dioxide, when present in the atmosphere, may reduce the atmospheric transmission. Hence, using the weighted sum of the grey gas model (WSGGM) method, the emissivity of the mixture of methane and atmospheric gases were analyzed at various temperatures and relative humidity. The emissivity function of the gas mixture is integrated into Stefan-Boltzmann law of radiation in order to obtain the actual temperature distribution of the LNG vapor. The result shows that the predictions of temperature using this method are in good agreement with the thermocouple measurements. The actual temperature profile of the gas cloud then can be obtained, and by comparing to the concentration of the LNG vapor at the

time of measurement, a temperature-concentration correlation for the LNG vapor can be calculated. Using this correlation, the concentration of the LNG cloud at certain temperature can be predicted at given atmospheric conditions.

The second part of this dissertation is dedicated to the prediction of emissions rates of gas releases from leaks in natural gas pipeline systems by utilizing the infrared imaging techniques. The minimum detectable methane concentration which can be observed by an infrared camera has been established in previously published literature. The vapor dispersion approach is used to establish a correlation between the gas emissions rate and the distance and height of the plume up to the minimum detectable concentration at different meteorological conditions. Using this correlation, the gas emissions rate from a leak can be quantified by observing the size of the plume shown in the thermograms. Finally, this dissertation presents an analytical tool to estimate the methane gas temperature, concentration and gas emission rates from a rather qualitative thermal image of a gas cloud or plume.

6.2 Recommendations for Future Works

The application of infrared imaging techniques is relatively new in the area of gas detection, visualization and measurement. The quantification method for temperature, concentration and gas emission rates estimation demonstrated in this dissertation is novel and there are vast opportunities in the future for improving and implementing this methodology.

This research performed analyses on the parameters involved in the determination of radiative power transmitted by a gas to a camera detector; however, several parameters which would also be important were not studied in the research works, for instance the optical length and its impact on the atmospheric transmission can be evaluated. Some literature suggested that a longer optical length can considerably reduce the atmospheric transmission. Future research may be conducted on the sensitivity analysis of the optical length and study its impact on atmospheric transmission.

Other potential research work can be done in the application of infrared imaging techniques for fugitive gas emissions from leaks in components or pipelines and for conduct sensitivity analysis of the minimum release rate and minimum concentration that detectable by the optical imaging. The tests can be done under different weather conditions such as ambient temperature, humidity, wind speed and solar radiation intensity, and the impact of these parameters on the minimum release rate and minimum detectable concentration can be observed. Other parameters which influence the camera's performance can be performed, for instance the effects of aerosols in the atmosphere on the thermal image quality or the impact of stimulated emissions and reflections from surrounding objects.

The application of infrared optical imaging for other hydrocarbons such as propane, butane, LPG and other petroleum products is also suggested. Data on the minimum emissions rate and minimum detectable concentrations for different gases can be collected.

There is also a need to optimize the infrared camera placement to maximize the visibility of the gas object in the real facilities. A cost benefit analysis can be performed to determine the number of infrared imaging devices that need to be placed in a facility to obtain maximum monitor of the facility.

Infrared optical imaging has been proposed as the new generation of detection method under the EPA LDAR programs. As a result, the correlation equations and emissions factors that have been established for the previous technique described in EPA Method 21 may not be applicable to the new techniques. Thus, research in this area can also be conducted towards the development of new correlation coefficients and emission factors used to estimate the total emissions from oil and gas systems.

REFERENCES

Barron, R. F. (1999) *Cryogenic heat transfer.* Ann Arbor, MI: Taylor and Francis.

Beer, J.M., Foster, P.J. & Siddall, R.G. *(1971)* Calculation methods of radiative heat transfer. *HTFS Design Report No. 22*. AEA Technology, U.K.

Benitez, L.E. & Penner, S.S. (1950). The emission of radiation from nitric oxide: approximate calculations, *J. Appl. Phys.*, *21* (9), 907-908.

Benson, R., Madding, R., Lucier, R., Lyons, J. & Czerepuszko, P. (2006a). Standoff passive optical leak detection of volatile organic compounds using cooled Insb based infrared imager. *Proceedings of Air and Waste Management Association 99th Annual Conference and Exhibition, 06-A-131*, 1-10.

Benson, R., Panek, J.A. & Drayton, P. (2006b). Direct measurement of minimum detectable vapor concentrations using infrared optical imaging systems. *Proceedings of Air and Waste Management Association 99th Annual Conference and Exhibition, 1052*, 1-14.

Beychok, M. R. (1994). *Fundamentals of stack gas dispersion*. (3rd ed.). Irvine, CA: M.R. Beychok.

Briscoe, F. & Shaw, P. (1980). Spread and evaporations of liquid. *Progress in Energy and Combustion Science, 6*(2), 127-140.

Britter, R.E. & Griffiths, R.F. (1982). *Dense gas dispersion*, Amsterdam: Elsevier Scientific Pub. Co.

Brosmer, M.A. & Tien, C.L. (1984). Infrared radiation properties of methane at elevated temperature. *Journal of Quantitative Spectroscopy Radiation Transfer, 33*(5), 521-532.

Caniou, J. (1999). *Passive infrared detection theory and application*, Boston, MA: Kluwer Academic Publishers.

Cormier, B. R., Qi, R., Yun, G., Zhang, Y. & Mannan, M. S. (2009). Application of computational fluid dynamics for LNG vapor dispersion modeling: a study of key parameters. *Journal of Loss Prevention in the Process Industries, 22*, 332-352.

Crowl, D. A. & Louvar, J. F. (2002*). Chemical process safety: fundamentals with applications*. (2nd ed.) Engleswood Cliffs, NJ: Prentice Hall.

Energy Information Administration (EIA). Section 1: energy consumption by sector. (2009a). *Annual Energy Review*. DOE/EIA-0384. Retrieved from: http://www.eia.doe.gov/aer/consump.html

Energy Information Administration. (2009b). Section Natural Gas: Monthly data on number of producing wells in the United States. Retrieved from: http://eia.doe.gov/dnav/ng/ng_prod_wells_s1_a.htm

Environmental Protection Agency. (1995a). Method 21: Determination of volatile compound leaks. 40 CFR 60. Retrieved from: http://www.epa.gov/ttn/emc/promgate/m-21.pdf

Environmental Protection Agency. (1995b). Office of Air Quality Planning and Standards: Protocol for equipment leak emission estimate. Report #EPA-453/R-95-017. Retrieved from: http://www.epa.gov/ttnchie1/efdocs/equiplks.pdf

Environmental Protection Agency. (2008a). Section 3.5: Natural Gas System (IPCC Source Category 1B2b). Inventory of U.S greenhouse gas emissions and sinks: 1990 – 2007. Report #430-R-08-005. Retrieved from: http://www.epa.gov/climatechange/ emissions/downloads09/InventoryUSGhG1990-2007.pdf

Environmental Protection Agency. (2008b). Verification of portable optical and thermal imaging devices for leak detection at petroleum refineries and chemical plant. *Environmental Technology Verification (ETV) - Environmental and Sustainable Technology Evaluation (ESTE) Project.* Retrieved from: http://www.epa.gov/etv/pubs/ 600s08028.pdf

Epperson, D., Lev-On, M., Tabback, H., Siegell, J. & Ritter, K. (2007). Equivalent leak definitions for smart LDAR (Leak Detection and Repair) when using optical imaging technology. *Journal of Air and Waste Management Association, 57*(9), 1050-1060.

Ermak, L., Chan, S.T., Morgan, D.L. & Morris, L.K. A comparison of dense gas dispersion model simulations with Burro series LNG spill test results. *J. Hazardous Materials, 6*, 129-160

Furry, D., Richards, A., Lucier, R. & Madding R. (2005). Detection of Volatile Organic Compound (VOC) with a spectrally filtered cooled mid-wave infrared camera, *Inframation Proceedings, 6*, 213-218.

Gas Research Institute (GRI)/ U.S. Environmental Protection Agency (EPA). (1996). Methane emissions from natural gas industry. Vol. 2: Technical Report. GRI-94 / 0257.1 EPA–600/R-96-080B. Retrieved from: http://www.epa.gov/gasstar/documents/emissions report/2_technicalreport.pdf

Gifford, F. (1976). Turbulent diffusion typing schemes: a review. *Nuclear Safety, 17*(1), 68-86

Goody, R.M. (1952). A Statistical model for water vapor absorption, *Q. J. R. Meteorol. Soc.*, *78* (336), 165-169.

Gross, W., Hierl, T., Scheuerpflug, H., Schirl, U., Schreer, O. & Schulz, M. (1998). Localization of methane distribution by spectrally tuned infrared imaging. *Proceedings of SPIE Conference on Air Monitoring and Detection of Chemical and Biological Agents, 3533*, 234 – 240.

Hanna, S.R. & Drivas, P.J. (1987). *Guidelines for use of vapor cloud dispersion models.* New York, NY: Center for Chemical Process Safety for the American Institute of Chemical Engineering.

Holst G.C. (1998). *Testing and evaluation of infrared imaging systems.* (2nd ed.). Winter Park, FL: SPIE Press.

Holst, G. C. (2000). *Common sense approach to thermal imaging.* Winter Park, FL: SPIE Press.

Hottel, H.C. & Sarofim, S.F. (1970). Models of radiative transfer in furnaces, *Journal of Engineering Physics and Thermophysics, 19*(3), 1102-1114.

Howard, J.N., Burch, D.E. & Williams, D. (1956). Infrared transmission of synthetic atmosphere. II. absorption by carbon dioxide. *J. Opt. Soc. Am., 46* (4), 237-241.

Howard, J.N., Burch, D.E. & Williams, D. (1963). Infrared transmission of synthetic atmosphere. III. absorption by water vapor. *J. Opt. Soc. Am., 6* (2), 585-589.

Jacob, P.A. (2006). *Thermal infrared characterization of ground targets and background*. (2nd ed.). Bellingham, WA: SPIE Press.

Kirchgessner, D.A., Lott, R.A., Cowgill, R.M., Harrison, M.R. & Shires, T.M. (1997). Estimate of methane emissions from U.S. natural gas industry. *Chemosphere, 35*(6), 1365 – 1390.

Leake, D., Moore, M., Murthi, A. & Mannan, S.M. (2005). Application of visualization and thermal detection technique for non-intrusive imaging of LNG leaks and plumes, *Proceedings of 8th Annual Mary Kay O'Connor Process Safety Symposium,* 164-181.

Leckner, B. (1972). Spectral and total emissivity of water vapor and carbon dioxide, *Combustion and Flame, 19*, 33-48.

Lee, R.H.C & Happel, J. (1964). Thermal radiation of methane gas. *Ind. Eng. Chem. Fundamen., 3*(2), 167-176

.

Lev-On, M., Epperson, D., Siegell, J. & Ritter, K. (2007). Derivation of new emission factors for quantification of mass emissions when using optical gas imaging for detecting leaks. *Journal of Air and Waste Management Association. 57*, 1061 – 1070.

Liou, K.N. (2002). *An introduction to atmospheric radiation*. (2nd ed.). San Diego, CA: Academic Press.

Macdonald, R. (2003). Theory and objectives of air dispersion modeling. *Internal Report MME 474A*. University of Waterloo, Waterloo, Ontario, Canada.

Madding, R. (2006). New development in portable infrared camera technology. *Hydrocarbon Processing, 85*(11), 83-86.

Malkmus, W. (1963). Infrared emissivity of carbon dioxide (4.3-μ band). *Journal of The Optical Society of America, 53*(8), 1963.

Minkina, W. & Dudzik, S. (2009). *Infrared thermography: errors and uncertainties*. John Wiley & Sons, Ltd. West Sussex, U.K.

Modest, M.F. (2003). *Radiative heat transfer*. (2nd ed.). San Diego, CA: Academic Press.

Nielsen, M. (2002). Spreading of cold dense gas cloud. In *The Handbook of Hazardous Material Spills Technology*. New York: McGraw-Hill; Fingas, M.E, *Chapter 18*, 1-15

Ostrander, M.H. (1951). Emissivity calculations for carbon monoxide. California Institute of Technology, Pasadena, CA.

Park, W. & Kim, T. (2003). Application of the weighted sum of gray gases model for nonhomogeneous gas mixtures having arbitrary compositions. *Proceedings of Eurotherm 73 on Computational Thermal Radiation in Participating Media*, 129-137.

Penner, S.S. & Gray, L.D. (1961). Approximate infrared emissivity calculations for HCl at elevated temperature, *J. Opt. Soc. Am., 51*(4), 460-462

Penner, S.S., Ostrander, M.H. & Tsien, H.S. (1952). The emission of radiation from diatomic gases III. numerical emissivity calculations for carbon monoxide for low optical densities at 300 K and atmospheric pressure. *J. Appl. Phys., 23*(2), 256 -263

Perry, R.H. & Green, D.W. (2008). *Perry's chemical engineering handbook*. (8th ed.). New York, NY: McGraw-Hill.

Pierluissi, J.H. & Maragoudakis, C.E. (1986). Band model for molecular transmittance of carbon monoxide. *Appl. Opt., 25*(22), 3974-3977.

Plisson-Saune, S., Suripno, S., Cramer, A., Pramono, H., Camps, R. & Lacamoire. H. (2008). Fugitive emissions management through infrared monitoring – full scale field application. *Proceedings of the Annual International SPE Conference on Health, Safety and Environment in Oil and Gas Exploration and Production, 111584*, 1- 10.

Robinson, D.R, Luke-Boone, R.E., Aggarwal, V., Harris, B., Anderson, E., Ranum, D., Kulp, T.J., Armstrong, K., Sommers, R., McRae, T.G., Ritter, K., Siegell, J.H., Van Pelt, D. & Smylie, M. (2007). Refinery evaluation of optical imaging to locate fugitive emissions. *Journal of Air Waste Management Association,* 57(7), 803-810.

Sandberg, C., Holmes, J., McCoy, K. & Koppitsch, H. (1989). The application of a continuous leak detection system to pipelines and associated equipment. *IEEE Transaction of Industry Applications*, *25*(5), 241-244.

Schulz, M., Gross, W. & Scheuerpflug, H. (2008). High resolution thermophysical measurements using staring infrared detector arrays. *High Temperatures – High Pressures, 32*, 527 – 536.

Siegel, R. & Howell, J. (2002). *Thermal radiation heat transfer*. (4th ed.). New York, NY: Taylor & Francis.

Sklavounos, S. & Rigas, F. (2005). Fuel gas dispersion under cryogenic release condition. *Energy& Fuel, 19*(6), 2535-2455.

Smith, B.C. (1999). *Infrared spectral interpretation: a systematic apporach*. Boca Raton, FL: CPRC Press.

Smith, J.M., Van Ness, H.C. & Abbot, M.M. (1996). *Introduction to chemical engineering thermodynamics.* (5th ed.) New York: McGraw-Hill.

Smith, T.F., Shen, Z.F. & Friedman, J.N. (1982). Evaluation of coefficients for the weighted sum for gray gases model, *J. Heat Transfer, 104*(4), 602-608.

Staley, D.O. & Jurica, G.M. (1970). Flux emissivity table for water vapor, carbon dioxide and ozone. *Journal of Applied Meteorology, 9*(3), 365-372.

Yegnan, A., Williamson, D.G. & Graettinger, A.J. (2002). Uncertainty analysis in air dispersion modeling, *Environmental Modeling & Software, 17*(7), 639-649.

VITA

Anisa Safitri was born in Bandung, Indonesia. She graduated with a B.Sc. in chemical engineering from Institut Teknologi Bandung, Indonesia in 2002. After graduating, she continued to pursue her Master's degree at Technische Universiteit Eindhoven, the Netherlands. She graduated with her M.Sc. in chemical engineering in 2005.

In August 2006, she joined the Chemical Engineering Department at Texas A&M University as a doctoral student. Since then, she has worked in the area of "preventive maintenance for natural gas systems using infrared imaging techniques" under the guidance of Dr. Sam Mannan. She received her Ph.D. in May 2011.

Her permanent address is:

Artie McFerrin Department of Chemical Engineering

Texas A&M University

Jack E. Brown Engineering Building

3122 TAMU Room 200

College Station, TX, 77840-3122

c/o M. Sam Mannan